Study of Electromagnetically Coupled Microstrip Arrays

Prepared by:
Mehdi Hamid Zahedi

A Thesis:
Submitted to the Faculty of Graduate Studies
in Partial Fulfillment of Requirements
for the Degree of

MASTER'S OF SCIENCE IN ENGINEERING

DEPARTMENT OF ELECTRICAL AND COMPUTER ENGINEERING
UNIVERSITY OF MANITOBA,
WINNIPEG, MANITOBA

THE UNIVERSITY OF MANITOBA

FACULTY OF GRADUATE STUDIES

*****

COPYRIGHT PERMISSION PAGE

STUDY OF ELECTROMAGNETICALLY COUPLED MICROSTRIP ARRAYS

BY

MEHDI HAMID ZAHEDI

A Thesis/Practicum submitted to the Faculty of Graduate Studies of The University of Manitoba in partial fulfillment of the requirements of the degree of

MASTER OF SCIENCE

Abstract

This thesis focuses on study and design of proximity fed arrays which consist of microstrip patch resonators placed near a feedline and coupling takes place through the gap inbetween. The configuration is capable of supporting standing-wave and traveling-wave excitations. When operating in the resonant mode, either the current or voltage standing-waves can be used as the excitation. Capacitive coupling or fringing electric fields at feedline edge results in creation of potential difference between two patch edges and resonant current on the patch. Capacitive coupling is best suited for vertical polarization (with respect to the feedline current). Horizontal polarization (or co-linear polarization with respect to the feedline current) is induced effectively by current standing-wave (or magnetic fields). Any desired distribution can be established across the array by a proper adjustment of the gap width. A minor modification in gap distribution along the array is also required in order to obtain a better uniform distribution for either standing-wave or traveling-wave excitation since the excitation is of series-fed type. The configuration can provide a dual band arrangement, an arrangement for a band at one side of the feedline or a single band cross-linear array may be arranged. The cross-linear array is suitable mainly for reducing the cross-polarization in a vertically polarized configuration. One effective technique to improve the performance bandwidth is to configure a progressive incremental length added to the resonant length across the array. The single linear array can surely be expanded to planar configuration for enhancement purposes.

Acknowledgement

I greatly appreciate the exceptional freedom and continual support provided by Dr. Shafai who also tolerated my shortcomings and improper communication of information during the extended years of study.

Special thanks to Brad Tabachnik for his co-operation, to R. Chaitanya Babu for his numerous advice, to Fethi Bellamin for his assistance, and to Derek Gray for many enlightening remarks regarding the subject matter.

Also hearty thanks to many colleagues who shed light on many questions during numerous discussions.

A sincere acknowledgement of my wife's constant comfort and confidence during the extent of my study and along many anguishing periods.

M. Hamid Zahedi

September 26, 1997

Contents

List of Figures

List of Tables

Chapter 1

Introduction

1.1 Introduction

Microstrip patch antennas have become popular candidates for many applications due to low cost, low profile and have been the focus of extensive research in the last few decades. Their compatibility with monolithic microwave integrated circuits (MMIC) has also expanded their applications and promoted further studies on various feeding and array configurations. This thesis is the result of investigation on an electromagnetically coupled array configuration which has received only a limited attention in literature.

Throughout this investigation a newly available software, **Ensemble** is used, which is capable of simulating multi-layer dielectric structures containing metallic shapes. **Ensemble** provides accurate results where surface or leaky waves are not excited.

1.2 Brief History

The subject of proximity fed antenna was addressed first by Cashen *et al.* [1] in 1970 and arrays of capacitively coupled resenators were produced by Emi-Varian in 1973 [2] as extracted from [3]. Report of characteristics such as maximum side lobe level of -12 dB for a resonant array and a bandwidth approximately equal to the one tenth of beamwidth is given in few articles. Nevertheless it appears that the subject was not thoroughly dealt with over the years and scarce reports are available on this matter.

One distracting issue is the terminology used for the structure. The proximity fed resonator is commonly addressed as two layer structure where feedline is placed above a ground plane and coupling takes place electromagnetically between the feedline and the radiator on the top layer. In our configuration the radiator is placed near the feedline on the same plane.

Traces of similar studies have been found in the literature but lack of accessibility to such sources restrained us from complete acknowledgement of the type and results of ongoing studies. In one available article [4], the case of single patch in proximity of an open feedline has been considered. The study focuses mainly on how to alter the polarization by adjusting the open stub length (i.e. the extension of feedline beyond the patch up to the termination). When the patch is at current standing-wave maximum, magnetic field creates a current on the radiating patch in the direction of feedline, in other words, an inductive coupling takes place. If voltage standing-wave maximum is used as excitation, charge accumulation at one edge of the patch creates a potential difference across the patch and ultimately a current exists on the patch transverse to the feedline. This is considered a capacitive coupling.

1.3 Topic Outline

The study begins with a concise overview of microstrip transmission line and radiating patch structures, where the required formulation and simplified models are provided. Next various power distributions across the array with emphasis on the Taylor distribution are reviewed. The last section provides a description of the software employed, **Ensemble**, where its features and shortcomings are explained.

Chapter two discusses the required design curves for a single patch case for two categories of standing-wave and traveling-wave feeding methods. Important parameters and their effects are investigated and sufficient explanations are provided.

Chapter three details the array simulations for both feeding methods and studies the effects of various parameters on the array performance. The cross-linear array, a cross-positioned arrangement of elements to reduce the cross-polarization, is also discussed as well as dual band array configurations which provide dual operating

frequency and dual polarization of choice with a single configuration.

Chapter four describes the construction of prototypes, physical dimensions used, problems encountered during the fabrication and testing as well as the test results. It also provides a complete comparison between the experimental results and the corresponding simulation results.

The last chapter summarizes the results achieved from the study and indicates the highlights of the research.

1.4 Microstrip Transmission Line

The basic model of a transmission line is a parallel plate structure having an infinite length but a finite width located some distance apart. Ideally, the parallel-plate structure can support the TEM mode defined as E- and H-fields normal to each other as well as being normal to the direction of propagation. Figure 1.1 indicates the fields and current components in longitudinal cross-section. Classical equations determining model components of the transmission line based on the parallel-plate structure are sufficiently known.

Microstrip transmission lines provide a means for distribution and coupling of power from the source to the radiating elements. Thus, a brief review of the propagation mechanism helps in understanding of its operation. This review emphasizes on printed transmission lines only (Figure 1.2).

1.4.1 Static and Dynamic Analyses of Printed Transmission Line

In practice pure TEM modes do not exist along printed transmission lines. Instead, there is a quasi-TEM, or hybrid modes, whose exact field configurations are quite complicated. In contrast to the parallel-plate waveguides, the electric fields are no longer confined between the two metallic layers but have components transverse to the lines edges. Magnetic fields maintain the flux encircling the line.

At frequencies lower than the static approximation frequency ($0 \leq f \leq f_{g,stat} \approx$

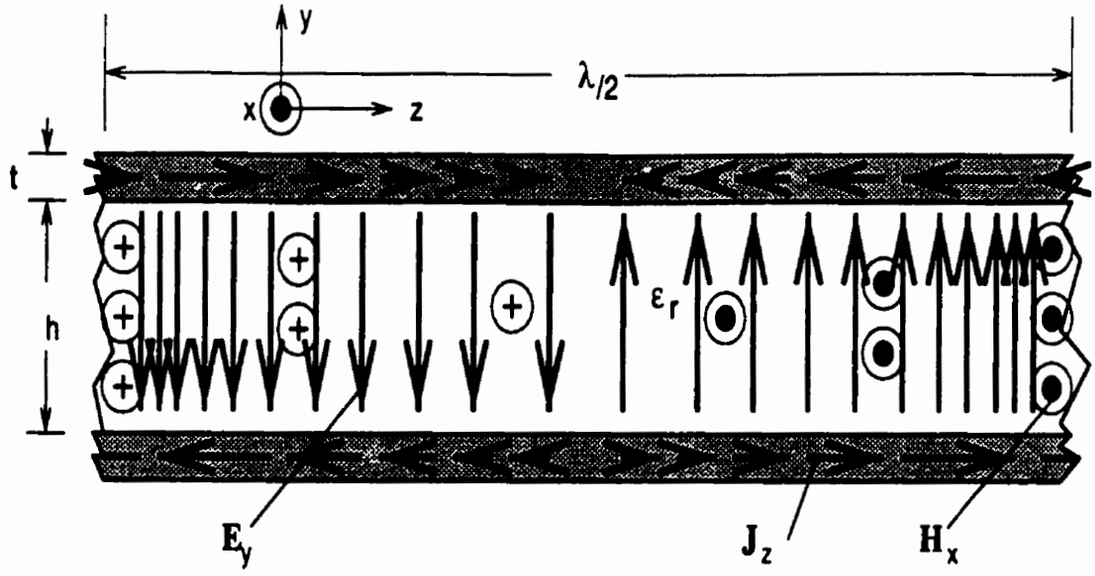

Figure 1.1: Field and Current Patterns in Parallel-plate Waveguide

1-5 GHz) given by ([5] pages 136-137)

$$f_{g,stat} \approx \frac{21.3}{(W+2h)\sqrt{\epsilon_r+1}}$$

(W and h in mm, $f_{g,stat}$ in GHz), the fields are mostly TEM and field components other than TEM are negligibly small. This means that fields can still be considered TEM despite the fringing effect at the edges. When frequency is higher than the cut-off frequency for the above static approximation, $f_{g,stat}$, the longitudinal field components along the direction of propagation become significant and their strength become more pronounced as frequency increases.

1.4.2 Wheeler Formulation

For calculation of the line width or the impedance of a transmission line with given material parameters, the well-known Wheeler's equations for microstrip line may be employed. They are given below for the case of zero conductor thickness ([5], pages 144-147).

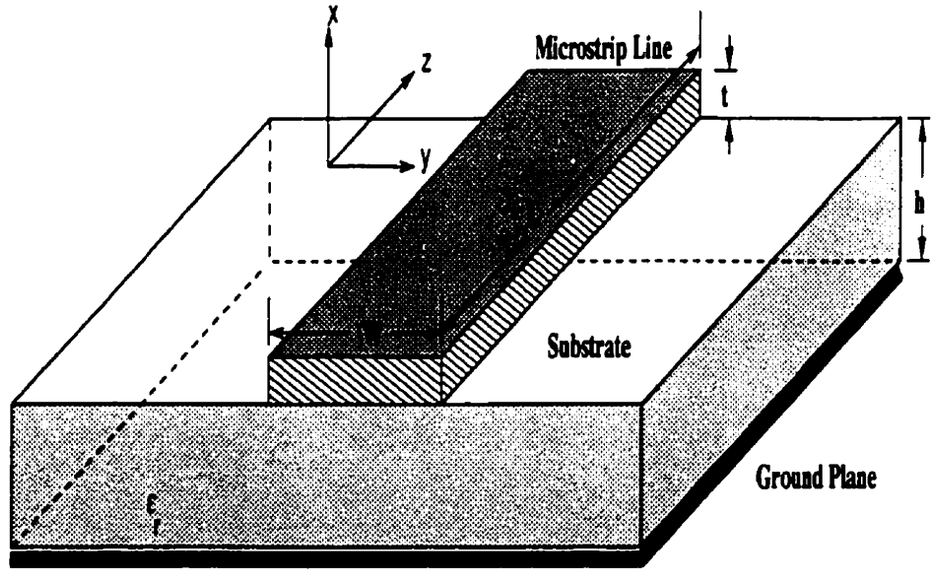

Figure 1.2: Diagram of Printed (Microstrip) Transmission Line

1) Characteristic impedance of narrow microstrip conductor, $W/h \leq 3.3$

$$Z_L = \frac{120}{\sqrt{2\left(\epsilon_r + 1\right)}} \left[\ln\left\{ \frac{4h}{W} + \sqrt{16\left(\frac{h}{W}\right)^2 + 2} \right\} - \frac{\epsilon_r - 1}{2\left(\epsilon_r + 1\right)} \left\{ \ln\left(\frac{\pi}{2}\right) + \frac{\ln\left(\frac{4}{\pi}\right)}{\epsilon_r} \right\} \right] \tag{1.1}$$

2) Characteristic impedance of wide microstrip conductor, $W/h \geq 3.3$

$$Z_L = \frac{60}{\sqrt{\epsilon_r}} \left[\frac{W}{2h} + \frac{\ln 4}{\pi} + \frac{\epsilon_r + 1}{2\pi\epsilon_r} \left\{ \ln\left(\frac{\pi e}{2}\right) + \ln\left(\frac{W}{2h} + 0.94\right) \right\} + \frac{\left(\epsilon_r - 1\right) \ln\left(\frac{e\pi^2}{16}\right)}{2\pi\epsilon_r^2} \right]^{-1} \tag{1.2}$$

The above formulas can also be arranged in terms of the line width. However, this results in a complicated form and requires extensive mathematical manipulation. The width for the desired impedance can be obtained by successive trials. As an example, using the material parameters of $h = 1.524$ mm and $\epsilon_r = 3.2$, a width, $W = 3.6$ mm, for a 50Ω microstrip line is obtained. This width is used throughout the simulations in this study as the feedline width. The effective dielectric constant for this microstrip line using Equation 1.3 (W_p replaced by W) is $\epsilon_{eff} = 2.55$.

1.5 Microstrip Patch

Printed Microstrip patch structures consist of a metallic patch of any shape above another metallic layer known as the ground-plane supported by dielectric materials, or substrates, as shown in Figure 1.3.

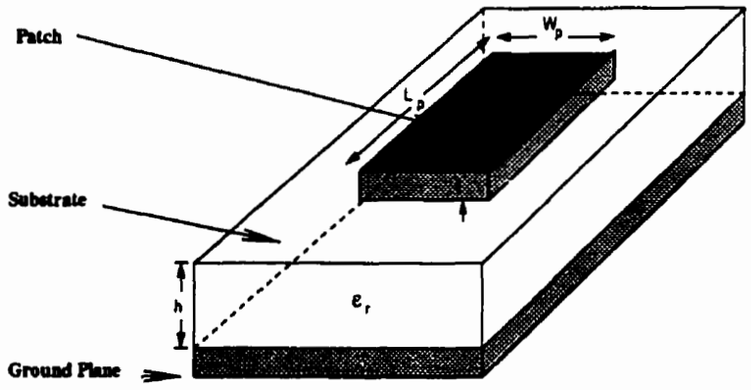

Figure 1.3: Patch Configuration with Common Dimensions

There are many modeling methods for investigating the microstrip patch structures. The Transmission Line Model (TLM) and Cavity Model (CM) are the two simplest and reasonably accurate models. More accurate modelings use numerical computations such as the integral equation formulations along with the Moment Method. The **Ensemble** software is based on such a method. Other modeling techniques are also available and their details can be found in the literature [6].

1.5.1 Design Equations

The necessary equations for the patch design are given as:

1) Effective Dielectric Constant, ϵ_{eff}: This compensates for the differences in material properties at the interface of two media. The effective dielectric constant is given by [7]

$$\epsilon_{eff} = \frac{\epsilon_r + 1}{2} + \frac{\epsilon_r - 1}{2}(1 + \frac{10h}{W_p})^{-\frac{1}{2}} \tag{1.3}$$

where h, W_p, and ϵ_r are respectively the substrate thickness, the patch width and dielectric constant.

2) Effective Length, L_{eff}: Due to the fringing effect which is the extension of the field at the edges of the patch, the electrical length of the patch normally appears larger than its physical length. The optimal patch length is $\frac{\lambda_g}{2}$, ($\lambda_g = \frac{\lambda_o}{\sqrt{\epsilon_{eff}}}$), to create an array of two radiating slots at each edge, $\frac{\lambda_g}{2}$ distance for maximum performance. The difference between the optimal length and the actual length, $L_{eff} = L_p + 2\Delta L = \frac{\lambda_g}{2}$, is determined by following equation [7]

$$\frac{\Delta L}{h} = \frac{[0.412(\epsilon_{eff} + 0.3)][\frac{W_p}{h} + 0.264]}{[\epsilon_{eff} - 0.258][\frac{W_p}{h} + 0.8]} \tag{1.4}$$

where L_p denotes the physical patch length and ΔL is the estimate of incremental length due to the fringing effect.

1.5.2 Radiation Pattern

The radiation of a rectangular patch is mainly attributed to its two radiating edges which are approximately modeled as radiating slots. Each slot is narrow having a width approximately equal to the substrate height, h, ($h \ll \lambda_o$ usually $0.003\lambda_o \leq h \leq 0.05\lambda_o$) and length corresponding to the patch width. An array of two rectangular slots each having dimensions of the patch width and substrate thickness provides a reasonable approximation in a closed-form expression for the far-zone radiation field components. The two slot approximate model gives very simple expressions for the radiation pattern. For a patch located in the xy-plane where length is along x-direction as shown in Figure 1.4, the H-plane radiation pattern is given by

$$E_\theta(\theta)|_{\phi=0} = K_T \frac{\sin\left(\frac{\pi W_p}{\lambda_o}\sin\theta\right)}{\frac{\pi W_p}{\lambda_o}\sin\theta}\cos\theta$$

and the E-plane pattern is expressed as

$$E_\phi(\theta)|_{\phi=\pi/2} = K_T \frac{\sin\left(\frac{\pi h}{\lambda_o}\sin\theta\right)}{\frac{\pi h}{\lambda_o}\sin\theta}\cos\left(\frac{\pi L_p}{\lambda_o}\sin\theta\right)$$

in spherical coordinates [8]. K_T is given as a constant by

$$K_T = -jV_o W_p k_o \left(\frac{e^{-jk_o R}}{4\pi R}\right)$$

with k_o denoting the propagation constant in free space and V_o representing the voltage across the slot.

Figure 1.4 illustrates the familiar microstrip patch patterns and the coordinate system used. The principle planes for the given geometry are E-plane (i.e. the plane transversing the radiating edges, $\phi = 0$) and H-plane (the plane parallel to the radiating edges, $\phi = \pi/2$)

Observation of the patterns and formulations reveal a broad pattern normal to the plane of the patch with possible linear or circular polarization depending on the excitation. Excitation can be direct via a coaxial probe, or microstrip transmission line or indirect (electromagnetically coupling) through proximity or an aperture. Depending on the substrate material and thickness, microstrip patch antenna exhibits various directivity. Typical gain of microstrip patch depending on the substrate material and thickness varies between 3 to 9 dBi.

1.6 Review of Power Distribution Methods

A quick review of the array theory provides some insight into the power distribution across an array. A single element usually has a broad radiation and low gain. Therefore enlarging the size of the antenna helps to increase the directivity and also provides means of controlling the radiation pattern through control parameters. In array design there are five control parameters which could be used to meet the desired specifications.

1) Geometrical configuration of the array: It should meet pattern and gain as well as size specifications along with fabrication scheme and suitability.

2) Interelement spacing: This controls overall pattern, side lobe level and grating lobes.

3) Amplitude distribution across the array: This allows us to obtain the desired pattern and side lobe level.

4) Phase distribution across the array: It determines the beam location and provides beam steering mechanism.

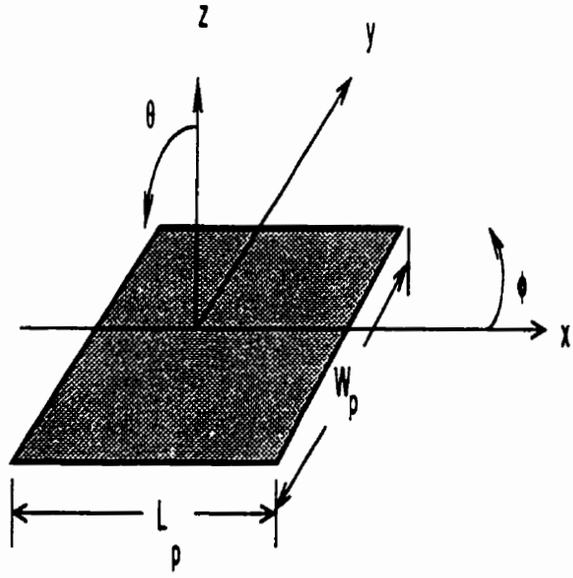

(a) Microstrip Patch Coordinates: $W_p = 37.5\,mm$, $L_p = 41.3\,mm$ @ 2 GHz

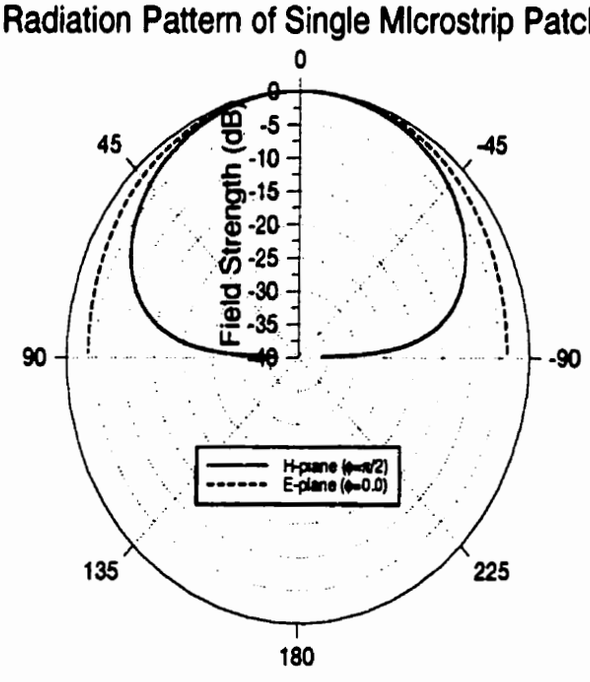

(b) E- and H-plane Patterns

Figure 1.4: Rectangular Patch Geometry and Far-field Patterns with X-polarized Excitation

5) Relative pattern of the individual elements: This is the building block of overall array pattern.

In the array theory the single element pattern and array factor provide the array pattern without consideration of mutual coupling between elements. This principle is known as pattern multiplication, where the single element pattern is directly multiplied to the array factor. Based on this principle, different array factors can be applied to the configuration under study. The general expression for the total E-field across a linear array [9] is

$$E(\theta,\phi) = f(\theta,\phi)\sum_{i=1}^{N} I_i \exp\left[j\left(k_o r_i \cos\psi_i + \alpha_i\right)\right]$$

where $f(\theta,\phi)$ represents the far-field function associated with the particular element, $k_o = 2\pi/\lambda_o$, I_i is the element amplitude of excitation and α_i denotes their phase excitation. The coordinates (r_i, θ_i, ϕ_i) refer to the element location with $i = 1, 2, \ldots, N$; N denoting the number of elements. The cosine term takes the expanded form of

$$\cos\psi_i = \cos\theta\cos\theta_i + \sin\theta\sin\theta_i\cos\left(\phi - \phi_i\right)$$

in terms of the spherical coordinates. In this study, linear type arrays with equal phase difference between adjacent elements are considered.

1.6.1 Common Excitation Amplitude Distributions

Beside the uniform distribution which is the most common type, there are a few other methods of amplitude distributions. The most known ones are the triangular, cosine, cosine-squared, binomial, Taylor and Dolph-Tschebyscheff distributions. Among simple distribution functions such as uniform, triangular, cosine and cosine-squared, the last exhibits some advantages over the other ones. The following table (Table 1.1 taken from [7]) indicates that tapered distributions decrease the gain and broaden the beamwidth but lower the side lobe levels.

The above distribution functions, respectively, establish only a fixed pattern characteristic across the array, while a great degree of flexibility in design exists by using the last three methods. The binomial and Dolph-Tschebyscheff distributions use

Table 1.1: Comparison among Simple Distribution Functions Used in Arrays

Distribution	Uniform	Triangular	Cosine	Cosine-squared
Half-power beamwidth (degrees) $l \gg \lambda$	$\frac{50.6}{(l/\lambda)}$	$\frac{73.4}{(l/\lambda)}$	$\frac{68.8}{(l/\lambda)}$	$\frac{83.2}{(l/\lambda)}$
First-null beamwidth (degrees) $l \gg \lambda$	$\frac{114.6}{(l/\lambda)}$	$\frac{229.2}{(l/\lambda)}$	$\frac{171.9}{(l/\lambda)}$	$\frac{229.2}{(l/\lambda)}$
First side lobe maximum (dB)	-13.2	-26.4	-23.2	-31.5
Directivity factor (for large l) Multiply by $2\left(\frac{l}{\lambda}\right)$	1	0.75	0.810	0.667

l denotes the total array length and λ is the wavelength in free space

polynomial expansion to determine the distribution coefficients. These two methods require mathematical manipulations with similar results as the Taylor method, so they become less appealing in comparison with simplicity and computability of the Taylor method. The Taylor distribution, on the other hand, is easily computable using closed-form expressions. The equations used for calculating the Taylor line-source model are given here. The general expression for the Taylor line-source placed along the z-direction is

$$I(z) = \frac{1}{l}\left[1 + 2\sum_{p=1}^{\bar{n}-1} SF(p, A, \bar{n}) \cos\left(2\pi p \frac{z}{l}\right)\right] \tag{1.5}$$

where $\bar{n}$ is the number of side lobes with a constant level. Space factor, $SF(p, A, \bar{n})$, is given by

$$SF(p, A, \bar{n}) = \frac{[(\bar{n}-1)!]^2}{(\bar{n}-1+p)!\ (\bar{n}-1-p)!} \prod_{m=1}^{\bar{n}-1}\left[1 - \left(\frac{\pi p}{u_m}\right)^2\right], \quad |p| < \bar{n} \tag{1.6}$$

and u_m takes the form

$$u_n = \pi \frac{l}{\lambda} \cos\theta_n = \begin{cases} \pm\pi\sigma\sqrt{A^2 + \left(n - \frac{1}{2}\right)^2} & 1 \le n < \bar{n} \\ \pm n\pi & \bar{n} \le n \le \infty \end{cases} \tag{1.7}$$

In the above formula, $\sigma = \frac{\bar{n}}{\sqrt{A^2 + \left(\bar{n} - \frac{1}{2}\right)^2}}$ and A is a constant related to the maximum desired side lobe level or voltage ratio, R_o, given by $\cosh(\pi A) = R_o$. The amplitude

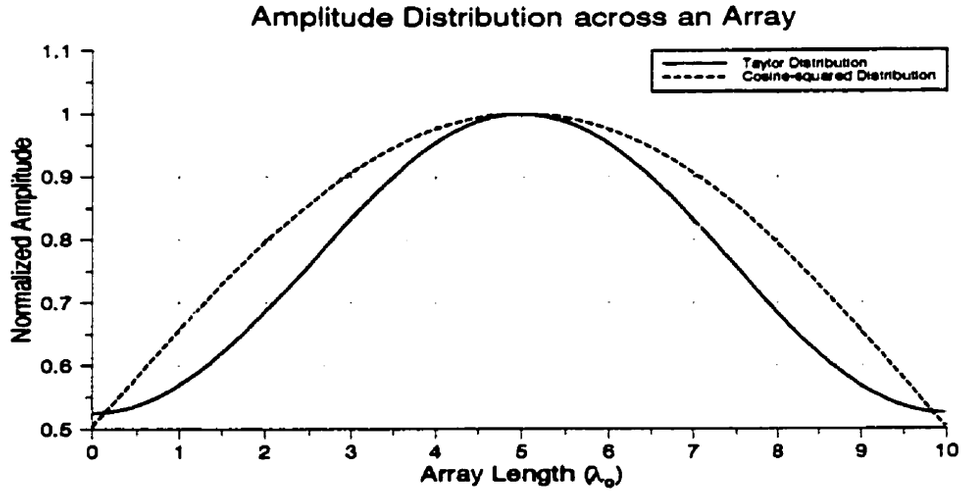

Number of elements=10; Taylor distribution for SLL=-20 dB and $\bar{n} = 3$

Figure 1.5: Taylor and Cosine-squared distributions

distribution across an array of 10 elements and minor lobes at -20 dB ($\bar{n} = 3$) and that of cosine-squared are given in Figure 1.5.

To demonstrate the effect of array factor with different distributions, the three distributions have been contrasted in Figure 1.6 for an array with rectangular microstrip elements. The dimensions of the patch are taken from single patch design explained in Section 2.3.1. The interelement spacing is approximately λ_g to match with the structure under simulation at 2 GHz discussed in Chapter 3.

1.7 Software Description

Throughout the study, a recently available software, **Ensemble** [10], which is capable of simulating multi-layer printed structures is employed . **Ensemble** uses the Method of Moments (MoM) to solve a Mixed-potential Integral Equation (MPIE) and to calculate the current density on predefined patch shapes. The mathematics comprising the basis functions and excitation models is an involved subject and the reader is referred to [11] for detailed discussion. Three commonly defined rectangular, triangular and circular shapes could be used in the design configuration. **Ensemble**

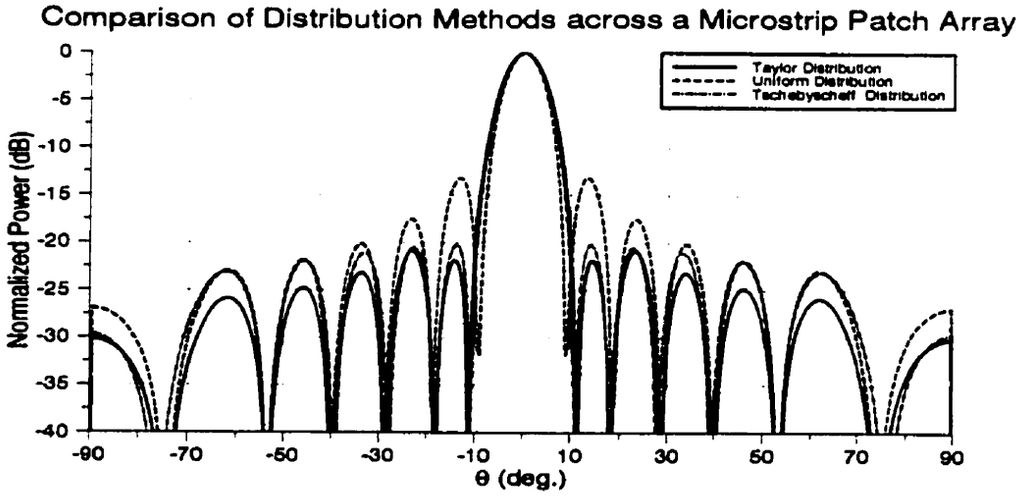

Taylor distribution: SLL=-20 dB, $\bar{n}$=3; Tschebyscheff distribution: SLL=-20 dB
Figure 1.4.(a), y-polarized excitation (W_p = 37.5 mm, L_p = 41.3 mm, h=1.524 mm, ϵ_r = 3.2)

Figure 1.6: Far-field Patterns of Uniform, Taylor and Tschebyscheff Distributions across a 10-element Array

utilizes a meshing routine which subdivides the configuration under simulation such that the number of segments increase at junctions of any patches and at the probe contact. Although user can adjust the cell size for each segment, software provides an optimal cell size at the operating frequency. In depth familiarity with **Ensemble** revealed that any kinds of shapes may be configured by changing the geometry file. A snapshot of the workspace window of the software is shown in Figure 1.7.

Ensemble outputs four types of measurements regularly used in antenna design. They are S- and Z-parameters, radiation patterns and current distributions on the metallic surface. S-parameters which determine the reflection and transmission coefficients respectful of the number of ports used, are stored in a designated file. Similarly Z-parameters corresponding to impedance of the structure at each port are saved under another file category with different file extension. **Ensemble** also provides radiation pattern and current density distributions for one frequency or a range of frequencies when options for creating such files are chosen. All the data files created by **Ensemble** can be graphed by plotting outputs of the software. Direct view of

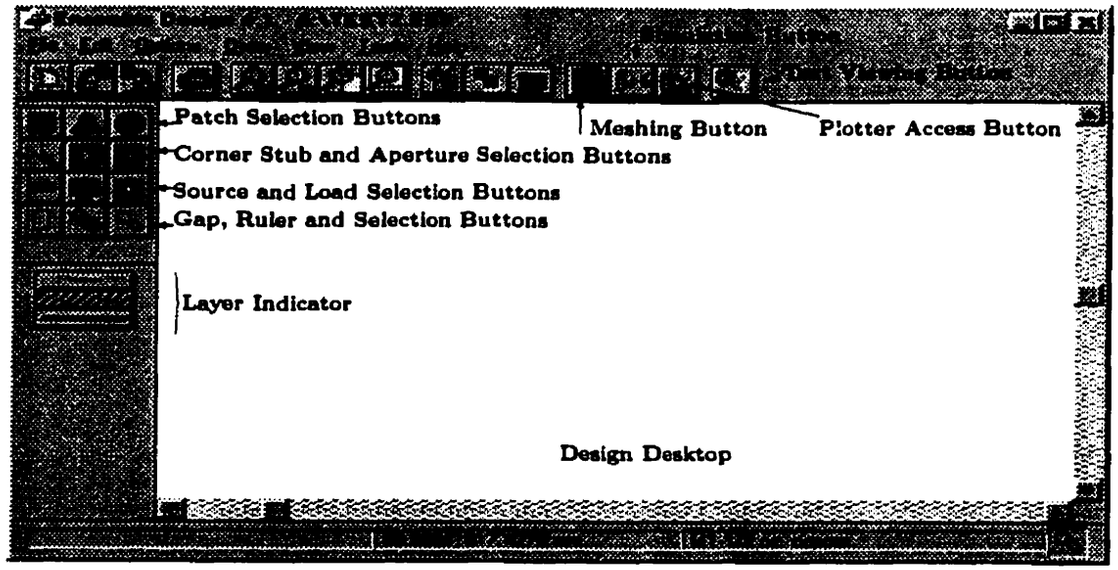

Figure 1.7: **Ensemble** workspace window

data files are also possible through a button in the top menu bar facilitating opening of text version of data. It is worthwhile to mention that although **Ensemble** provides nearly accurate results for multi-layer planar structures, it has its own limitations. Beside some software defects in the versions used for the study, **Ensemble** suffers from shortcomings such as considering only the infinite ground-plane and dielectric layers, inability to handle 3-dimensional structures as well as multiple probes beyond the first layer.

We can consider the case of infinite ground-plane sufficiently precise compared to the actual finite size to be able to carry out the study.

Our configuration consists of only planar structure with single dielectric layer, which **Ensemble** easily handles.

1.7.1 Software/Hardware Limitation

Ensemble , like any software, has its limitation and shortcomings. Some of the limitation comes from the hardware constraints such as memory capacity and internal speed while others are software dependent. For version 4.02 on a Pentium 90 MHz, memory shortage occurred for problem sizes beyond 2000 and time required to solve

a problem of size 1000-1500 is about 5-10 minutes per frequency.

Beside the hardware restraints, **Ensemble** suffers from very inflexible meshing routine and very sensitive to segmenting schemes. To illustrate this drawback, a single patch is simulated with different meshing sizes and schemes.

For this configuration, a single rectangular patch in proximity of a feedline, the intensity of meshing provides incompatible results. In most cases the optimal cell size suggested by the software results in deviation from the converged solution. This could be the result of narrow rectangular cells along the feedline. The instruction manual warns about avoiding very narrow triangular segments in order to avoid ill-conditioned matrices. By dividing the feedline into two separate strips, symmetrical segments were achieved but this slightly altered the solution under the same cell size.

Smaller cell size converges into one solution for three different meshing scheme, which is entirely at another frequency. This indicates that some deviation from the converged solution is expected when optimal cell size is used. Especially for large configurations, even using optimal cell size require long computing time.

Throughout the study the optimal cell size is mostly used, which is slightly off from the converging solution (as shown in Figure 1.8).

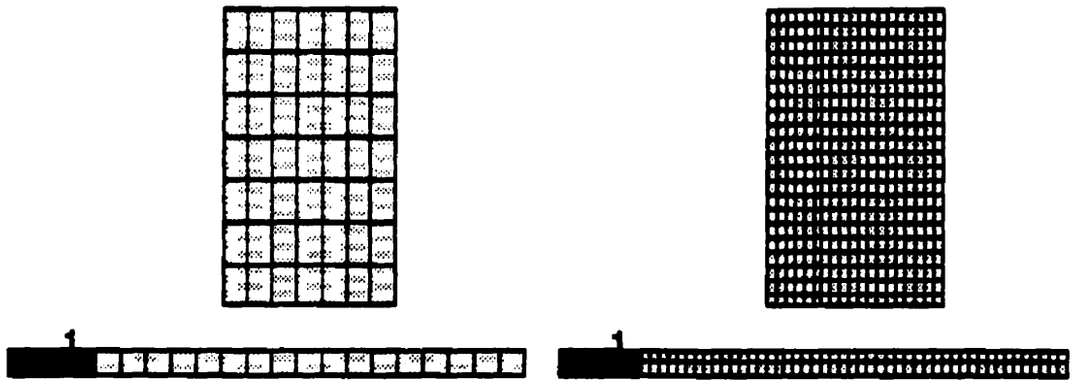

(a) Single patch with cell size=5.5 mm (b) Single patch with cell size=2.0 mm

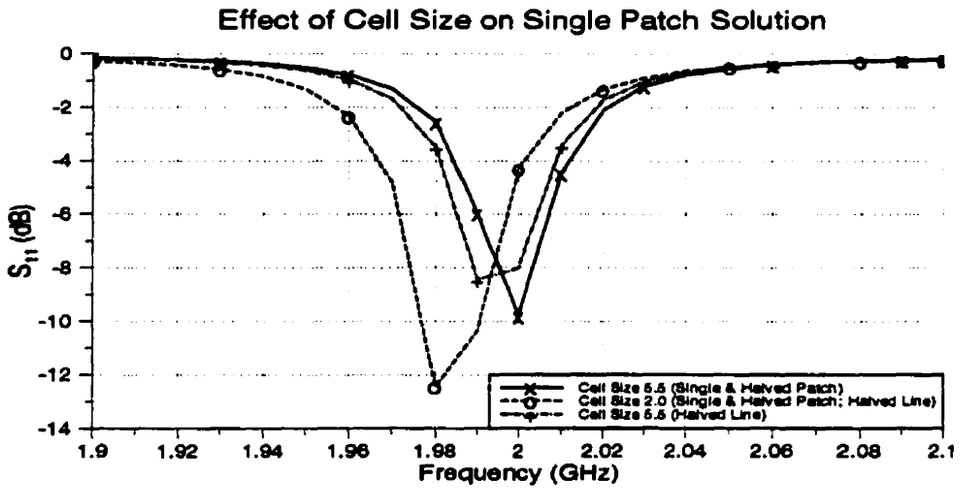

$\epsilon_r = 3.2$, $W = 3.6$, $L = 93.2$, $W_p = 37.5$, $L_p = 41.3$, $h = 1.524$ (Dimensions in mm)

Figure 1.8: Trend of Reflection Coefficient of Single Patch with Various Meshing Schemes (Refer to Figure 2.4 for parameters)

Chapter 2

Single Patch Design Curves

2.1 Introduction

The proximity coupled single element is the focus of the study in this chapter. The problem consists of a transmission line which provides coupling and distribution of the power and a patch (or series of patches) placed near the feedline where coupling takes place through proximity. The proximity coupling is mainly due to fringing fields spilling out at the edge of the feedline or the magnetic field surrounding the feedline. Figure 2.1 indicates the arrangement of the elements and feedline, where patches may be placed to create y- or x-directed polarization. The relation between the coupled power and the gap distance, d, is investigated in following sections. The resonant patch dimensions at the desired frequency should be determined first and then various design curves are derived for specific resonators.

2.2 Preliminary Specifications

At this stage some specifications are considered to begin the study and design. For ease of construction and lower cost, the operating frequency is decided to be 2.0 GHz. The availability of material then determined some parameters such as substrate thickness, h, of $0.06" = 1.524$ mm, with dielectric constant $\epsilon_r = 3.2$ and loss tangent of $\tan\delta = 0.008$ at 10 GHz. The parameters mostly used in simulation are

- Dielectric constant, $\epsilon_r = 3.2$

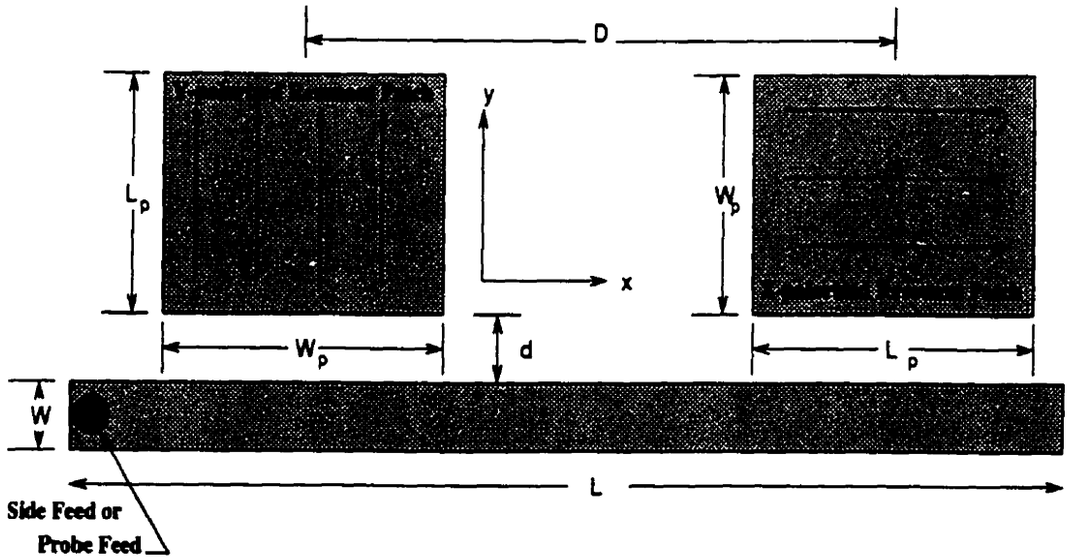

Figure 2.1: Patch and Feedline Configuration

- Substrate thickness, $h = 1.5$ mm (unless physical value used for comparison purpose)
- Loss tangent, $\tan\delta = 0.008$ (when lossy material is considered)
- Guided wavelength, $\lambda_g = 93.9$ mm (for $W = 3.6$ and $h = 1.5$ mm)

2.3 Y-polarized Resonant Patch Design

A resonant rectangular patch shows slight differences in all parameters when placed in the proximity of a feedline than when the same rectangular patch is fed directly. The resonant dimensions of rectangular patches in proximity of feedline are investigated next. Three cases of rectangular patches having different patch width to guided wavelength ratios are considered here. The convention used here is the resonant patch width to the feedline guided wavelength, λ_g.

2.3.1 Rectangular Patch ($\frac{W_p}{\lambda_g} \approx 0.4$) with Standing-wave Feeding

The following design is based on an open-circuited transmission line, which supports a standing-wave along its length. For the constructive reflection, the voltage standing-wave (VSW) is maximum at $\lambda_g/2$ intervals from each ends a feedline with length of λ_g multiples. The current standing-wave simultaneously exists on the line with 90° out of phase with respect to the VSW. This phenomenon is illustrated in Figure 2.2 where the short-circuited case is also shown. A design based on an open-ended feedline can easily be applied to the traveling-wave feedline where the consideration of maximum voltage locations is no longer required.

From the discussion in section 1.4.1 and Figure 2.2, we know that the maximum field occurs at $\lambda_g/2$ multiples from the end point. The voltage is directly proportional to the electric field, while current has direct relation to the magnetic field. These relations provide us with understanding the method of coupling; by fringing electric field or magnetic field couplings.

In order to determine the resonant dimensions, the material parameters given in Section 2.2 and Equations 1.3 and 1.4 are used to calculate the physical length for an arbitrary width. To design a rectangular patch, $W_p = \lambda_d/2 = \frac{\lambda_o}{2\sqrt{\epsilon_r}} = 41.90 \approx L_p$ mm is used as the first estimate. Considering the effective length to be optimal length of $\lambda_g/2$, the actual physical length of $L_p = 41.66$ mm is obtained. Resonant frequency of a square patch with the computed length is simulated next. The **Ensemble** result without any matching is shown in Figure 2.3 which employs the direct-fed configuration.

When the same patch is laid out in capacitive coupling configuration (Figure 2.4) where the current is induced due to fringing fields, the resonant frequency is shifted to some degree. This effect is due to the change in impedance; mainly introduction of mostly capacitive reactance into the overall impedance and distribution of edge impedance of patch over a wider area in comparison with the impedance seen by direct connection of transmission line to patch could be the major shift in resonance.

When the resonant length is along the y-direction, the patch should be centered

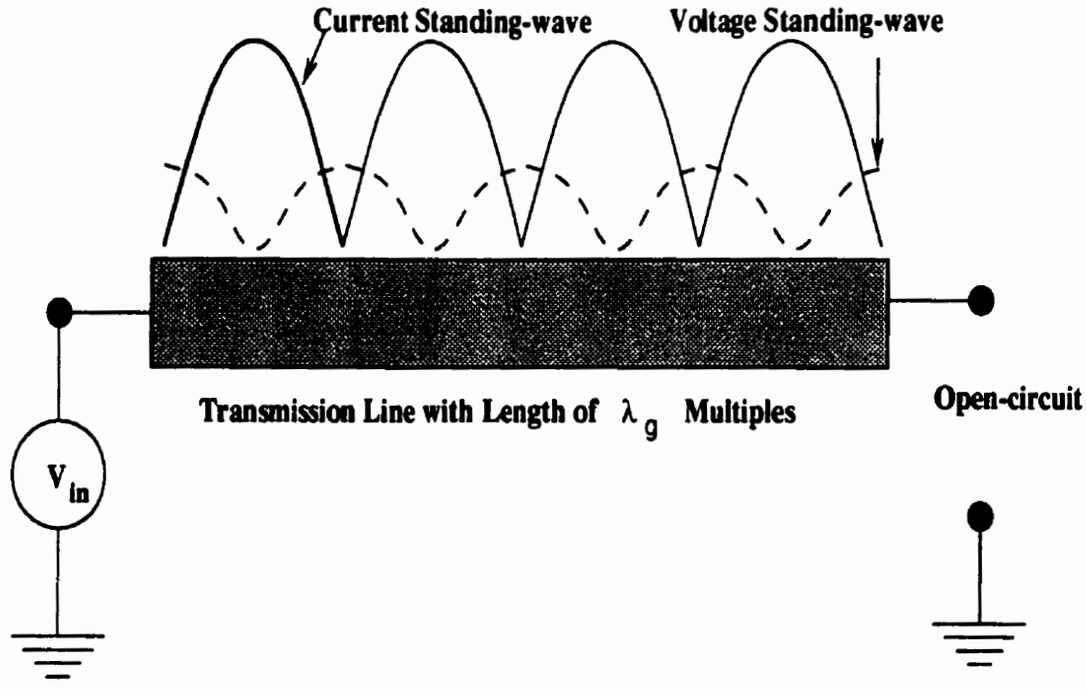

(a) Open-circuited Transmission Line

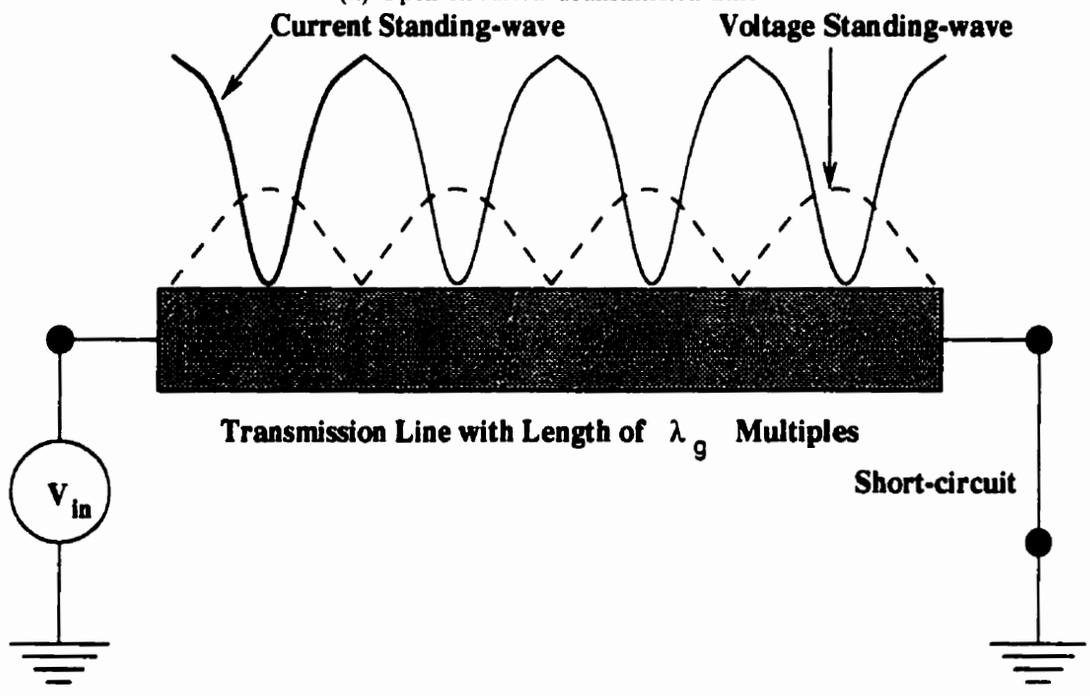

(b) Short-circuited Transmission Line

Figure 2.2: Standing-wave Patterns Created by Two Different Line Terminations

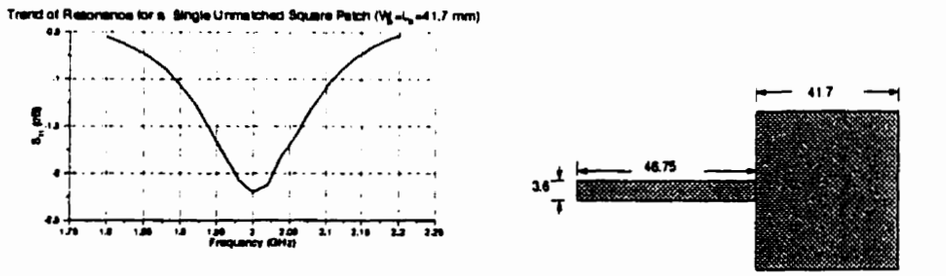

(a) Reflection Loss of Direct-fed Patch (b) Configuration of Single Square Patch

Figure 2.3: Single Square Resonant Patch

at the maxima of voltage standing-wave. For x-polarized radiating edges, the current standing-wave (and its corresponding magnetic field) is the source of coupling to the patch meaning patches should be placed at current maxima. In case of traveling-wave the position of current and voltage maxima are unnecessary.

Based on the open-ended feedline, simulation results for a feedline with $L = 92.7$ mm when probe-fed at one end having open-circuit impedance. This length differs from $L = 93.9$ mm calculated in Section 1.4.1 owing to the probe feed and its model used in the software. For clarity the geometry of the single patch configuration is shown in Figure 2.4 indicating also the orientation of coordinates.

With the length of open-ended feedline to be λ_g, the patch is placed at the center of line with an arbitrary gap distance and the length is reduced until the resonance frequency is shifted toward the desired one (Figure 2.5.a).

When the resonance is adjusted by trimming the length, the square patch becomes rectangular having a width slightly larger than the length. This feature exhibits a high level of cross-polarization which is already in excess due to the structure (i.e. the surface current created on the patch is normal to the current flowing in x-direction on the feedline). To reduce the cross-polarization, it is preferred that the width is kept smaller than the length.

From Figure 2.5.(a), it is obvious that for every 0.2 mm (about 0.5%) change in length there is a shift of 10 MHz in the resonant frequency.

Figure 2.5.(b) indicates the degree of frequency shift when the width is properly adjusted. There is an optimal width associated with the given length where further

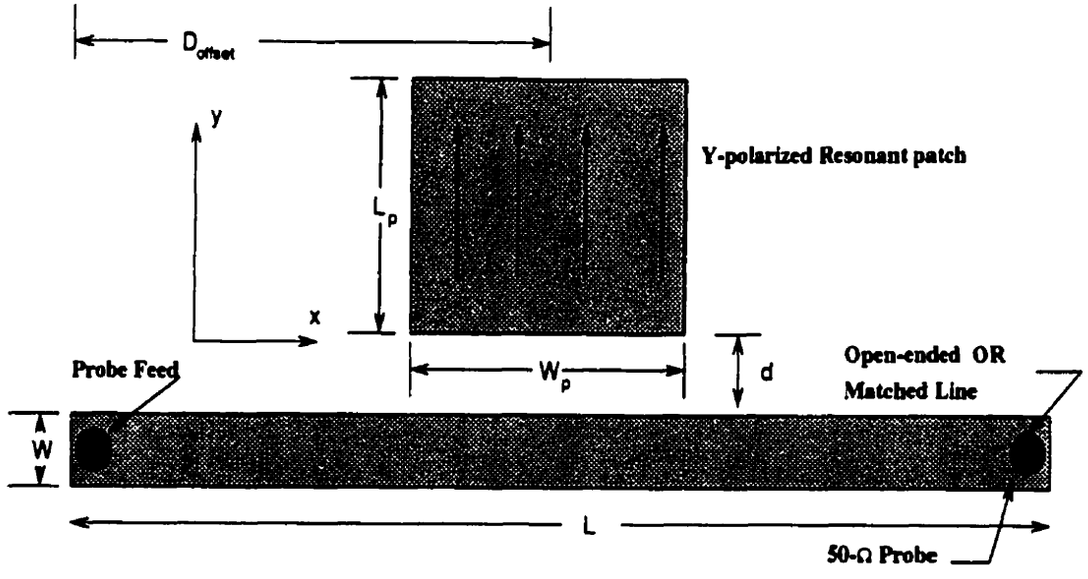

Figure 2.4: Geometry of a Y-polarized Single Patch in Proximity of a Feedline

reduction causes a shift in frequency. The width adjustment has less significance on the resonance shift and is considered as fine tuning of resonant element. It is noticeable that more than 10% change in width is required in order to shift the resonant frequency by 10 MHz.

The final design dimensions are determined as $W_p = 37.5$ and $L_p = 41.3$ mm. Of course these dimensions serve only as preliminary design data and any attempt for matching the antenna seems unnecessary.

These dimensions are used throughout the study for a rectangular patch. In case of an open-circuited feedline, the standing-wave along the feedline is probed at the center of the patch by measuring the current amplitude on the patch for various offset locations along the feedline. The normalized amplitude and phase of the current are displayed in Figure 2.6.

2.3.2 Narrow Rectangular Patch ($\frac{W_p}{\lambda_g} \approx 0.1$)

By reducing the width of the rectangular patch further, or equivalently forcing the induced current to be more directive toward the radiating edges, the cross-polarization level decreases significantly. The price paid for lower cross-polarization is a weaker

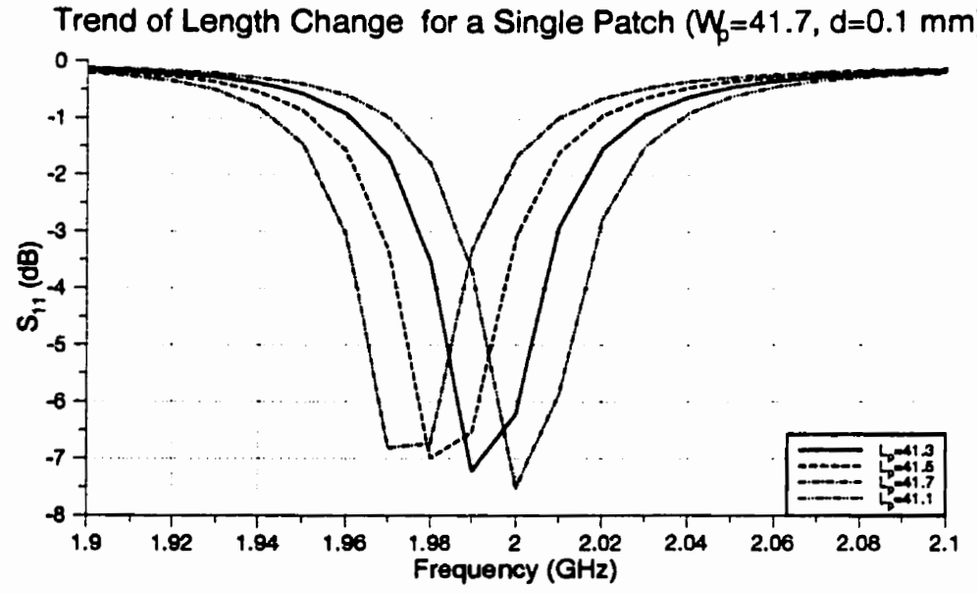

(a) Effect of Length Change on Resonance Shift

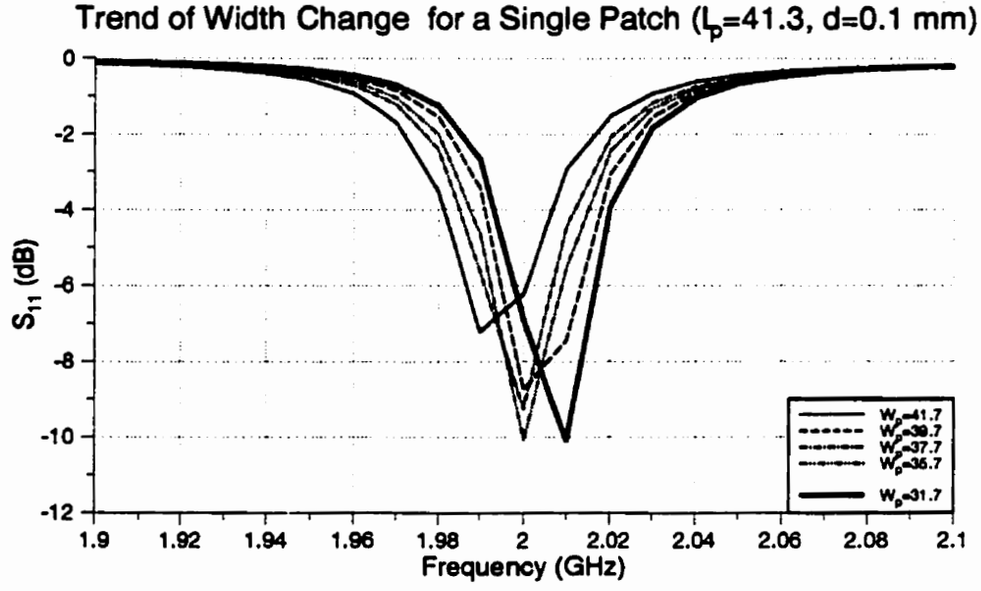

(b) Effect of Width Change on Resonance Shift

Figure 2.5: Effect of Size Trim on Frequency Shift for a Single Patch with Open-ended Feedline

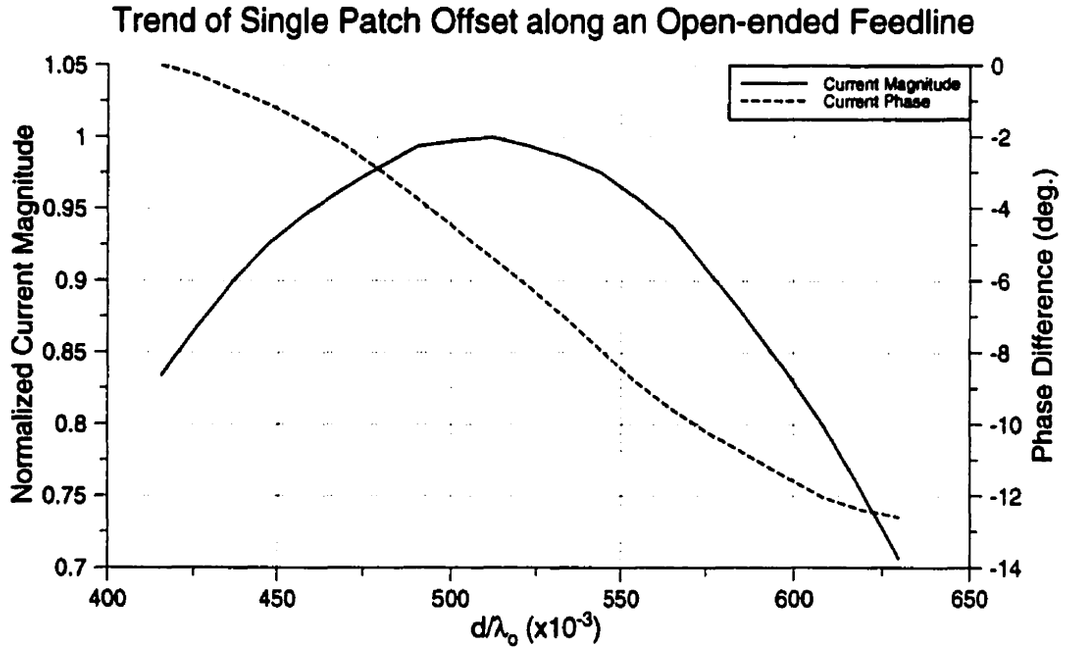

Dimensions (mm): $W = 3.6$, $L = 93.2$, $W_p = 37.5$, $L_p = 41.3$, $d = 0.005$
The current component J_y is taken at the patch center in Figure 2.4

Figure 2.6: Current Measurement on a Resonant Patch at Various Offset Distances

coupling between the patch and feedline. This results in a longer array.

An arbitrary width of 10 mm is chosen, which is near the criteria for printed dipoles ($W_p \leq 0.05\lambda_o$).The resonant size at the desired frequency is then determined by a proper adjustment of the length. Figure 2.7 shows the design results which arrives at resonant dimensions of $W_p = 10$ and $L_p = 43.3$ mm. The value obtained from length calculation is 43.43 mm which is in good agreement with the value obtained by successive trial procedure. This resonant size is used for the narrow patch.

2.3.3 Wide Patch Resonator ($\frac{W_p}{\lambda_g} \approx 0.8$)

In order to create more general sets of curves, another resonant patch with patch width exceeding $\lambda_g/2$ is considered. Following the same design procedure, dimensions of $W_p = 74.5$ and $L_p = 40.6$ mm are obtained. The results of three resonant patches

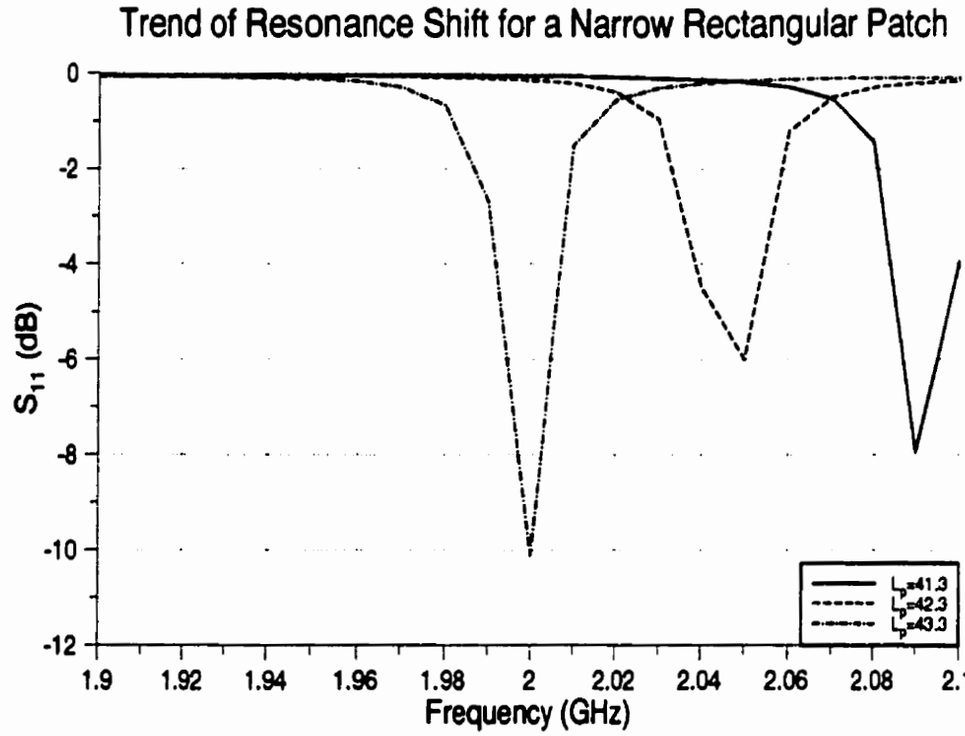

Dimensions (mm): $W = 3.6$, $L = 92.7$, $W_p = 10.0$, $d = 0.1$

Figure 2.7: Resonant Frequency Shift of Narrow Rectangular Patch with Open Termination

are summerized in Table 2.1.

2.4 X-polarized Resonant Patches

When the resonant current induced on the patch is normal to the current on the feedline (y-polarized), the abrupt change of direction introduces cross-polarization including the feedline radiation in the far-field. Beside many techniques to lower the cross-polarization, the case when the resonant current on the patch is in the same direction as the current on the feedline is expected to lower the cross-polarization. The x-polarized resonant patches reduce the high cross-polarization when the patch size falls within the approximate limit $\frac{W_p}{\lambda_g} \leq 0.5$. The findings reveal that the x-polarized

Table 2.1: Summary of Resonant Patch Dimensions at 2.0 GHz

Patch Type	W_p (mm)	L_p (mm)
Narrow Patch	10.0	43.3
Rectangular Patch	37.5	41.3
Large Patch	74.5	40.6

patch has better coupling when its center is placed at maximum standing-wave current where magnetic fields coupling to the patch result in excitation of resonant current. The reader is referred to Figure 2.1 for the x-polarized geometry and conventional parameters.

2.4.1 X-polarized Narrow Patch ($\frac{W_p}{\lambda_g} \approx 0.1$)

In design of x-polarized narrow patch, the same patch values as the y-polarized narrow patch can be used as the estimate dimensions and the resonant length can be found when the width is kept at the fixed value of $W_p = 10.0$ mm. Figure 2.8 displays the approach to the final width value. Geometry of Figure 2.4 is used with the difference of a x-polarized patch positioned at the center of a short-circuited feedline. Here the notation of length and width is interchanged as presented in Figure 2.1. This is to keep consistent with the terminology of rectangular patch that width refers to the side where radiating edges exist and length is the distance between these two edges.

2.4.2 Patch Dimensions with Traveling-wave Feeding

The dimensions used for the three types of rectangular resonators remain almost the same whether coupling is due to standing-wave or traveling-wave. When the feedline is matched at the far end, there exists a traveling-wave along the transmission line. In contrast to the standing-wave feeding, the patch locations become arbitrary and there would be no need to determine the feedline's exact length corresponding to multiples of λ_g. The drawback of this feature is the amplitude decay in comparison to standing-wave case and the difference in interpretation of results.

Because there is no constructive reflection from matched feedline, the voltage

2.4.3 Circuit Analysis of Configuration

Another approach for the analysis of the configuration is to consider the equivalent circuit of the structure. As mentioned in the previous section, the radiation of a rectangular patch is mainly due to the radiating slots at two edges separated by the patch length. The equivalent circuit of a radiating slot is modeled as an impedance. When the electrical patch length is chosen to be $\lambda_g/2$, the imaginary parts of radiation impedances become 180° out of phase, and cancelled out in addition of impedances. The real impedance, known as radiation resistance is shown as a lumped resistor in the circuit. The impedance of the metallic patch is calculated using the transmission line equations. This equivalent circuit is shown in Figure 2.9.a where the total real radiation resistance is divided into two parallel components. The empirical equations for computing the approximate radiation resistance is given as [12]

$$R_{rad} = \begin{cases} 90\left(\frac{\lambda_{eff}}{W_p}\right)^2 & \text{for } W_p \leq \lambda_o \\ 120\left(\frac{\lambda_{eff}}{W_p}\right) & \text{for } W_p \geq \lambda_o \end{cases}$$

The above formulae is used along with the transmission line model of the patch on **Libra** [13]. **Libra** is a software used mainly in circuit design and is capable of analysis and optimization of vast range of electronic and microwave circuits. The software employs circuit elements or equivalent models as means of analysis. The main purpose of this attempt was to verify the approximate model of the proximity coupling as a shunt capacitance at points along the feedline (Figure 2.9.b). A simple formula for computing the parallel plate capacitance is used to model the coupling capacitance and to determine its value with minor modifications. The well-known capacitance equation,

$$C = \frac{\epsilon_o \epsilon_r A}{d} \implies C_c = \frac{\epsilon_o \epsilon_{eff} W_p t}{d}$$

was redefined as C_c where effective dielectric constant (see Equation 1.3) replaces ϵ_r to account for the inhomogeneous nature of structure, t and W_p represent the feedline thickness and patch width respectively and d corresponds to the gap distance between patch and feedline. Parameters L_p and L in Figure 2.9 denote the same parameters as in Figure 2.4 where feedline length, L, is chosen to be λ_g long.

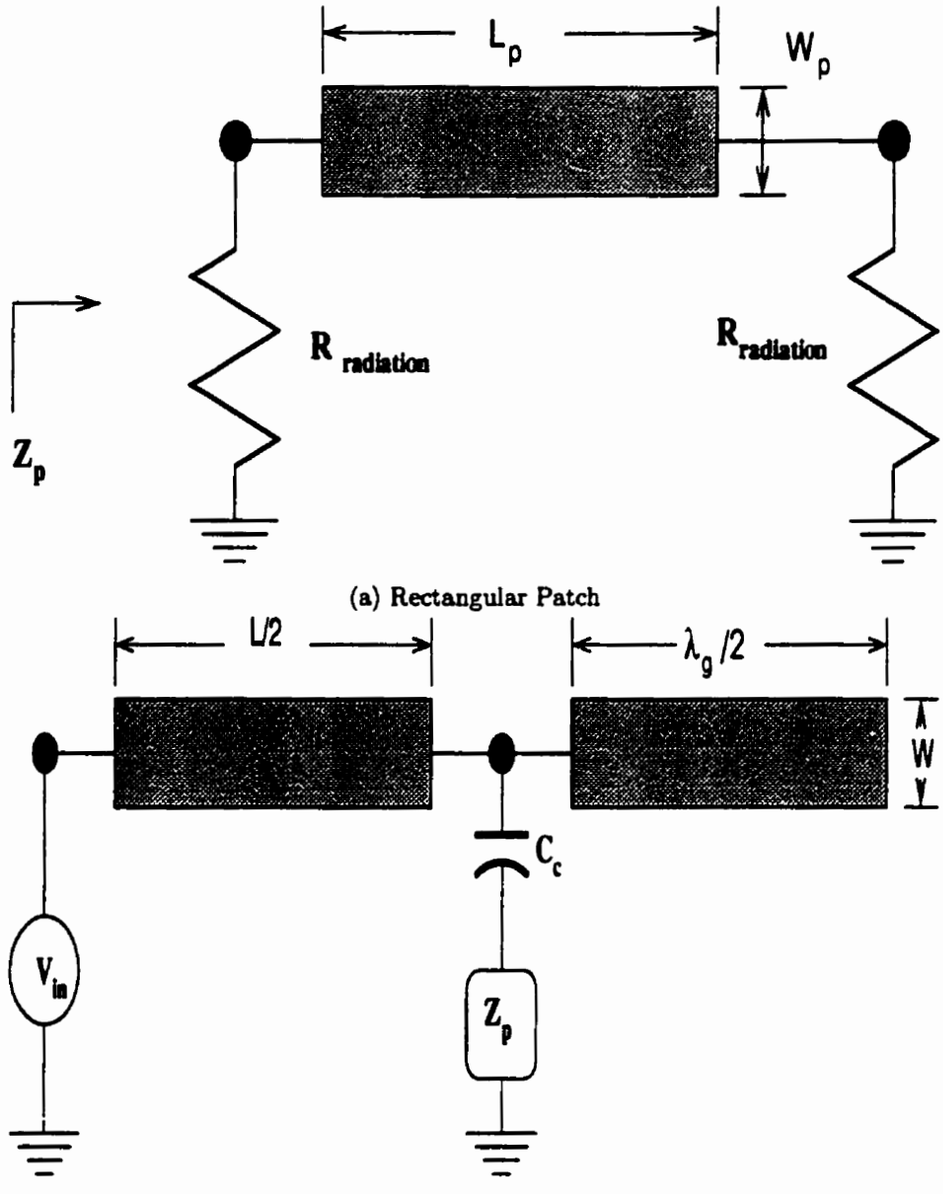

(a) Rectangular Patch

(b) Capacitively-coupled Patch

Figure 2.9: Equivalent Circuit of a Single Rectangular Patch, When Placed in Proximity of Open-ended Feedline

This simple model was simulated on **Libra** and the outcome is in fair agreement with that of **Ensemble** . The comparison between the two results indicates a difference in magnitude and resonant frequency when exact parameters are considered. The optimal length of 43.0 mm is obtained by allowing only the patch length to be varied within a reasonable range. The optimal length shifts the resonance of the circuit to the resonant frequency which coincides with results obtained by **Ensemble** as shown in Figure 2.10. This difference in length reminds us of the fact that the effective length should be included in the equivalent circuit and that **Ensemble** accounts for the fringing length. Using Equation 1.4, an effective length of 43.07 mm which is in agreement with the optimal length achieved by **Libra** is calculated.

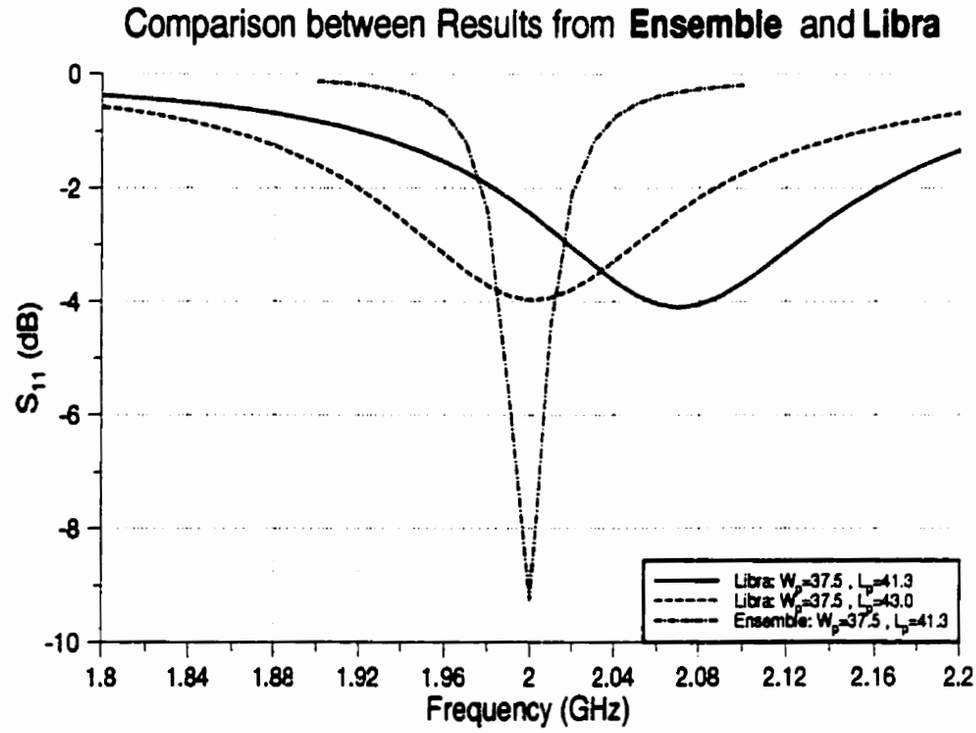

Dimensions (mm): $W = 3.6$, $L = 92.7$, $W_p = 37.5$, $d = 0.1$, $t = 0.017$, $h = 1.588$, $\epsilon_r = 3.2$

Figure 2.10: Resonant Frequency of Structure under Simulation by both **Libra** and **Ensemble**

The above analysis provides a measure of correctness as well as an alternative approach if needed. It also brings some insight into the dominant electrical components and their corresponding equations.

The same analogy can be applied to the magnetically coupled x-polarized resonator. Similar to the capacitive coupling approach, it is suggested that two mutually coupled inductors (or a transformer) replace the coupling capacitance. The mutual coupling between two inductors should be related directly to the patch width and inversely to their separation.

2.5 Design Curves for Control Parameters

In this section, the effects of various parameters on a single patch configuration is discussed and the design curves which are used later in array design are presented. The geometry in Figure 2.4 is considered in this section to obtain the design curves.

2.5.1 Effect of Gap Distance on Coupled Power

The first parameter to be studied is the relation between the gap and the power coupled to the patch. In order to determine this, the current distribution on the patch at resonance frequency is computed while changing the gap distance, d. Since the radiated power is directly proportional to the square of the current, the y-polarized $\mathbf{J}_y$ at the patch center is selected to study the power coupled from the line to the patch. The relative coupling is then normalized to the maximum value which corresponds to the selected minimum distance of 0.005 mm.

Figure 2.11 displays the coupled power, the square of y-component current magnitude, for both standing- and traveling-wave scenarios. No significant difference in coupling is observed, which implies negligible effect of feeding scheme on the coupling.

To generate a broader set of design curves, three different resonant patch dimensions are considered, and it is reasonable to study the effect of gap distance on all three. These patch sizes can also be configured to generate the x-polarized resonant current. Minor adjustments tune the patch to the desired 2.0 GHz resonant frequency for the case of x-polarized resonant patches. Table 2.2 displays some important pa-

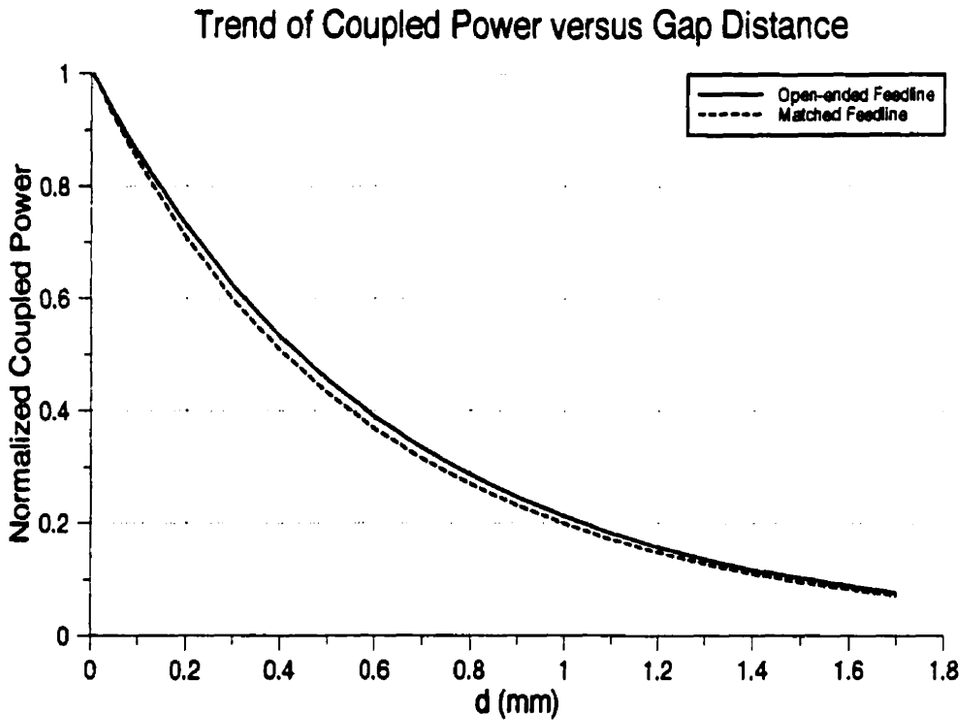

Dimensions (mm): $W = 3.6$, $L = 92.7$, $W_p = 37.5$, $L_p = 41.3$, $h = 1.588$, $\epsilon_r = 3.2$

Figure 2.11: Comparison of Coupled Power to the Patch as a Function of Gap Distance under Two Feeding Schemes for Geometry of Figure 2.4

rameters of different resonators which placed in proximity of feedline as shown in Figure 2.4. In case of x-polarized resonator, the open-end termination is replaced by a short-circuit while the single patch is centered along a λ_g long feedline.

The simulation reveals that different resonant patches exhibit distinct and different relationships between the coupled power and the gap size, d. This fact as shown in Figure 2.12 which indicates that for each patch a design curve specifically generated for that patch must be used.

When the phase change due to the gap size is considered, the computed results (Figure 2.13) indicate larger phase changes for y-polarized narrow patches and negligible phase differences for other rectangular patches . A phase difference of less than

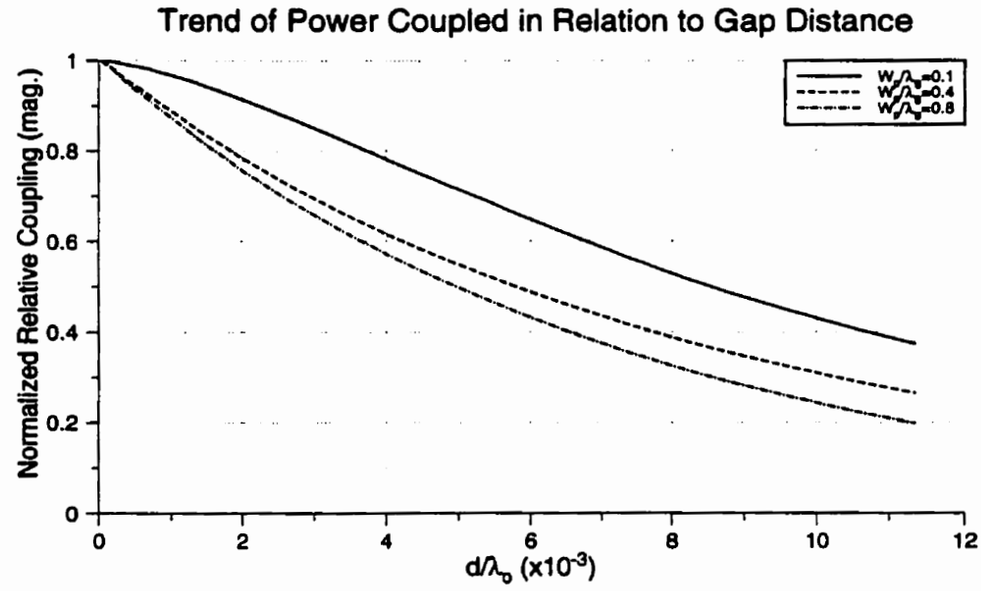

(a) Y-polarized Resonant Patches

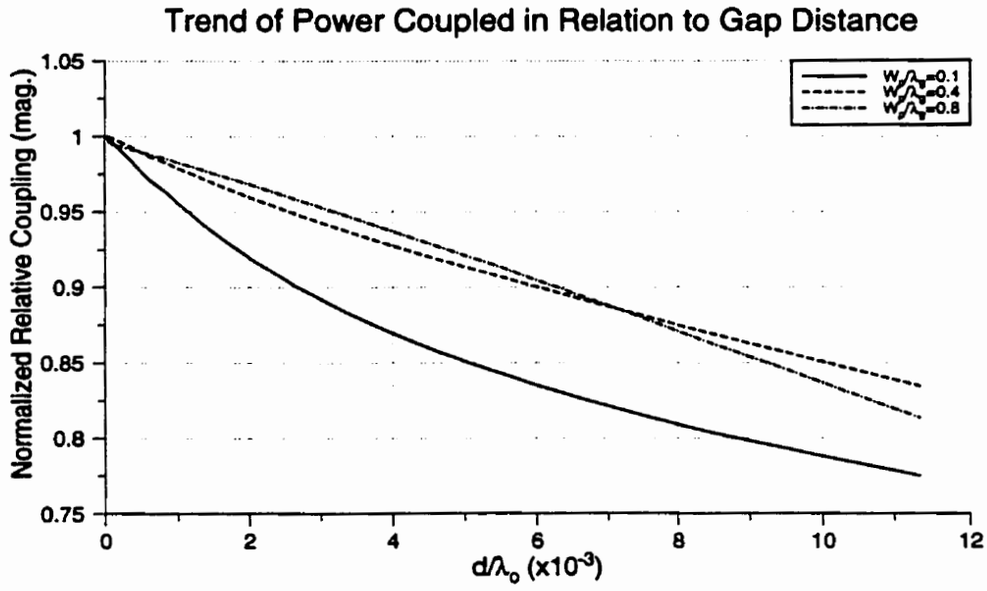

(b) X-polarized Resonant Patches

Figure 2.12: Design Curves of Single Resonant Patch in Proximity of Feedline

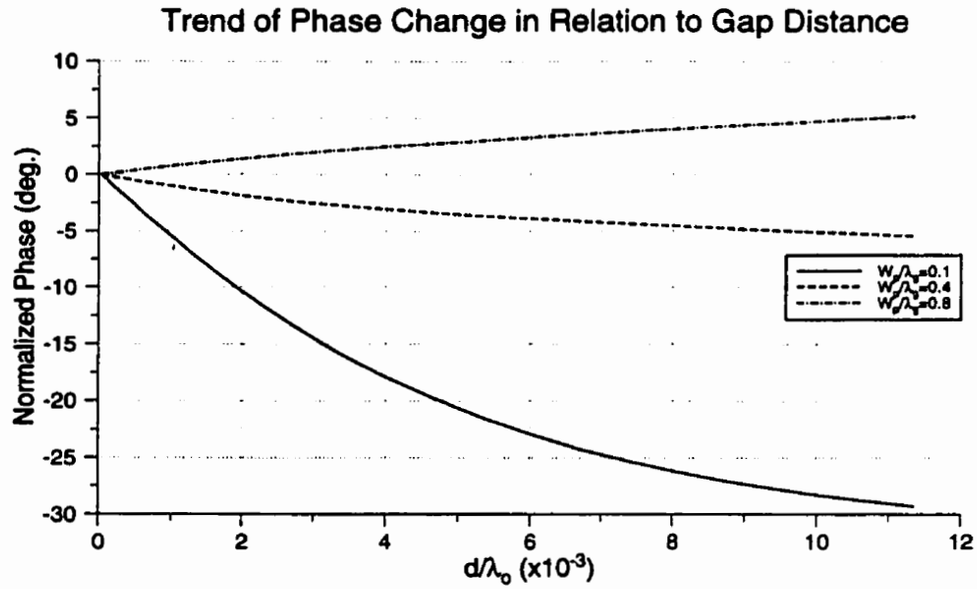

(a) Y-polarized Resonant Patches

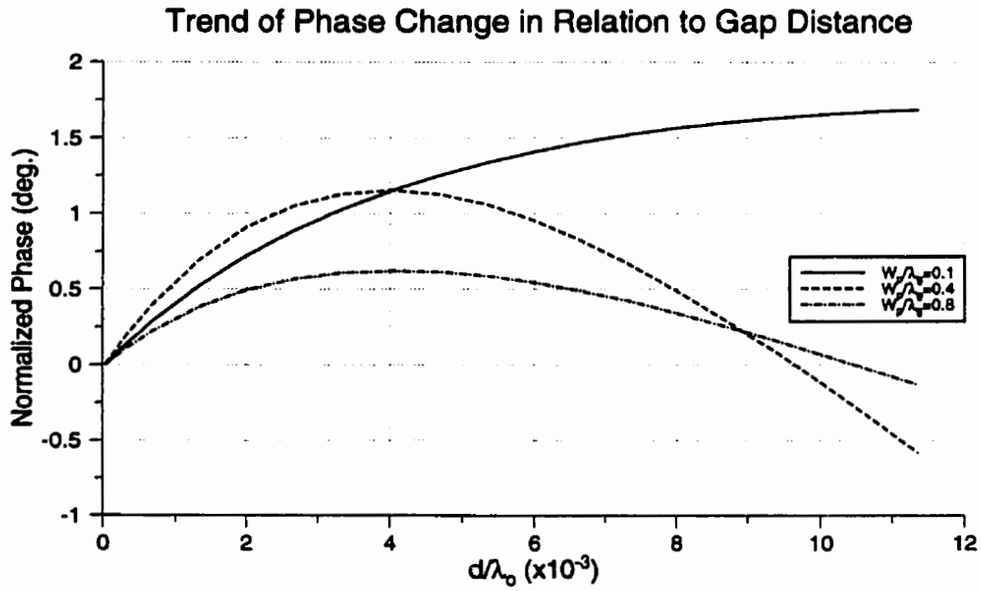

(b) X-polarized Resonant Patches

Figure 2.13: Phase Change due to Gap Distance

increase of width beyond the resonant width augments the overall impedance due to material and coupling resistance. Figure 2.14.(b) illustrates the phenomenon and similar trends exist for other patch sizes with different feedline terminations.

2.5.4 Effect of Patch Width on Gain

To investigate the gain for different resonant patches, other resonant dimensions are used and the gain and return loss for each case are attained. The geometry of Figure 2.4 is used with y-polarized resonant patches. Patch sizes beyond a guided wavelength exhibited negative gain but a resonance corresponding to the feedline resonance. This indicates that due to the cancellation of anti-phase current components the patch was actually ineffective in the configuration. The results (Table 2.3) indicate optimal patch sizes falling in the range of $0.1\lambda_g \leq W_p \leq 0.4\lambda_g$ and having a length of about $0.45\lambda_g$. The length values are the physical lengths and do not include the fringing lengths. This study also fortifies the choice of narrow width patches for achieving lower cross-polarization.

Table 2.3: Performance of Single Resonant Patch of Different Dimensions for Two Feeding Methods (Figure 2.4)

		Standing-wave Feeding		**Traveling-wave Feeding**	
W_p (mm)	**L_p (mm)**	**Gain (dBi)**	**S_{11} (dB)**	**Gain (dBi)**	**S_{11} (dB)**
5.0 ($\approx 0.05\lambda_g$)	45.0 ($\approx 0.48\lambda_g$)	4.92	-7.38	3.76	-13.74
10.0 ($\approx 0.11\lambda_g$)	43.3 ($\approx 0.46\lambda_g$)	5.99	-15.51	2.00	-11.30
25.0 ($\approx 0.27\lambda_g$)	41.8 ($\approx 0.45\lambda_g$)	6.14	-13.23	2.05	-11.78
37.5 ($\approx 0.40\lambda_g$)	41.3 ($\approx 0.44\lambda_g$)	5.99	-9.38	1.58	-13.56
46.5 ($\approx 0.50\lambda_g$)	41.1 ($\approx 0.44\lambda_g$)	5.61	-6.77	0.88	-15.44
74.5 ($\approx 0.80\lambda_g$)	40.6 ($\approx 0.44\lambda_g$)	-0.84	-0.81	-6.54	-30.35

Common Parameters in mm: $W = 3.6$, $L = 93.2$, $d = 0.1$, $h = 1.524$, $\epsilon_r = 3.2$

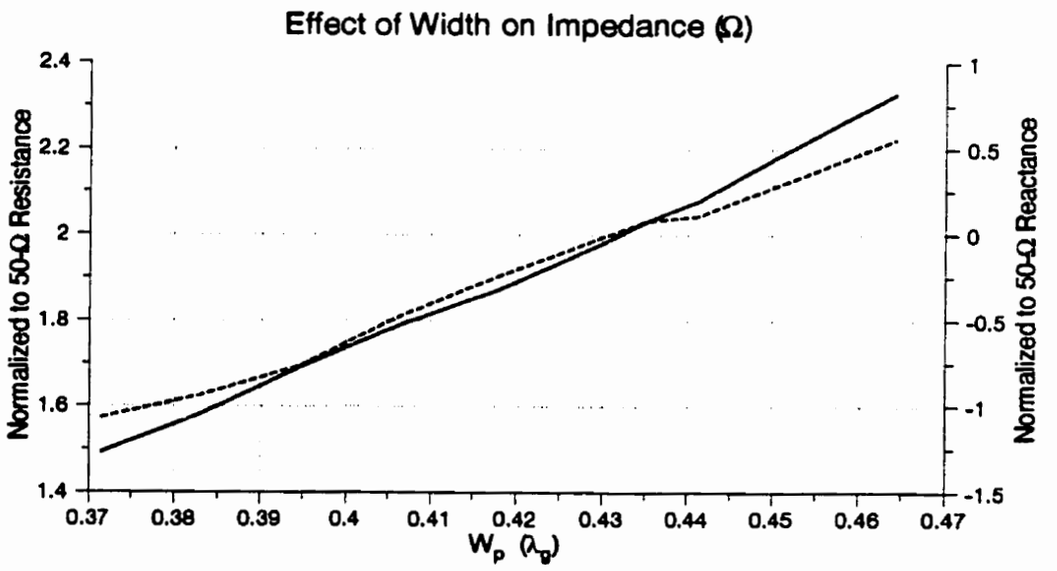

(a) Widths less than $\lambda_g/2$

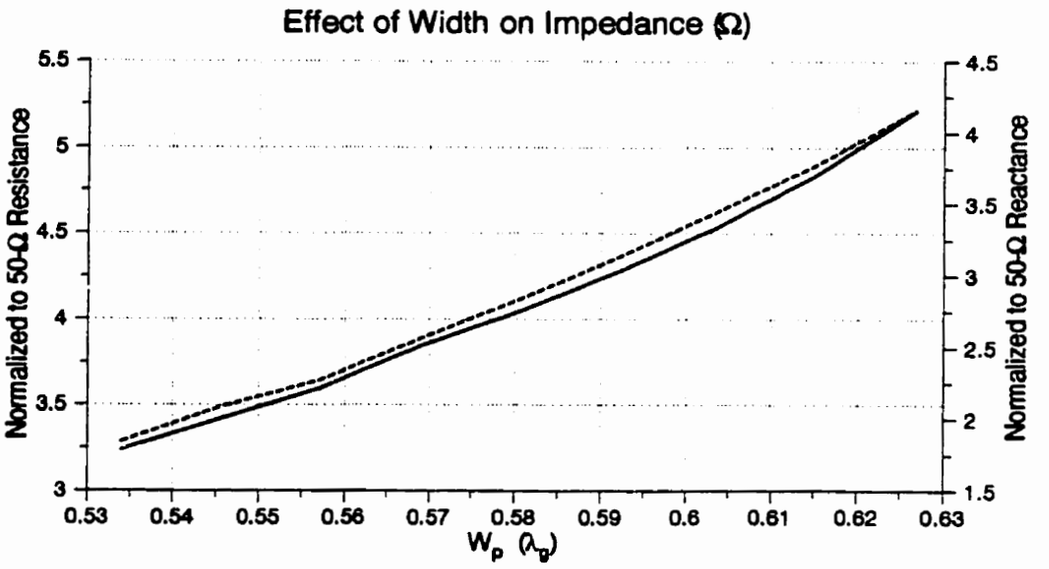

(b) Widths greater than $\lambda_g/2$

Dimensions (mm): $W = 3.6$, $L = 92.7$, $L_p = 41.3$ @ 2 GHz

Figure 2.14: Plot of Input Impedance versus Patch Width for Single Patch with Open-ended Feedline (Based on Figure 2.4)

2.5.5 Effect of Feedline Width on Coupling

A single element resonator is placed in proximity of feedlines with different widths (see Figure 2.4 for geometry). The feedline input impedance with no patch should be determined first for various line widths. Since an open-circuited termination and consequently standing-wave is used to excite the resonator in each case, minor adjustment of feedline length was also required to obtain an open-circuited feedline impedance. The following table (Table 2.4) reflects the simulation for coupling to a single patch in proximity of feedlines. The resonant current at the center of a y-polarized patch was computed and relative coupling for each case was normalized to the maximum value. This investigation indicates that narrower feedlines have higher coupling to the patch.

Table 2.4: Effect of Feedline Width on Coupling

W (mm)	Z_o (Ω)	L (mm)	Relative Coupling
0.95	100	97.4	0.99
1.8	75	95.8	1.0
3.6	50	93.2	0.93
9.5	25	88.8	0.79

Fixed parameters in mm: $W_p = 37.5$, $L_p = 41.3$, $d = 0.1$, $h = 1.524$, $\epsilon_r = 3.2$

Transmission line theory also reminds us of concentration of field at the edges as line width becomes narrower. Wider lines have lower impedances due to spread of current and field across line width. These results comply completely with the theory and reveal another factor affecting the coupling.

Chapter 3

Array Configurations

3.1 Introduction

In this chapter a linear array of 10 elements with standing-wave and traveling-wave feeding schemes are considered. First the cases of uniform and Taylor distributions across an array with standing-wave excitation are discussed and then the traveling-wave cases are studied. The cross-linear configuration, a specific arrangement for reducing the cross-polarization, follows next. Effects of mutual coupling and progressive width and length change on array performance are included in the respective sections. Dual configuration capability and relative simulations are also presented. The geometry of array with important parameters is displayed in Figure 3.1 and numerous references to this figure for the geometry and notation are made throughout the chapter.

In this study, the term λ_g which denotes the guided wavelength of the feedline and is calculated as $\frac{\lambda_o}{\sqrt{\epsilon_{eff}}}$ (see Equation 1.3), is repeatedly used. The guided wavelength is calculated for the feedline width in the structure and is the basis for determining the array phase distribution.

Throughout the design, the attempt to establish a uniform phase progression across the array is striven. For an array of 10 elements the phase dispersion along the feedline is not very effective but in design of larger arrays the phase dispersion factor should be considered. For the given specifications of dielectric constant, $\epsilon_r = 3.2$, and substrate thickness, $h = 1.524$ mm, λ_g for a 50Ω feedline with width $W = 3.6$ mm is

with the difference that the feedline has a length equal to $10\lambda_g$ and open termination. The input impedance of line alone at the source also falls on open-circuit (on a Smith Chart). The first patch location is $\lambda_g/2$ from the source and the patch is moved to positions at λ_g multiples.

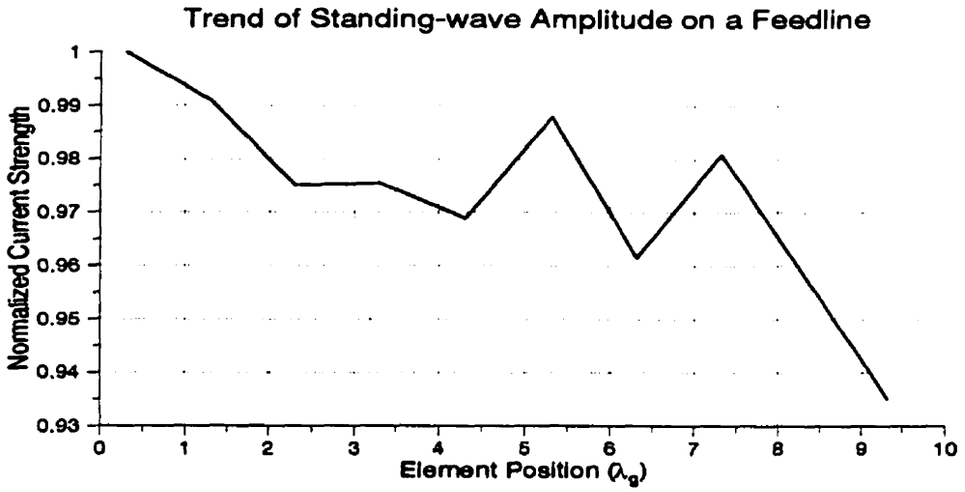

Dimensions (mm): $W = 3.6$, $L = 936.3 \approx 10\lambda_g$, $W_p = 37.5$, $L_p = 41.3$, $d = 0.1$, $D = 93.5$

Figure 3.2: Variation of Standing-wave Measured at the Center of a Single Patch Moved along an Open-ended Feedline at 2.0 GHz

As seen in Figure 3.2, the measured current magnitude on the patch is almost uniform along the feedline since the variation and the gradual decay of amplitude is negligible for approximate purposes. The phase alse remain almost constant with negligible fluctuation.

Throughout the simulation the feedline length is designed for the standing-wave case which can be converted to traveling-wave instance by a proper matching termination. In traveling-wave feeding scheme the position of elements along the feedline is arbitrary at the cost of a lower amplitude level and gradual decay toward the termination.

3.2.1 Uniform Distribution

The simplest configuration is the uniform distribution of amplitude and phase across the array of identical resonators. The inter-element spacing determines phase distribution which is considered free of dispersion for short arrays. For larger arrays the phase dispersion due to the material losses should be taken into account.

The dielectric loss is neglected throughout the simulation in order to discern the effect for the ideal situation. More realistic approach is considered in the next chapter.

An array of 10 elements with a fixed gap distance and constant inter-element spacing is chosen for the simulation purpose. Figure 3.3 includes the return loss and gain of the array as well as the current distribution across the array, measured at the center of each patch. There is a slight shift in the resonance frequency but the directivity is almost constant at around 15 dBi in the bandwidth which is about 1.5%. Based on Figure 3.3, the amount of power radiated can be calculated as

$$P_{rad} = 1 - |S_{11}|^2 = 1 - |0.2541|^2 = 0.935,$$

while the average coupling of 95% (about 90% power coupled) is read. Aperture theory also provides an estimate for the directivity which gives a measure of comparison with the simulated value. For the array of $936.3 \times (41.3 + 3.6)$ mm^2 at 2.02 GHz, the effective aperture is $(6.3\lambda_o) \times (0.5\lambda_o)$. when the effective aperture area is used in the equation given in Section 4.4.2, a directivity of 39.58 or 15.97 dBi is obtained which is close to 15.4 dBi simulation result.

The current distribution also indicates that not an exact uniform distribution is established across the array. On the average there is 5%-6% reduction in coupling from the source end to the termination. The phase distribution follows a decreasing trend which is dictated mainly by the inter-element spacing. In the above figure, the spacing between the elements is 93.5 mm which is slightly less than the 93.6 mm, the open-circuited feedline with $10\lambda_g$ length at 2.0 GHz. A uniform phase distribution can be achieved by better adjustment of inter-element spacing.

As shown in Figure 3.4 the expected side lobe level of -13.0 dB is achieved at the center frequency while the effect of frequency shift is also illustrated. At frequencies above and below the operating bandwidth, splitting of main lobe occurs. This is due

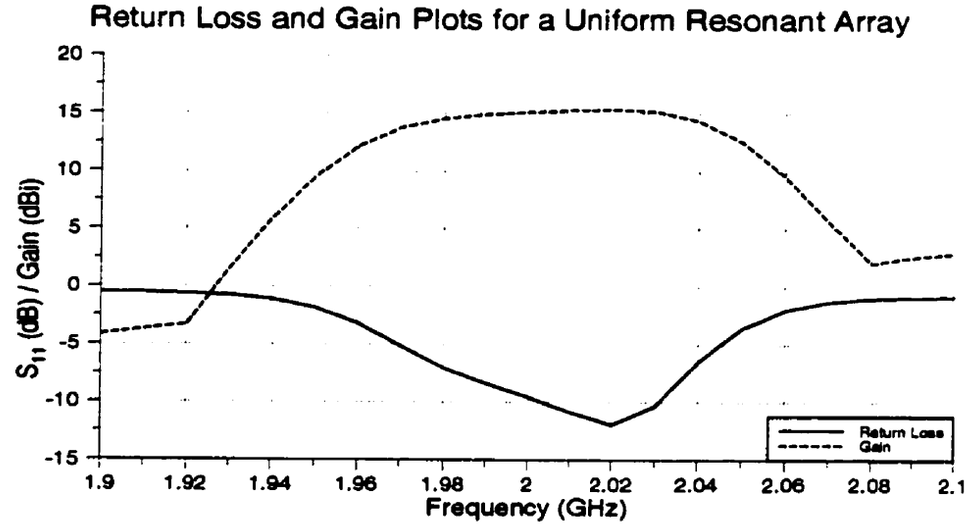

(a) Return Loss and Gain at 2.02 GHz

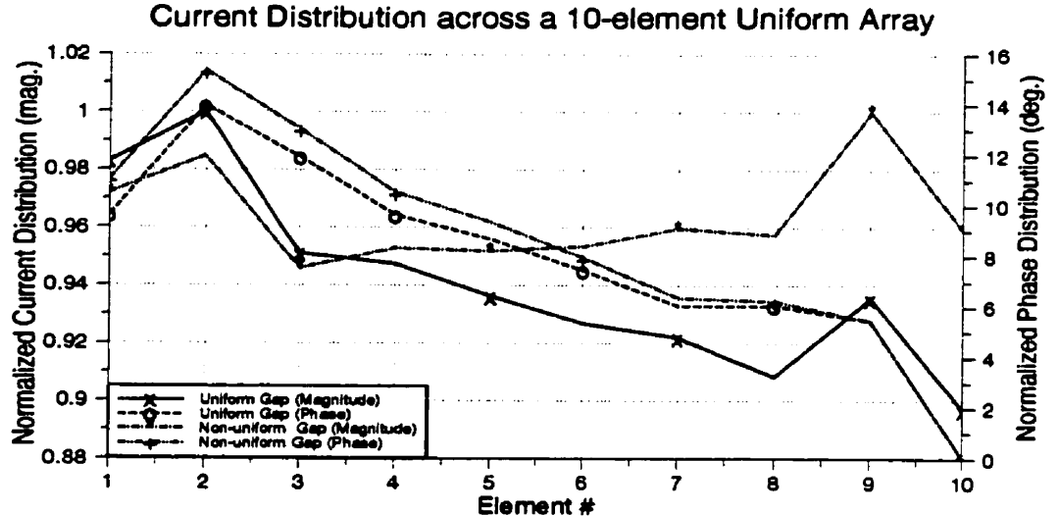

(b) Normalized Current Distribution (with Uniform and Non-uniform Gap) at 2.02 GHz
Uniform Gap: $d = 0.6$; Modified Non-uniform Gap: $d_{1,2} = 0.6$,
$d_3 = 0.58$, $d_4 = 0.56$, $d_5 = 0.54$, $d_6 = 0.52$, $d_7 = 0.5$, $d_8 = 0.48$, $d_{9,10} = 0.46$
$W = 3.6$, $L = 936.3$, $W_p = 37.5$, $L_p = 41.3$, $D_{offset} = 47.75 \approx \lambda_g/2$, $D = 93.5 \approx \lambda_g$
(All dimensions in mm)

Figure 3.3: Plots of Return Loss, Gain, and Current Distribution for a 10-element Resonant Uniform Standing-wave Array

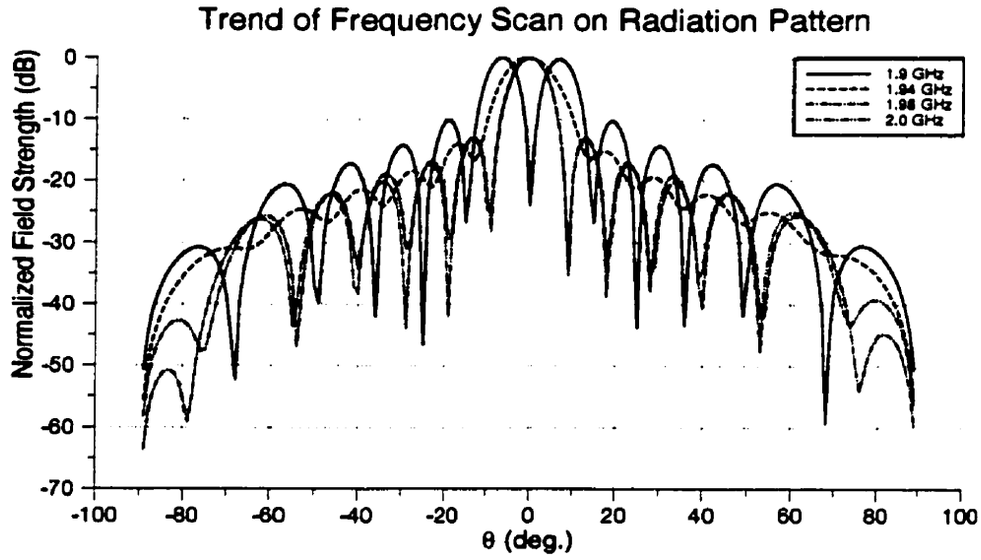

(a) Lower frequency scan

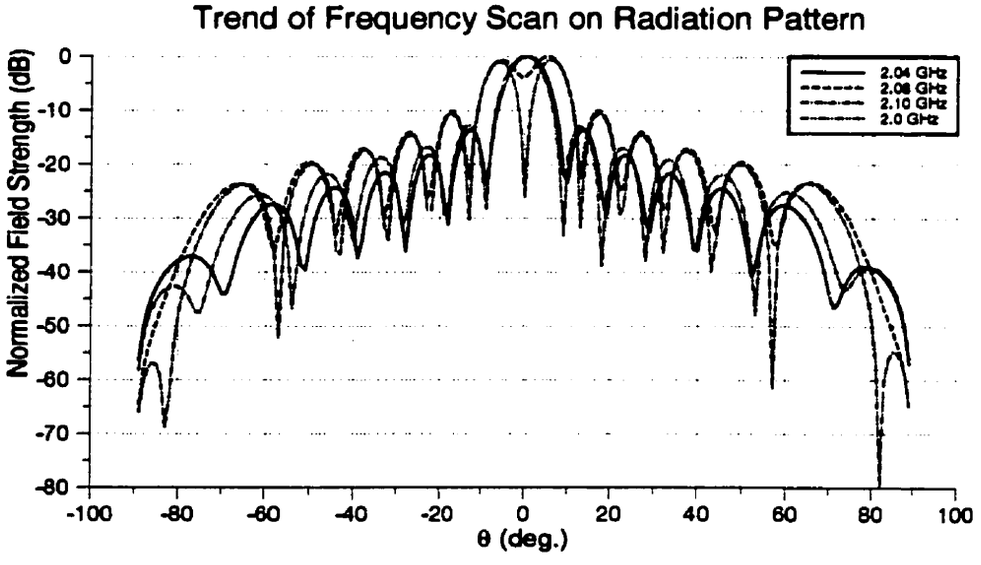

(b) Higher frequency scan

$W = 3.6$, $L = 936.3$, $W_p = 37.5$, $L_p = 41.3$, $d = 0.6$, $D_{offset} = 47.75 \approx \lambda_g/2$, $D = 93.5 \approx \lambda_g$

(All dimensions in mm)

Figure 3.4: Frequency Scan of a 10-element Uniform Standing-wave Array with Open-ended Feedline ($\phi = 0$)

to resonance of radiators at forward and reflected waves which exist on the line and become more out of phase further away from the operating frequency.

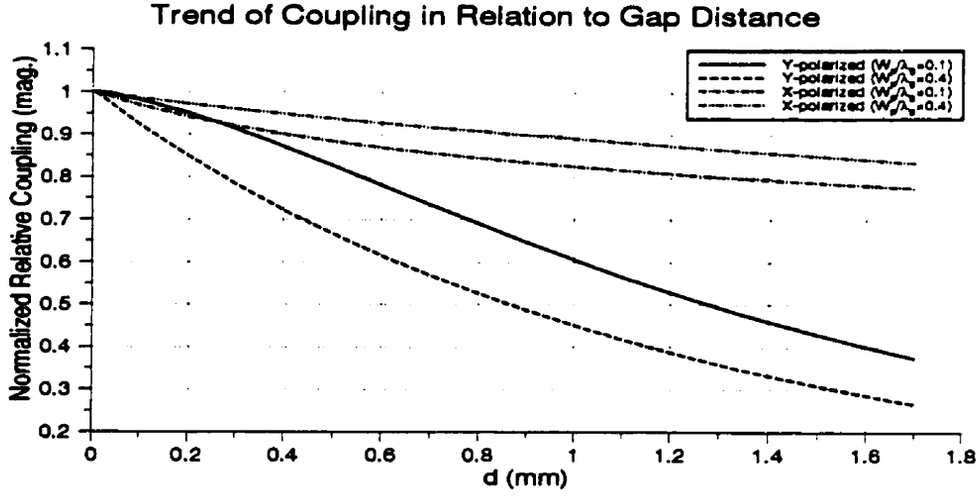

Figure 3.5: Design Curves for Various Patch Dimensions and Polarizations

An attempt to compensate for the non-uniform distribution is made and the procedure to balance the existing 6% drop in coupling is to introduce a non-uniform gap size along the array. By referring to the design curves (a combined design curve is given in Figure 3.5) a 5% increase in coupling corresponds to about 0.15 mm in gap size. When 0.15 mm is divided among 7 or 8 middle elements, an incremental gap reduction of 0.02 mm is obtained. The implemented simulation results in Figure 3.3.(b) displays an average 97% uniform coupling for the modified gap distribution in comparison with 93% for a uniform gap size.

3.3 Taylor Distribution

Changing the patch length or width alters the resonant characteristics of radiators; however, the amount of power coupled to each patch can be controlled using the gap distance. This feature provides us with the capability of assigning any desired distribution across the array. The method is simply relating the desired distribution to the

design curve obtained for the single patch case. The coupling-gap diagrams provide estimate of coupling percentage to a resonant patch at various patch separations. Data obtained for design curves should be at the resonant frequency of the patch in order to avoid any deviation from the actual efficiency of radiators.

One of the commonly employed distributions in arrays is Taylor distribution which was described briefly in Section 1.6.1. Figure 3.5 is provided for reference in understanding the method which relates the desired Taylor distribution to the gap distance across the array.

The first step is to determine the minimum gap required across the array. This should correspond to the maximum coupling of the center element(s) in Taylor distribution. Here the assumption that sufficient accuracy is achievable at the time of fabrication is considered. Based on the design curve, the minimum gap distance maps to some fraction of coupling. This fraction should be incorporated in calculation of percentage power coupled for other elements.

If no amplitude and phase decay along the feedline is assumed, the first gap distance which realizes the Taylor distribution can be determined and any compensation for attenuation factor and power level decrease typical of series-fed method can be accounted for next. For instance if we consider an array of 10 patch elements ($\frac{W_p}{\lambda_g} = 0.4$) with a minimum gap of 0.2 mm for two central patches, 85% coupling is read off the design curve. By locating the elements at λ_g intervals starting from $\lambda_g/2$, the two central patches should receive 98% of the power based on the Taylor distribution diagram. The fraction can be approximated to unity and simplify the computation.

Taking the minimum gap of 0.2 mm as the reference, the relative coupling of $0.9 \times 0.85 = 0.765$ is computed, which translates to a gap of approximately 0.3 mm for the adjacent element. Similar calculation determines the estimated gap distance for other elements. Table 3.1 includes the values obtained by the method explained above.

The results included in Table 3.1 are implemented in simulation on the geometry of Figure 3.1 and the outcome is, as expected, a lower side lobe level about the desired magnitude [Figure 3.7.(a)]. The gap distance for each element is denoted with subscripts corresponding to the element numbers. Figure 3.6.(a) confirms the

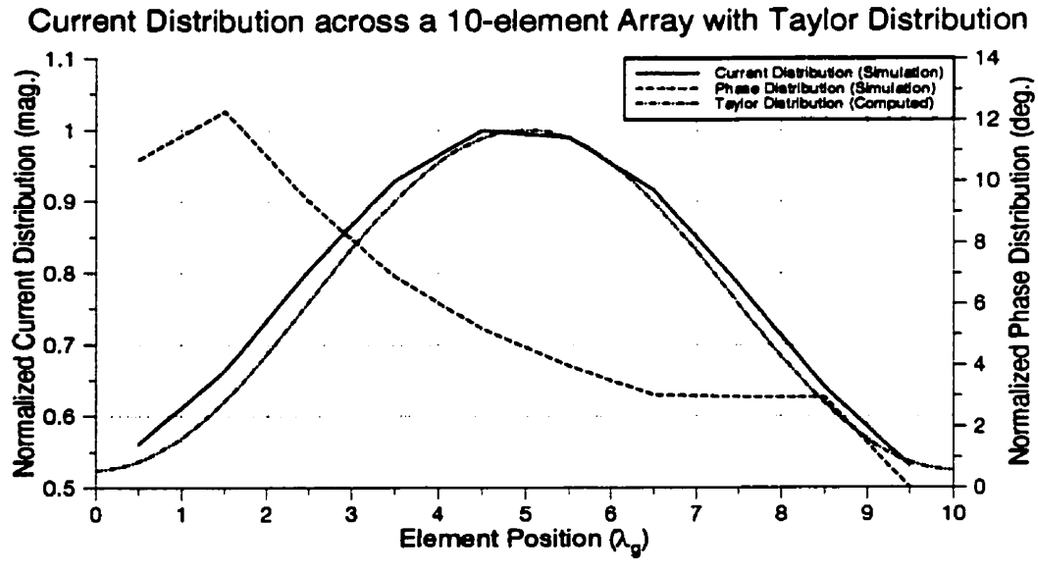

(a) Current Distribution across the Array at 2.03 GHz
(Theoretical Taylor Distribution for: N=10, SLL=-20 dB, $\bar{n}$=3)

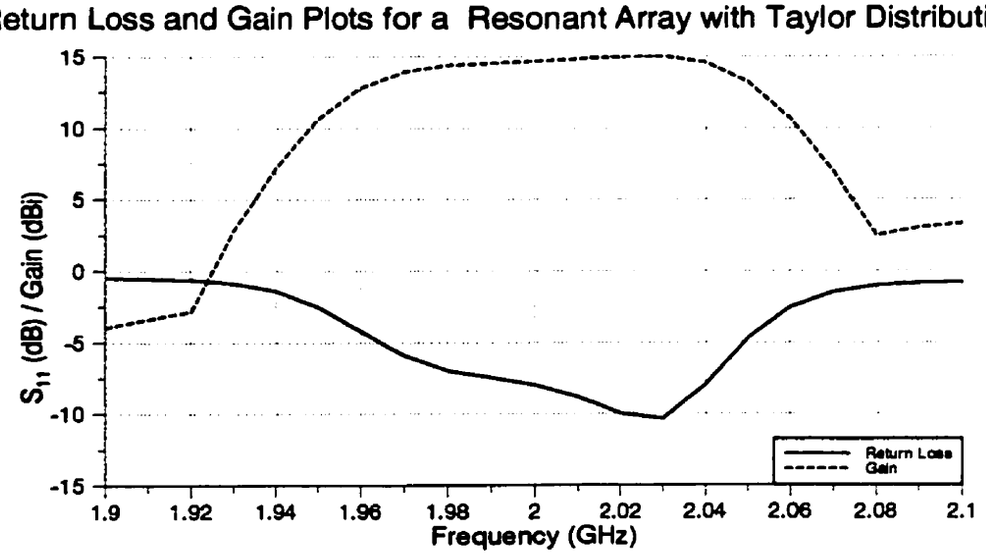

(b) Return Loss and Gain at 2.03 GHz
$W = 3.6$, $L = 936.3$, $W_p = 37.5$, $L_p = 41.3$, $D_{offset} = 47.75 \approx \lambda_g/2$, $D = 93.5 \approx \lambda_g$

Figure 3.6: Current Distribution, Return Loss and Directivity of a 10-element Standing-wave Array with Taylor Distribution

Table 3.1: Determination of Spacing, d, for a Taylor Distribution with 10 Elements. SLL=-20 dB and $\bar{n}$=3

Element #	Taylor Distribution	Normalized Coupling	Gap d (mm)
5	≈ 1.0	0.85	0.2
4	0.90	0.765	0.3
3	0.75	0.638	0.5
2	0.63	0.523	0.8
1	0.53	0.451	1.0

established distribution as compares it with the theoretical Taylor distribution. Once again, the simulated current distribution is obtained by reading the y-component of the resonant current at the center of each element and normalizing it to the maximum value of the set. This verifies the method to implement Taylor distribution using the design curves or any trend deduced from these curves. Thus the design curves are reliable bases to approach the design of a desired distribution. The phase distribution, although not so significant, can be improved by different inter-element spacing. Also an average coupling of 78% is read from the current distribution and the percentage power radiated of 90.8% is computed by

$$P_{rad} = 1 - |S_{11}|^2 = 1 - |0.30|^2 = 0.908.$$

The array is also simulated with a matched feedline to investigate the effect of traveling-wave on far-field patterns. This issue is addressed in the next section.

The cross-polarization in the array with the desired Taylor distribution is identical to the that with uniform distribution. The uniform and Taylor distributions exhibit maximum gains of 15.4 and 15.0 dBi which is expected as the result of uneven power distribution.

3.4 Traveling-wave Fed Array

Once the termination is matched with the impedance of the feedline, traveling-waves at any frequency can propagate along the transmission line. First intuition is to position the elements into an array in proximity of a matched feedline.

There are two ways to accommodate for a traveling-wave configuration. The first one is to terminate the feedline with a second source port. The other approach is to include a matched probe load at the termination.

In the probe load model, many parameters govern the overall impedance imposed on the circuit, mainly the probe diameter and substrate thickness. When the feedline is matched to a load with proper parameters, there would be sufficient confidence that the traveling-wave exists along the feedline. This can also be checked by running a simulation for the matched feedline and observing the return loss and input impedance.

The traveling-wave feeding mechanism removes the necessity of precise location of resonators while suffers from lower gain due to dissipation of the left over power at the termination.

For a matched feedline, the impedance mismatch becomes highest at the resonant frequency where the coupling to patches is maximum and patch impedances are imposed on the overall impedance of array. For off-resonant frequencies, the array input impedance corresponds to the transmission line impedance matched at termination. The matched feedline requires further matching of the entire array.

In addition to the matched feedline, the matching of the entire array to an appropriate load at the resonant frequency can be considered at the termination. This technique needs measurement of impedance seen at the feedline end with reference to 50Ω. However, such a matching demands various load terminations which practically is not achievable. To investigate the difference of each technique, a comparison is made using a uniform array.

A uniform array with the given specification in Figure 3.8 and geometry of Figure 3.1 is matched using the following two approaches. For the first case the feedline is matched to a 50Ω load and the entire array is matched at the input using a tuning stub. The impedance seen at the input for the array including the 50Ω is $11.2 - j3.9\ \Omega$. A tuning stub with width $W_{stub} = 3.6$ mm (the same as feedline) and length $L_{stub} = 31.6$ mm is placed at 3.5 mm away from the source in the geometry of Figure 3.1 (but not shown there). The matching provides a return loss of -20 dB and gain of 14.4 dBi at the resonant frequency.

The other approach requires a load of $11.5-j8.7\ \Omega$ at the feedline end including the elements and yields an impedance of $10.3+j0.6\ \Omega$ at the input. Since the impedance is mostly real, a quarter-wave transformer matching at the source would provide the matched input. The transformer takes the values $W_{quarter-wave} = 10.8$ mm in width and $L_{quarter-wave} = 22.5$ mm in length which is inserted between the source line and feedline of Figure 3.1 (also not shown there). As seen in Figure 3.8, there is a shift in resonance and the gain at this minimum is about 12.1 dBi. The maximum gain still occurs at 2 GHz with the value of 13.9 dBi, which is not so different from the previous approach.

Radiation from the tuning stub could be a reason for the increase in gain and use of tuning stub is recommended in y-polarized configurations. The latter matching method appears to be suitable for x-polarized radiators; however, using a non-standard load is not practical in any ways.

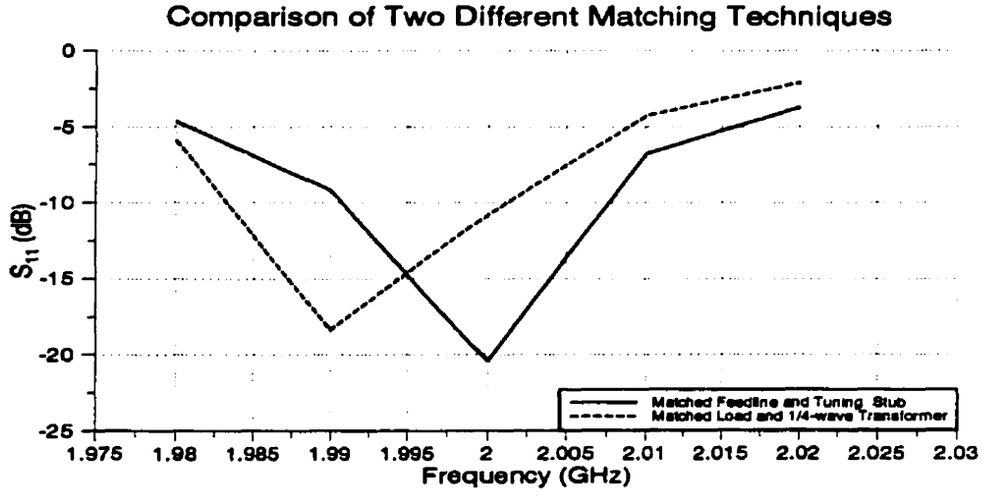

Dimensions (mm): $W = 3.6$, $L = 936.3$, $W_p = 37.5$, $L_p = 41.3$, $d = 0.2$, $D = 94.0$; $\epsilon_r = 3.2$

Figure 3.8: Return Loss of Two Matching Methods for Traveling-wave Feeding Purpose

3.4.1 Traveling-wave Characteristics

In practical lines, the traveling-wave attenuates due to the material properties. The major sources of attenuation are dielectric and conductor losses. Dielectric loss denoted by α_d is the imaginary portion of the complex dielectric constant and the dominant cause of attenuation. The type and quality of dielectric material determines this parameter which in turn relates inversely to the cost of material production. Conductor (copper) loss, α_c, is the secondary source of attenuation and an inevitable factor unless superconductive materials are employed instead. The sum of two attenuations comprises the overall attenuation of the printed microstrip structure. The general equation for the case of traveling-wave along a transmission line is employed (the expression for the traveling voltage is $V(x) = V_s\, e^{-\alpha x}\, e^{-j\beta x}$) in order to obtain results for mathematical model.

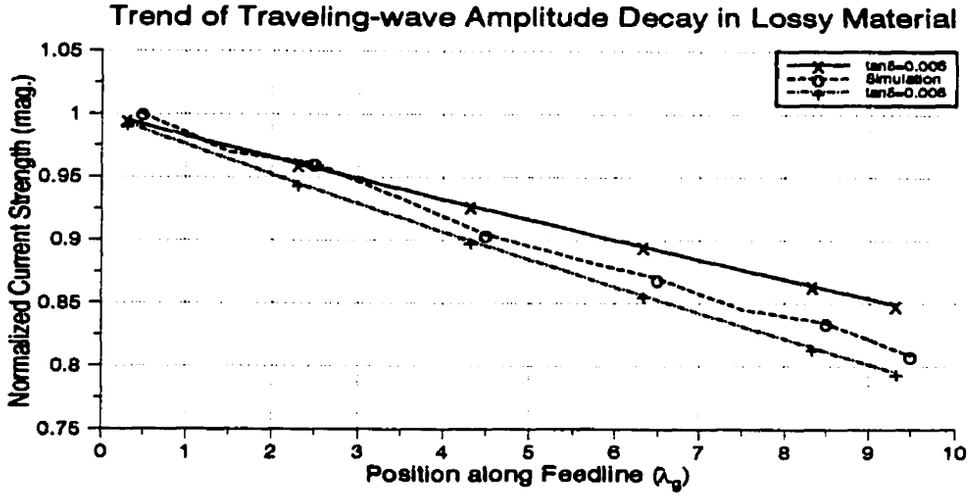

Dimensions (mm): $h = 1.524$, $W = 3.6$, $L = 936.3 \approx 10\lambda_g$, $W_p = 37.5$, $L_p = 41.3$, $d = 0.1$, $D = 93.5$; $\epsilon_r = 3.2$ (Figure 2.4 with 50Ω termination)

Figure 3.9: Traveling-wave Amplitude Decay as a Function of Position on a Feedline

The parallel plate distributed elements are used to calculate the propagation constant, γ. The next step is to determine γ by calculating the four distributed circuit components of transmission line, i.e. resistance, capacitance, inductance and conduc-

tance. The conductivity of $\sigma = 1.0 \times 10^{-13}$ S/m for dielectric material is used in calculation as well as the conductivity of $\sigma_c = 5.8 \times 10^7$ S/m for copper.

For the MC5 dielectric material ($\epsilon_r = 3.2,\ h = 1.524$ mm), $\gamma = 0.188 - j74.93$ is obtained for $\tan\delta \approx 0.006$ at 2.0 GHz and $\gamma = 0.263 - j74.93$ is computed for $\tan\delta \approx 0.008$ at 10.0 GHz on the basis of parallel plate configuration.

In order to investigate the amount of power dissipation along the feedline, the resonant current component of a single radiating patch at λ_g intervals along the line is measured (Figure 2.4). Feedline of $10\lambda_g$ was considered and guided wavelength of $\lambda_g = 93.9 \approx 94$ mm was used as the discrete reading points. The current values are then normalized to the maximum value and squared to obtain the relative power. When the computed values from simulation are plotted in contrast to the mathematical model using the parallel plate approach yet at the same positions, the simulation results appear to follow the trend based on the general parallel plate transmission line formulation. Figure 3.9 clearly illustrates the phenomenon.

This discussion brings us to the conclusion that proper gap adjustment should be taken into consideration in order to compensate for the amplitude decay of traveling-wave. The consideration become necessary as the length of array and/or the material losses increase.

3.4.2 Uniform Distribution

The same uniform distribution used in standing-wave configuration (Figure 3.1) is applied to the traveling-wave and as expected similar pattern is observed with the exception of slightly lower gain. In order to simultate a traveling-wave, the feedline is terminated with 50Ω probe load. This configuration may introduce some error since the probe load value is directly related to the probe diameter and the substrate thickness, which may not exactly match with the feedline impedance. This method is considered reliable since replacing the probe load with another source introduces error in gain calculation as well as phase distribution along the feedline. However, traveling-waves propagate on the feedline when the 50Ω feedline is terminated with a 50Ω load. Figure 3.10 includes the loss and current distribution measured at the center of each element in a 10-element array. The dominant y-polarized current

component decreases rapidly toward the termination. Due to the probe load, the end element exhibits relatively larger coupling which is the result of a discontinuity at the termination. The power calculation reveals that

$$P_{rad} = 1 - |S_{11}|^2 = 1 - |0.47|^2 = 1 - 0.22 = 0.78.$$

only 78% of the power is radiated. In order to compensate for the non-uniform distribution across the array, the position of the elements are adjusted to account for the 20% reduction in coupling across the array (see Figure 3.5). The drop in coupling corresponds to about 0.4 mm in gap size between the eight middle elements.

If the gap difference of 0.4 mm is distributed among the eight elements, a progressive gap increase of 0.05 mm should establish almost a uniform distribution. The result of modified gap size which represents a progressive increase of 0.05 mm in gap distance is included in Figure 3.10.(b).

The traveling-wave excitation also has the advantage of displacing the main beam rather than deforming the overall pattern at frequencies within bandwidth. As shown in Figure 3.11, the integrity of the far-field pattern has been preserved despite the frequency scan and only beam tilt occurs.

Although the traveling-wave feeding removes the requirement for positioning the elements at particular points, the significant non-uniform distribution of power requires the non-uniform gap size across the array. Despite the option of non-uniform gap size, the traveling-wave feeding scheme continues to suffer from very low efficiency which makes other merits of this method unattractive.

In practice, it is easy to convert the resonant structure into traveling-wave feeding with matched termination of feedline, if the low efficiency and less uniform distribution can be overlooked. The conversion may slightly alter the resonant frequency due to change in overall input impedance but has little effect on the far-field pattern.

The gain reduction shown in Figure 3.12 is due to the increased cross-polarization in the array plane. The increase in cross-polarization is the result of weaker resonant current amplitude. While the co-polar fields remain the same, increase in cross-polar component lowers the overall efficiency. Uneven side lobe levels at each side of the main beam is indicative of relatively uniform distribution for left elements in contrast

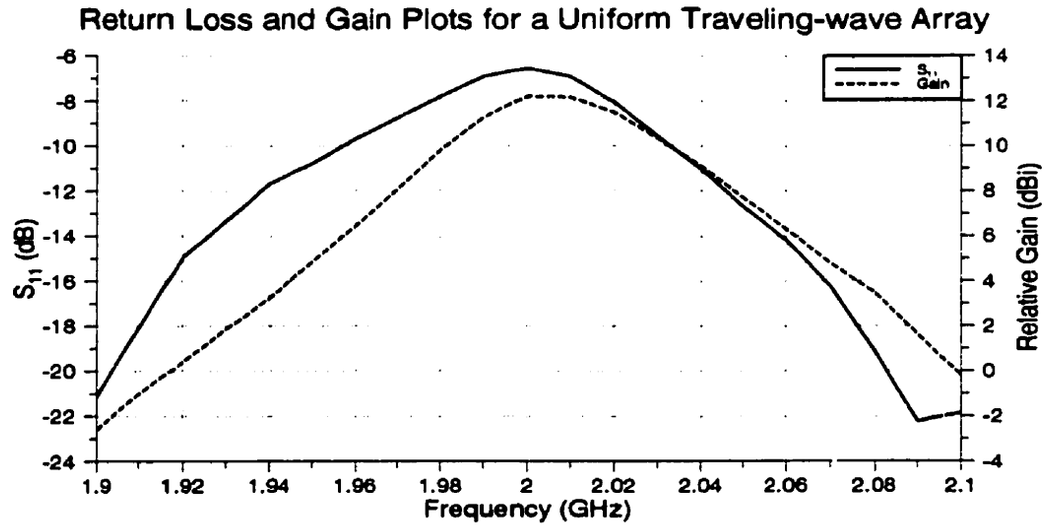

(a) Losses and Gain Plots at 2.0 GHz

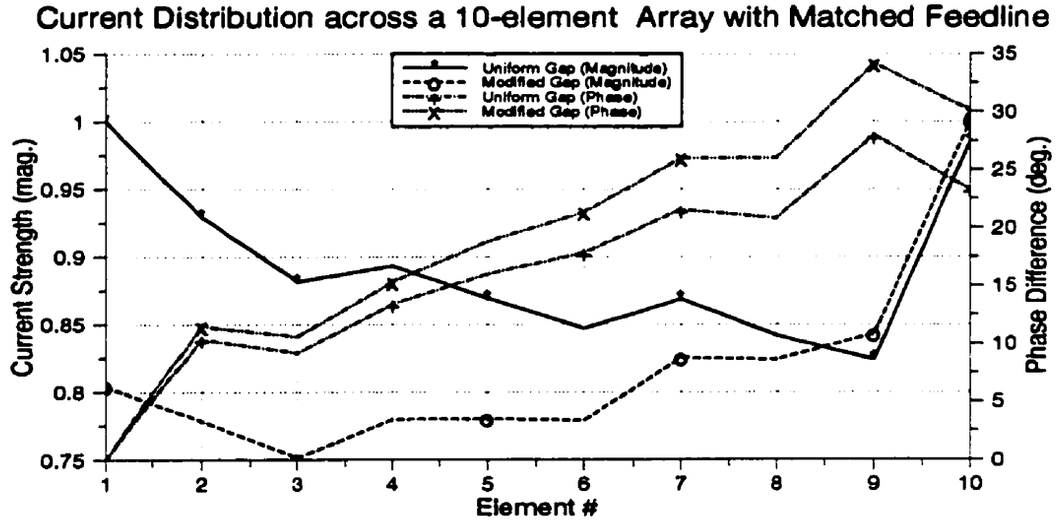

(b) Normalized Current Distribution (with Uniform and Non-uniform Gap) at 2.0 GHz
Uniform Gap: $d = 0.6$; Modified Non-uniform Gap: $d_1 = 0.6$,
$d_2 = 0.55$, $d_3 = 0.5$, $d_4 = 0.45$, $d_5 = 0.4$, $d_6 = 0.35$, $d_7 = 0.3$, $d_8 = 0.3$, $d_{9,10} = 0.2$
Dimensions (mm): $W = 3.6$, $L = 936.3$, $W_p = 37.5$, $L_p = 41.3$, $D = 93.5 \approx \lambda_g$

Figure 3.10: Current Distribution, Losses and Gain of a 10-element Array with Matched Feedline

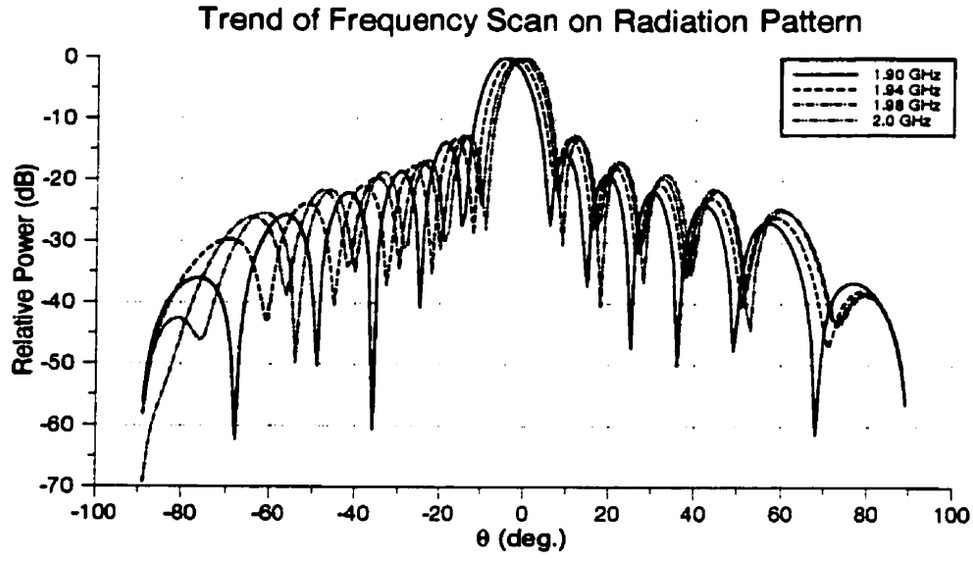

(a) Lower frequency scan

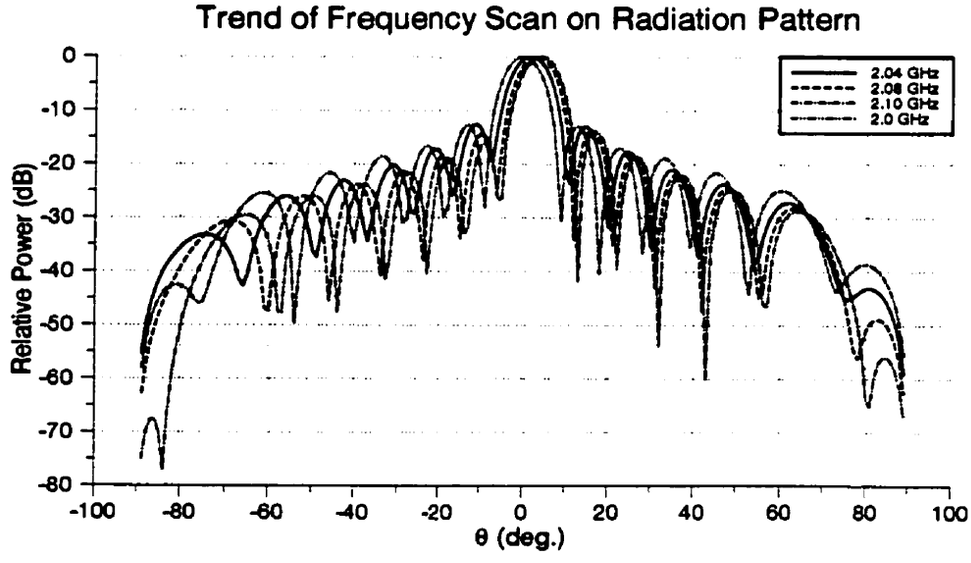

(b) Higher frequency scan

Dimensions (mm): $W = 3.6$, $L = 936.3$, $W_p = 37.5$, $L_p = 41.3$, $d = 0.6$, $D = 93.5 \approx \lambda_g$

Figure 3.11: Frequency Scan of Uniform Array of 10 Elements with Matched Feedline in $\phi = 0$ plane

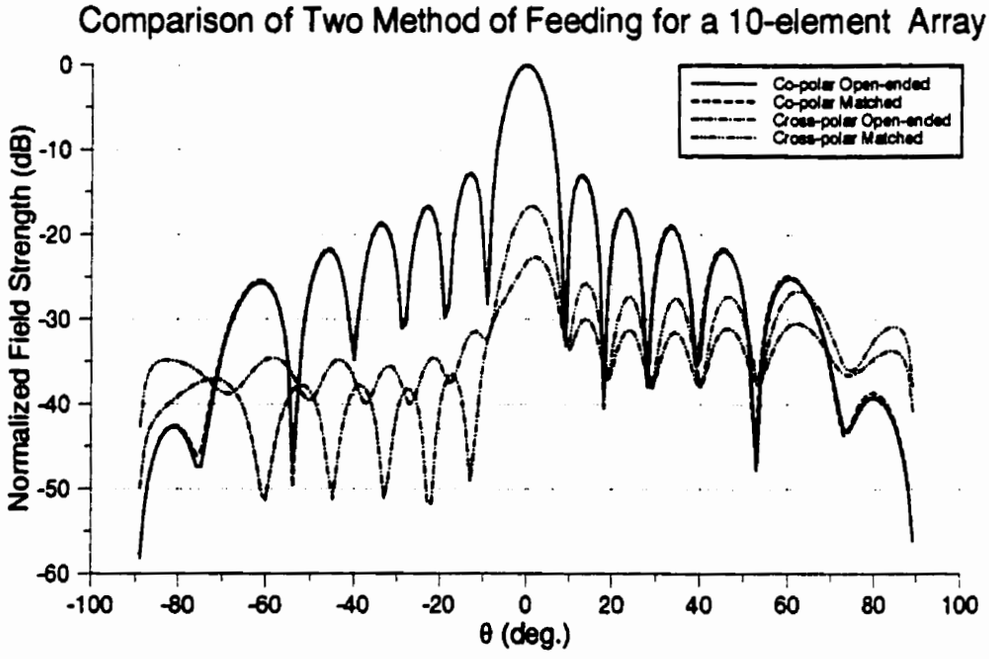

Dimensions (mm): $W = 3.6$, $L = 936.3$, $W_p = 37.5$, $L_p = 41.3$, $d = 0.6$, $D = 93.5 \approx \lambda_g$

Figure 3.12: Traveling-wave versus Standing-wave Feeding Method ($\phi = 0$)

to semi-uniform distribution for right elements in respect to the center element.

Taylor Distribution

Like uniform distribution, a Taylor distribution across an array with traveling-wave excitation exhibits demerits of increased cross-polarization and reduced directivity in exchange of some design flexibility. The results in Figure 3.7 confirms once again the features associated with the traveling-wave feeding.

3.5 Uniform Cross-linear Array

As mentioned in previous chapters, the patch length determines the resonance of radiator and the patch width has a smaller effect on the resonant frequency. Determination of patch length is normally computed through an arbitrary width; thus there

is a resonant length corresponding to the assumed width. In this configuration, width may not be larger than the half guided wavelength, otherwise the cross-polarization will be high. This study also indicates that for large patch size ($0.5 \leq \frac{W_p}{L_p} \leq 0.95$ where $W_p, L_p \leq \lambda_g/2$) the cross-polarization is significant. Narrow patches ($0.1 \leq \frac{W_p}{L_p} \leq 0.5$) resolve the problem at the expense of lower coupling.

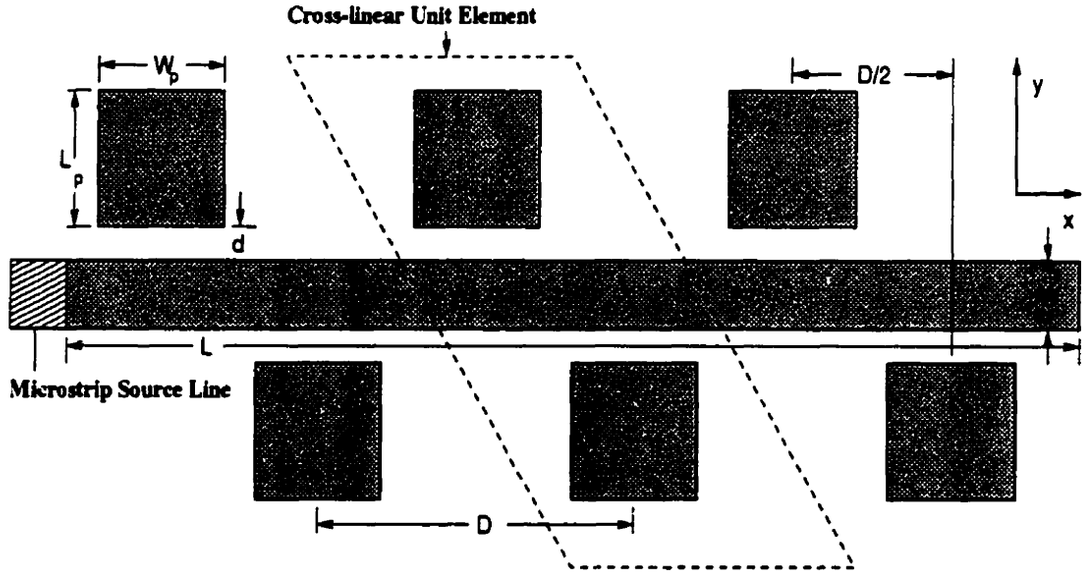

Figure 3.13: Cross-linear Array Configuration

Another solution to reduce the cross-polarization in the xz-plane is to position identical patches at half guided wavelength away from the original array across the feedline as shown in Figure 3.13. Therefore, the linear array consists of resonators on one side of the feedline (Figure 3.1) while the cross-linear comprise of patches located on both sides of the feedline at $\lambda_g/2$ intervals (Figure 3.13). For identical number of resonators, this technique reduces the array length which also results in reduced directivity. Figure 3.14 compares the cross-polarization level of linear and cross-positioned array of 10-elements with matched feedline.

The cross-polar component diminishes significantly at the boresight, in the xz-plane, and overall cross-polar strength becomes nearly constant at all angles. Pattern of Figure 3.14 also points out the change in the number of side lobes. This feature corresponds to the number of elements in the array. From the pattern we observe

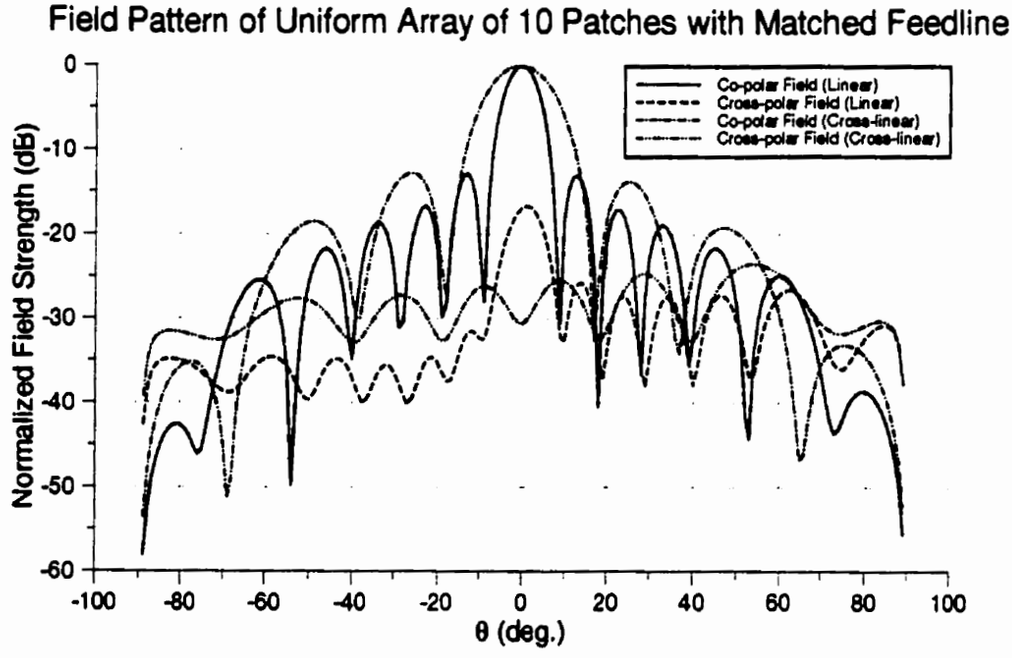

All dimensions in mm: $W = 3.6$, $W_p = 37.5$, $L_p = 41.3$, $d = 0.6$
Linear: $L = 936.3$, $D = 93.5 \approx \lambda_g$ Number of Patches=10
Cross-linear: $L = 467.8$ $D/2 = 46.7 \approx \lambda_g/2$ Number of Patches=10

Figure 3.14: Radiation Patterns of Linear and Cross-linear Arrays with Equal Number of Patches ($\phi = 0$)

that each pair of cross-positioned patches comprises one radiating element; therefore, although there is equal number of patches in both configurations, the array of 10 elements would reduce to 5 radiators in each guided wavelength when configured as cross-linear. In order to make a better comparison, an array of the same length and the same number of radiators but with cross-linear configuration is considered. Figure 3.15 signifies the differences between the two arrays and Table 3.2 summarizes the important parameters. Due to the use of 50Ω rather than the second port, the transmission loss at the termination is not measured.

When each pair of patches within a guided wavelength is considered as one element (as shown in dashed area in Figure 3.13), twice as many of patches is needed to

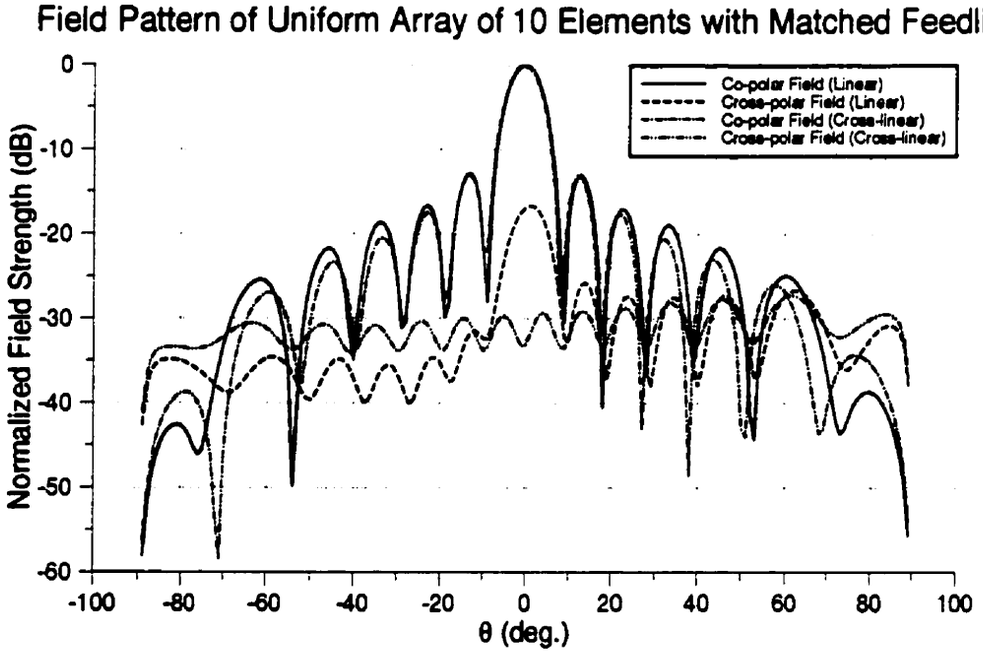

Dimensions (mm): $W = 3.6$, $W_p = 37.5$, $L_p = 41.3$, $d = 0.6$ @ $2.0\,GHz$
Linear with 10 Patches: $L = 936.3$, $D = 93.5 \approx \lambda_g$
Cross-linear with 20 Patches: $L = 936.3$, $D = 93.5 \approx \lambda_g$, $D/2 = 46.7 \approx \lambda_g/2$

Figure 3.15: Linear versus Cross-linear Arrays with Equal Number of Elements in $\phi = 0$ Plane

construct an array of 10 elements. The spacing between each cross-positioned patch is $\lambda_g/2$ in order to keep the patches at anti-phase positions. Anti-phase positions create co-phase resonant current on patches and cancel out the cross-polar components.

3.6 Effect of Non-uniform Element Width

As mentioned earlier one technique to improve the performance bandwidth is to implement a linear increase in patch width. This method disturbs the far-field pattern to some extent but greatly widens the resonant bandwidth. Certainly width perturbation should not be drastic but gradual. To study the effect of incremental width change along the array, three cases are considered first. Since the elements are dis-

Table 3.2: Linear and Cross-linear Array

Features at 2.0 GHz	**Linear** (10 elements)	**Cross-linear** (5 elements)	**Cross-linear** (10 elements)
Gain (dBi)	12.4	11.1	14.4
# of Side Lobes	12	6	12
Maximum Cross-polar Level (dB) ($\phi = 0$)	-16.8 @ 0°	-23.5 @ 54°	-27.2 @ 61°
Beamwidth (deg.)	13.0	25.0	13.0

Dimensions (mm): $W = 3.6$, $W_p = 37.5$, $L_p = 41.3$, $d = 0.6$ at 2.0 GHz
Cross-linear: (10 Patches) $L = 467.8$; (20 Patches) $L = 936.3$, $D = 93.5 \approx \lambda_g$, $D/2 = 46.7 \approx \lambda_g/2$
Linear with 10 Patches: $L = 936.3$, $D = 93.5 \approx \lambda_g$

crete, the linear increase takes discrete values.

Figure 3.16 gives an example of linearly progressive width increase. It also includes the progressive increase in length discussed in the next section.

The uniform array of Figure 3.1 in conjunction with the progression method shown in Figure 3.16 can be referred to as the geometry of this and the following sections. For the linear progressive increase in width, elements beyond the first patch near the source receive incremental increase in width which is based on some percentage of width. The mathematical terms for the linear progressive width increase takes the form

$$W_{p,n} = W_p + n\Delta W_p$$

where n is the integer multiplier which corresponds to number of percentage increase in width as progresses and ΔW_p is the incremental width added to the original patch width. This method is similar to constant increase of elements width with respect to the previous width size but reduces the problem of determining patch width for each step. Figure 3.17.(a) demonstrates the wider bandwidth due to different percentage increases in width. No significant improvement is observed for less than 1.0% width increase. 2.0% percent increase broadens the bandwidth to 2.0%, which is used in different patterns in order to investigate the best possible progression across the array.

Figure 3.17.(b) presents the various progression patterns in contrast with the linear

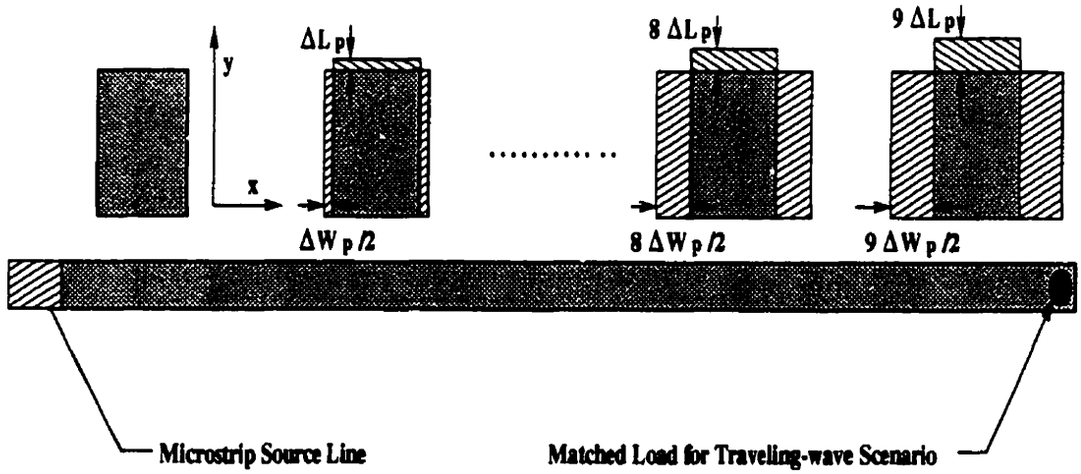

$W = 3.6$, $L = 936.3$, $L_p = 41.3$, $d = 0.6$, $D = 39.9$ (all in mm)
Width Change: 10-element open-ended array with first element width of $W_p = 37.5$ mm
Length Change: 10-element open-ended array with first element length of $L_p = 41.3$ mm

Figure 3.16: Geometry of Linearly Progressive Width or Length Increase

increase. In the V-type progression the center element(s) retains the natural resonant dimensions while the elements toward the array ends receive progressive increase in width. The A-type is similar to the V-type but a progressive decrease in width is established across the array. In the S-type progressive decrease is applied to elements on the left of center patch(es) while linear increase is set along elements on the right side of array.

None of the suggested patterns improve the bandwidth favorably and only linear 2.0% progression seems to provide a symmetric and enhanced bandwidth. The side effect of enhanced bandwidth is distortion and increase of the cross-polar field which result in degradation of overall pattern and reduced efficiency (Figure 3.18).

3.7 Effect of Non-uniform Element Length

The same approach is applied to the resonant lengths of the array. Since the resonance of each patch is mainly governed by its resonant length, the percentage change in length should be very minimal. If the effective progression for patch width is 2.0% , then the progression of length should be of the order 0.2% or less.

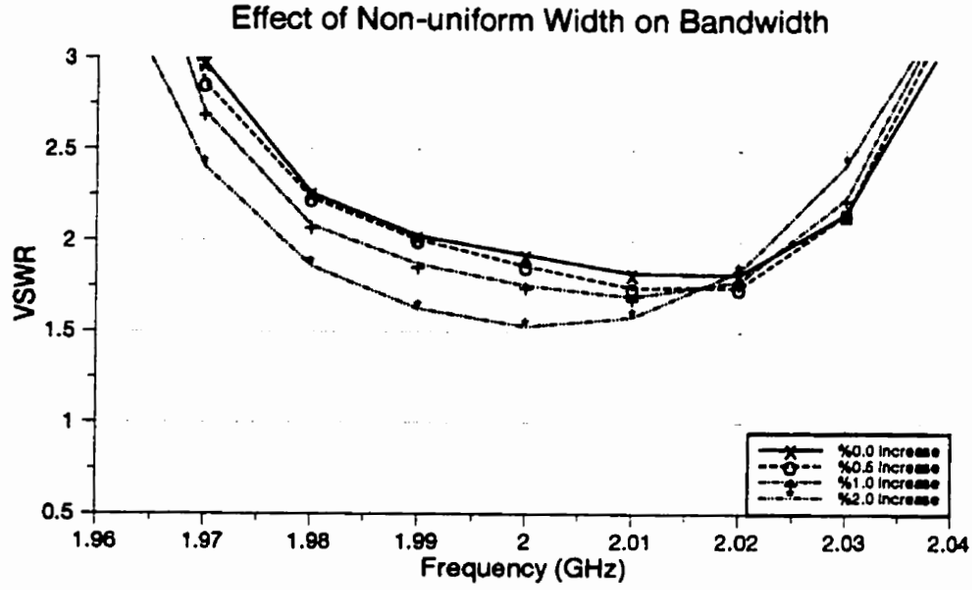

(a) Linear Width Progression for: $\Delta W_p = 0.005W_p$, $0.01W_p$, and $0.02W_p$

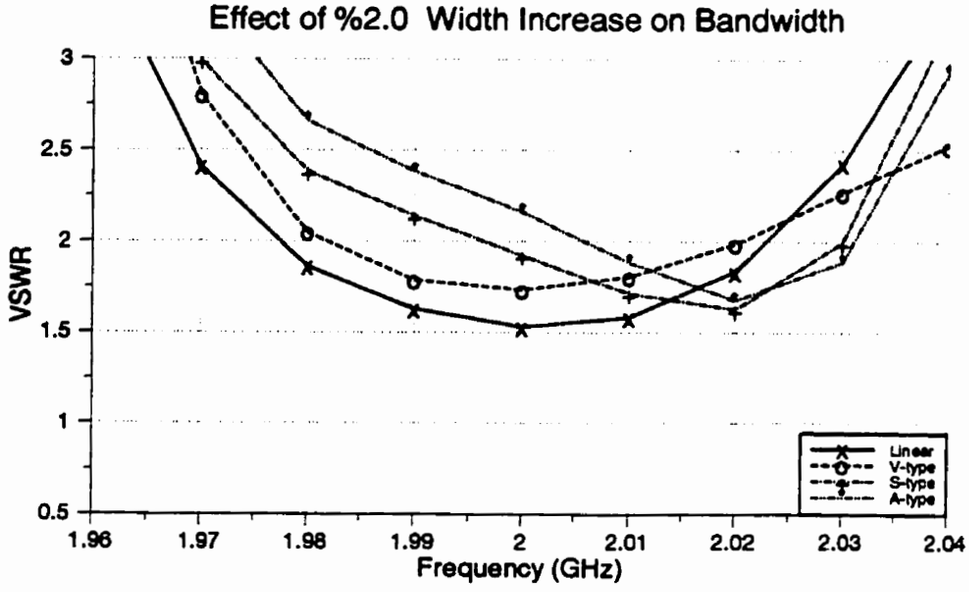

(b) Various Width Progression

Dimension (mm): $W = 3.6$, $L = 936.3$, $L_p = 41.3$, $d = 0.6$, $D = 39.9$; $\epsilon_r = 3.2$

Figure 3.17: Effect of Width Change across Array on VSWR

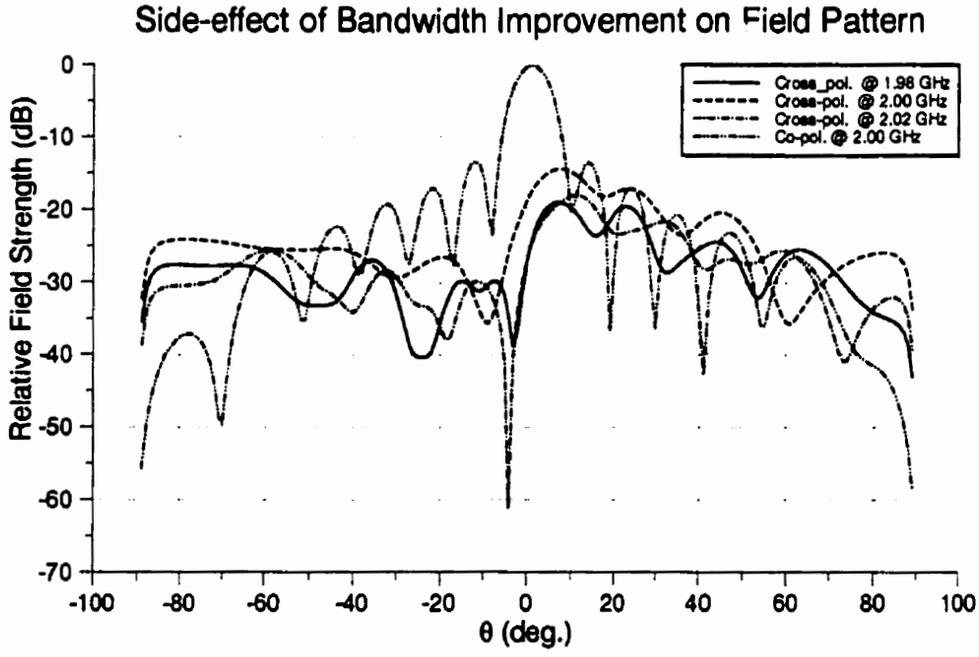

$W = 3.6$, $L = 936.3$, $L_p = 41.3$, $d = 0.6$, $D = 39.9$ (all in mm)
10-element array with open termination and first element width of $W_p = 37.5$ mm

Figure 3.18: Pattern Distortion due to Linearly Progressive Width Increase

Two cases of length progression are considered for the purpose of investigating the effect of non-uniform patch length change and the outcome demonstrates the effectiveness of the technique. The bandwidth enhancement is measured by how wide the resonance frequency band is placed for return losses of less than -10 dB. The first trend follows a V-type progression meaning the center elements maintain the designed resonant length and elements on both sides undergo 0.1% progressive increase in length. The S-type configuration is obtained by 0.1% positive progression on one side of the array while a negative progression is established on the other portion of the array with respect to the center element(s).

In a 10-element uniform array, two middle patches remain at the design resonant length at 2.0 GHz and other patches receive a progressive change in length.

As shown in Figure 3.19, the V-type progression brings about a frequency shift

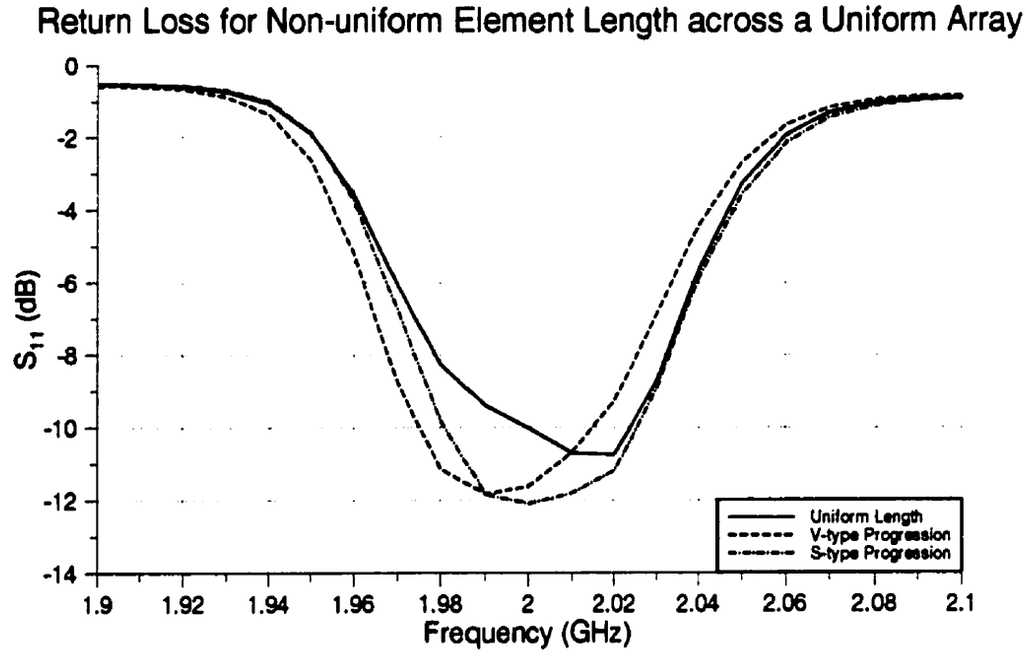

Dimensions (mm): $W = 3.6$, $L = 936.3$, $W_p = 37.5$, $d = 0.6$, $D = 39.9$
10-element array with open termination and center elements length of $L_p = 41.3\ mm$

Figure 3.19: Bandwidth Improvement by Progressive Length Change across an Array

which approximately coincides with the average of resonant lengths of all elements. However, the bandwidth improves from 1.2% to 2.0%.

The S-type progression provides a symmetric bandwidth about the design frequency and enhances the bandwidth to 2.2%. The progression was positive for the elements near the source and negative for elements towards the array end. This caused a slight shift in overall resonance which compensated for the deviation from the design frequency of the uniform array. If the progression reverses, the resonance shifts further away from the design frequency.

The effect on pattern due to such modification varies for each progression. The V-type progression exhibits some increase in side lobe levels and smoother nulls (Figure 3.20). In contrary, the S-type cause unsymmetric side lobes with respect to the main lobe in addition of smoother nulls which are indicative of differences in patch

resonance.

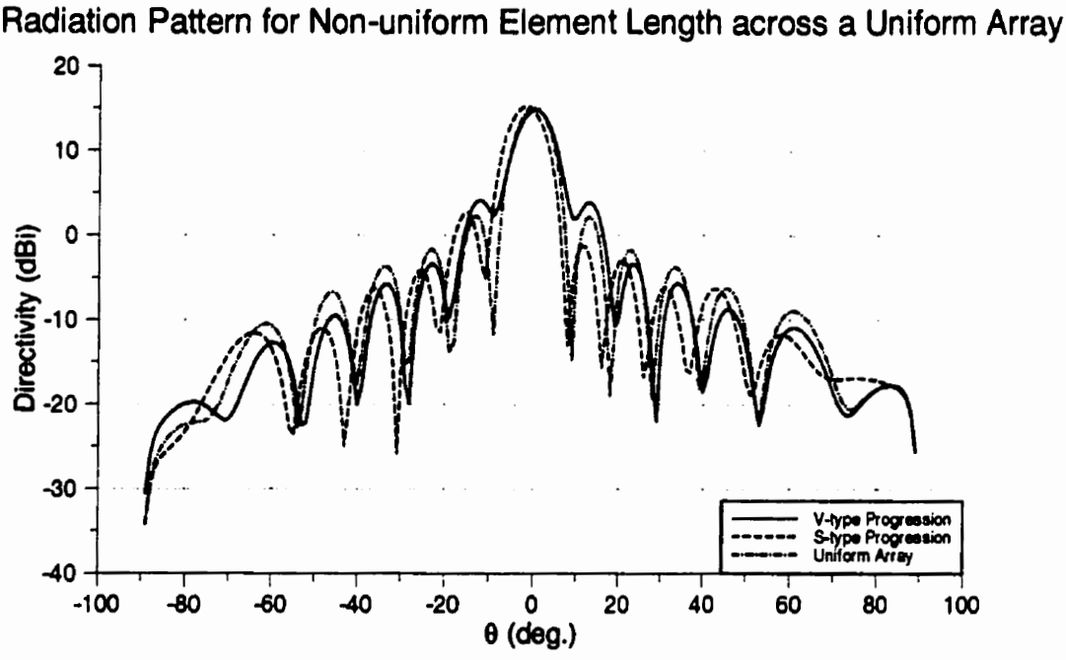

Dimensions (mm): $W = 3.6$, $L = 936.3$, $W_p = 37.5$, $d = 0.6$, $D = 39.9$
10-element array with open termination and center elements length of $L_p = 41.3$ mm ($\phi = 0$)

Figure 3.20: Effect of Progressive Length Change across a Uniform Array at 2 GHz

The cross-polarization increases at higher frequencies for both types but comparable or less at center and lower frequencies in comparison to the uniform case. The V-type has slightly lower cross-polar components at lower frequencies and marginally higher level at upper frequency bandwidth in contrast to the S-type.

Applying progressive length increment across the array appears as an efficient method to broaden the bandwidth while keeping the cross-polarization in a reasonable level. In practice, non-uniform length may exist due to imperfection in fabrication and is an inevitable factor. As seen in this section, minor inaccuracy in length sizes determines the performance of the array where such inexactness in width does not affect the characteristic significantly.

3.8 Dual Polarization Capability

As discussed earlier, either y- or x-polarization with respect to feedline current can be achieved, if proper orientation of radiating edges is maintained. When width (radiating edge) is parallel to the feeding strip, y-polarization is obtained and in case of patch width normal to the feedline x-polarization is achieved. In standing-wave feeding, the maximum coupling for y-polarized radiators occurs at voltage standing-wave maxima where x-polarization is achieved best when resonators are placed at current standing-wave maxima. The standing-wave pattern and existence of 90° phase shift between voltage and current standing-waves for both open- and short-circuited termination are shown in Figure 2.2. This characteristic provides the capability of dual band and dual polarization or three other possible combinations with a single antenna configuration.

3.9 Dual Configuration

The configuration under study enables us to have dual band and/or dual polarization array arrangements. This feature is investigated by an attempt to design and simulate a dual polarized array operating in two bands of 2.0 and 5.0 GHz (Figure 3.21) which correspond to the s- and c-bands in frequency spectrum. The design procedure for various resenators at 2.0 GHz band has previously been presented and here only the 5.0 GHz band design is briefly explained.

In order to reduce the simulation time, an array of $5\lambda_g$ at 2.0 GHz is preferred. This requires 5 elements in the s-band and about 12 elements in the c-band. Shorter array also removes any concern over amplitude and phase dispersion in the material.

The approach is to base the design on the c-band since any adjustments in c-band has little effect on the s-band design. An x-polarized array of resonators at 5 GHz band and an y-polarized arrangement of radiators at 2 GHz band are decided.

The resonator design begins with estimates using the conventional formulation. Resonant length for a patch of 10.0 mm width is computed to be 16.5 mm. When patch is placed in proximity of 50Ω feedline, the resonant length at 5.0 GHz is about

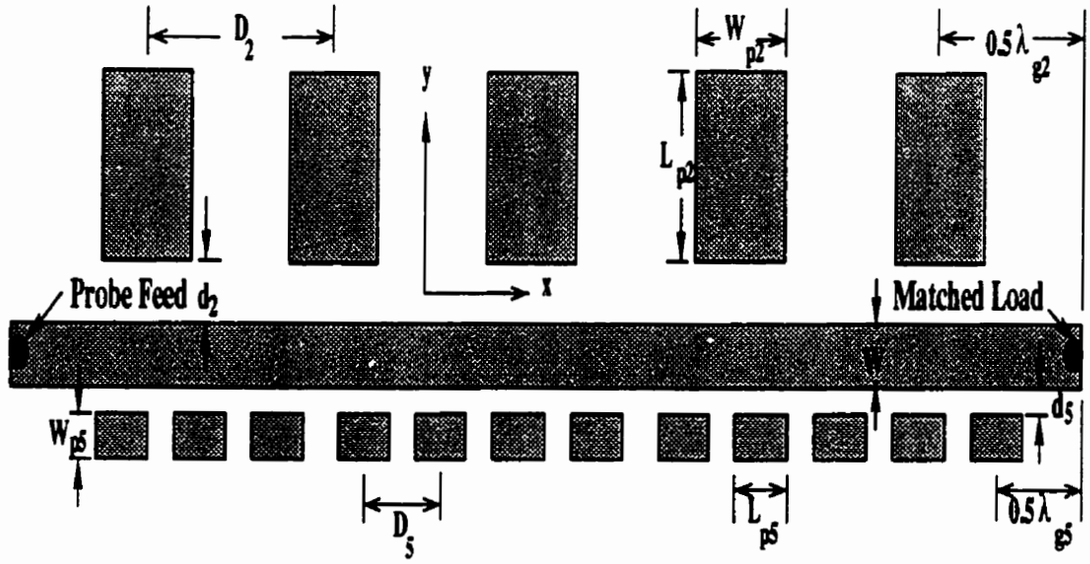

S-Band: $W_{p2} = 25.0$, $L_{p2} = 41.8$, $d_2 = 0.3$, $D_2 = 94.0 \approx \lambda_{g2}$
C-Band: $W_{p5} = 10.0$, $L_{p5} = 16.6$, $d_5 = 1.0$, $D_5 = 37.6 \approx \lambda_{g5}$
All dimensions in mm: $Z_o = 50\,\Omega$, $W = 3.6$, $L = 463.0$, $h = 1.524$, $\epsilon_r = 3.2$

Figure 3.21: Geometry of Dual Band Array Configuration

16.6 mm. A quick comparison between 5-GHz resonator and 2-GHz ones casts light on how drastic the difference is (Figure 3.22). A comparison of identical patch widths appears inadequate while width to wavelength ratio seems a more reasonable contrasting measure. The coupling greatly increases at higher frequencies (as seen in Figure 3.22) for the same range of gap distance. Simple direct frequency scaling is used to determine gap limits of c-band corresponding to the range in the s-band.

It appears that a set of design curves at one resonance frequency does not apply directly to designs at any other frequency.

3.9.1 Simulation Results

In order to avoid difficulty of finding the proper feedline length corresponding to the open-circuited line at 2.0 GHz band and short-circuited at 5.0 GHz band, traveling-wave feeding method is chosen. In case of dual band array, the simplest way is to provide a matched load to the feedline prior to placement of elements and apply matching at both bands at the source end after including the elements. For this case

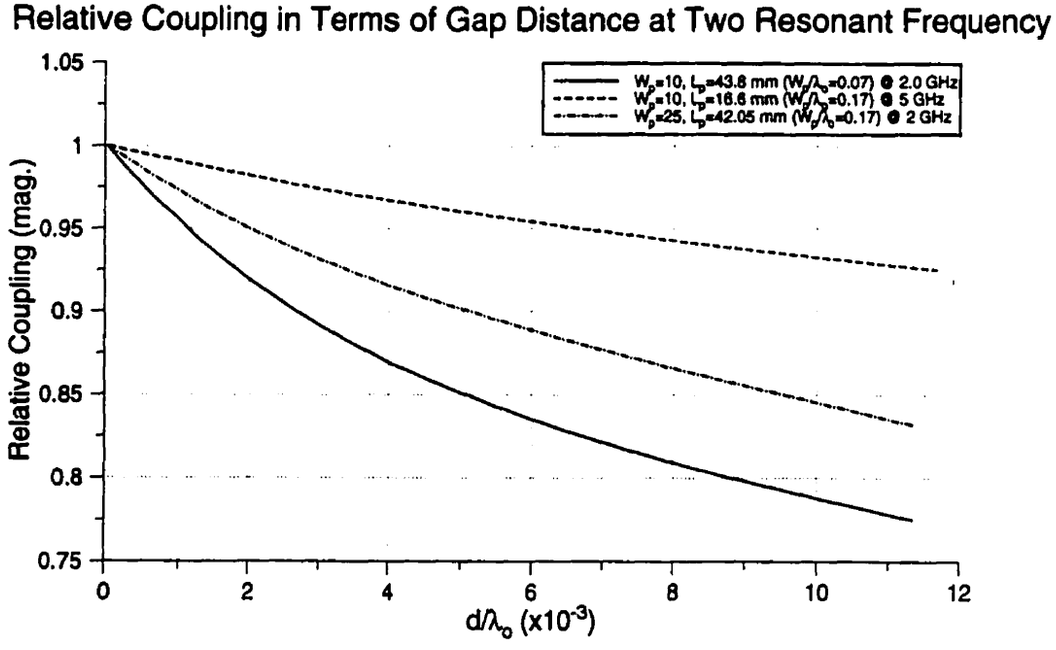

Dimensions (mm): $W = 3.6$, $L = 93.2$ (@ 2 GHz) ; $L = 36.2$ (@ 5 GHz)
Single x-polarized patch with short-circuited termination as in Figure 2.4

Figure 3.22: Comparison of Coupling at Two Resonant Frequencies

a 50Ω probe load is placed at the termination; therefore no transmission loss, S_{21}, is measured.

At the resonant frequency, coupling to patches imposes some impedance on the feedline and consequently mismatch occurs within the resonant band of radiators. At frequencies where no coupling takes place, the input impedance seen at the source is matched and no reflection is anticipated. Thus the greatest mismatch occurs where strongest coupling exists. The return loss plot, therefore, represents a maximum reflection at the resonance and reducing reflection coefficient at other frequencies. Figure 3.23 demonstrates a resonance at 1.99 GHz for the s-band and another at 5.02 GHz in c-band. Further matching is required to improve the return loss.

Figure 3.24 verifies the design with acceptable cross-polarization. Since the width to guided wavelength is the same for both resonators, similar cross-polarization is

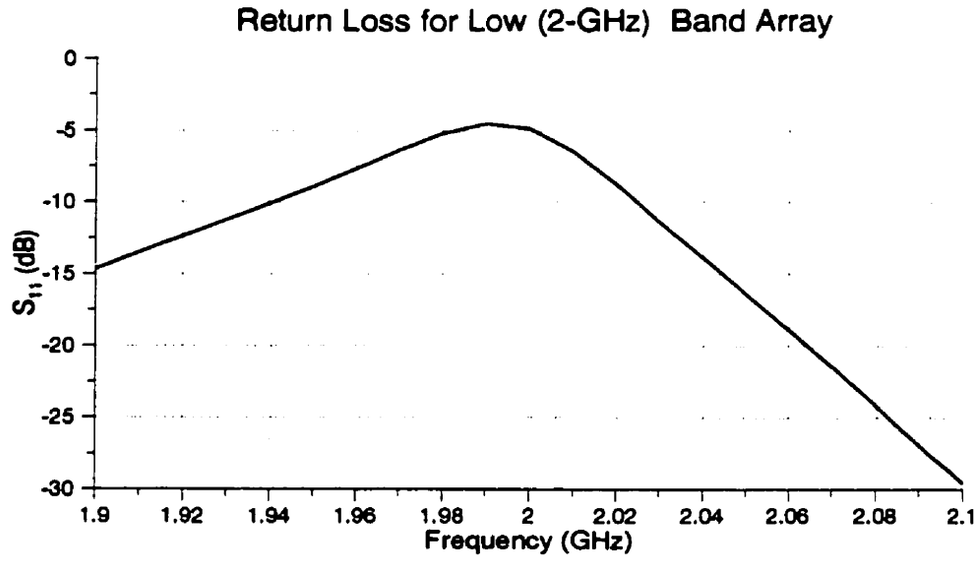

(a) Low Frequency Band
Dimensions (mm): $W_p = 25.0$, $L_p = 41.8$, $d = 0.3$, $D = 94.0$

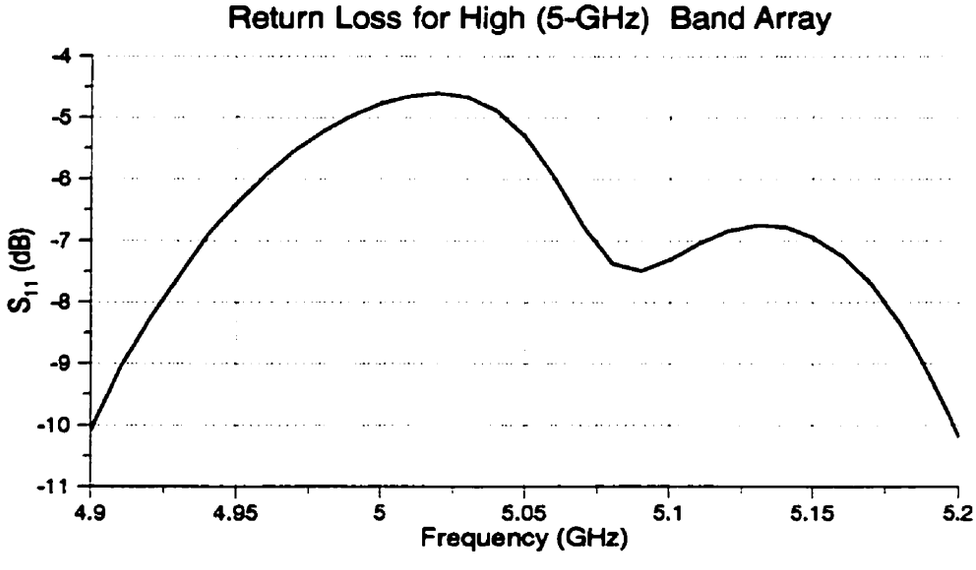

(b) High Frequency Band
All dimensions in mm: $W_p = 10.0$, $L_p = 16.6$, $d = 1.0$, $D = 37.6$
$W = 3.6$, $L = 463.35$, $h = 1.524$; $\epsilon_r = 3.2$

Figure 3.23: Resonance Behavior of Dual Band Array with Matched Feedline (Figure 3.21)

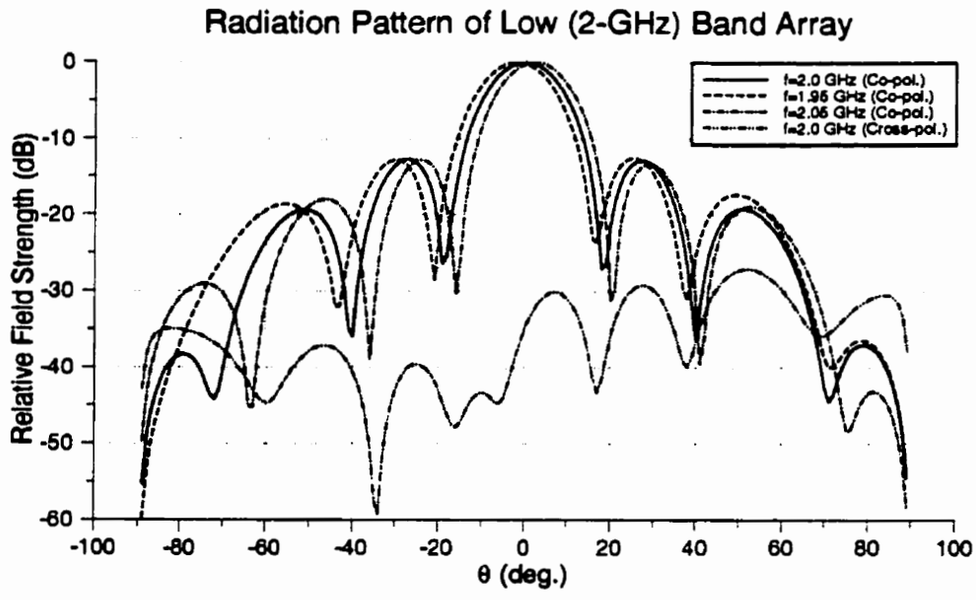

(a) Low Frequency Band: $W_p = 25.0$, $L_p = 41.8$, $d = 0.3$, $D = 94.0$ all in mm

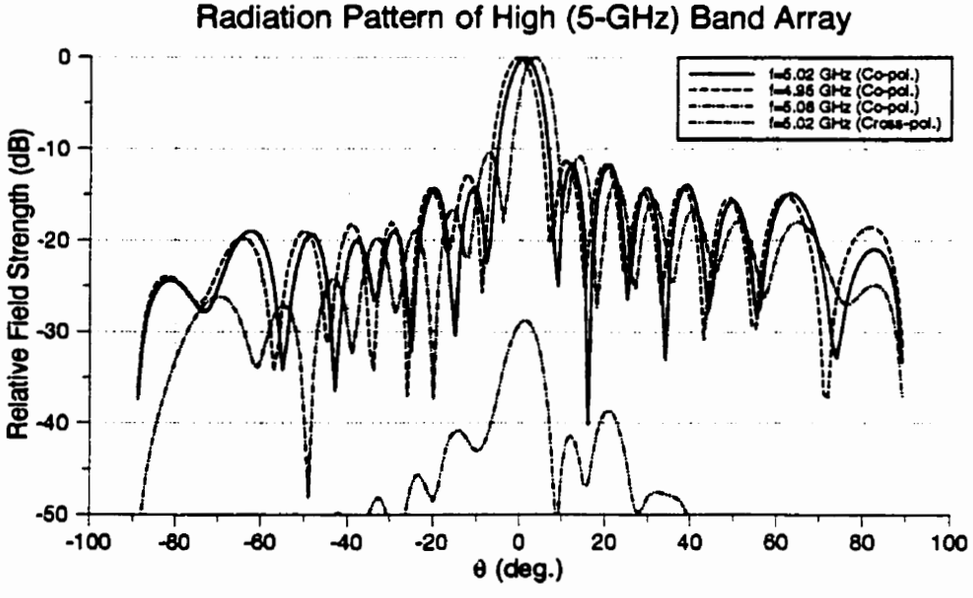

(b) High Frequency Band: $W_p = 10.0$, $L_p = 16.6$, $d = 1.0$, $D = 37.6$ all in mm

Figure 3.24: Radiation Pattern of Dual Band Array with Matched Feedline ($\phi = 0$)

achieved at resonance frequency, regardless of polarization type. Both patterns are in $\phi = 0$ plane where the dominant field components are interchanged. $\mathbf{E}_\theta$ is the cross-polar component as opposed to $\mathbf{E}_\phi$, co-polar field, for the s-band antenna. The patterns in $\phi = 90°$ plane at each bands corresponds to the single patch patterns which is not included here.

3.9.2 Planar Dual Band Array Configuration

Further expansion of the dual band dual polarized linear array to a planar array is possible and the effect of such expansion and the considerations required for the design are investigated next. Once again, the traveling-wave as means of excitation is used and the difficulty of positioning the elements at proper maxima is avoided. Figure 3.25 illustrates the expanded form where the separation between two branches is chosen to be 60 mm. Based on the array theory, the optimal separation between each two elements of an array ranges from $0.5\lambda_o$ to $0.8\lambda_o$. The design of planar dual band array is a difficult task and the choice of 60 mm separation is made carefully to compromise between the array separation of each band.

The challenge of planar dual array is taken for an y-polarized low band array at 2.0 GHz (in S-band) and an x-polarized high band at 4.5 GHz (in C-band). The choice of 4.5 GHz operating frequency provides a separation less than λ_o which nevertheless falls out of the above optimal range. However, appearance of grating lobes in each plane is investigated in the simulations.

The y-polarized patches are resonant about 2.0 GHz and the separation of 60 mm between two branches corresponds to $0.4\lambda_o^s$, where the superscript relates to the 2-GHz band or s-band. The x-polarized patches are chosen to be resonant at 4.5 GHz for which the 60 mm separation corresponds to $0.9\lambda_o^c$ at the operating frequency in c-band.

In order to obtain an equal division of power at the probe feed, the feedline impedance of $Z_o = 100\Omega$ is used. With material properties of $h = 1.524$ mm and $\epsilon_r = 3.2$, the feedline width is calculated to be 0.95 mm. Figure 3.25 contains the geometry and the important parameters of the array. The case of a single linear array is also considered for the comparison purpose. The linear array geometry is similar

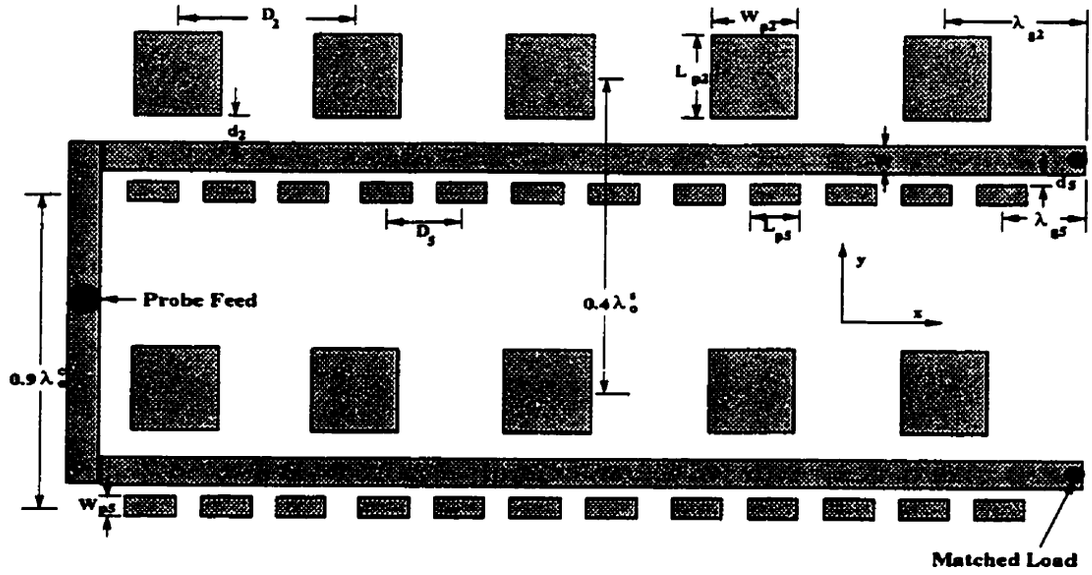

Lower Band: $W_{p2} = 25.0$, $L_{p2} = 41.8$, $d_2 = 0.3$, $D_2 = 98.0 \approx \lambda_{g2}$
Upper Band: $W_{p5} = 10.0$, $L_{p5} = 18.6$, $d_5 = 1.0$, $D_5 = 37.6 \approx \lambda_{g5}$
All dimensions in mm: $Z_o = 100\,\Omega$, $W = 0.95$, $L = 463.35$, $h = 1.524$, $\epsilon_r = 3.2$

Figure 3.25: Geometry of Planar Dual Band Array Configuration

to Figure 3.21 with differences in patch sizes at the c-band.

The unloaded feedlines for linear and planar arrays show relatively perfect match which is required for a traveling-wave feeding scheme.

As expected we observe the maximum reflection occurring at the elements resonance due to higher coupling (Figure 3.26). The planar array exhibits higher reflection at the resonance owing to the added elements and their couplings. Beside the slight frequency shift in resonance, there is a significant gain difference (about 3 dB) between the linear and planar array configurations. However, the gain remains almost constant within the antenna frequency bandwidth in the c-band and decreases in the s-band at bandwidth frequency limits.

Beside the expected increase in gain, the planar array has about the same features as the linear array. The radiation patterns in Figures 3.27 and 3.28 indicate the uneven side lobes as the result of series fed excitation and decaying traveling-wave. Due to choice of narrow patches for both bands the cross-polar component is kept in an acceptable level. However the field patterns in the yz-plane takes the single

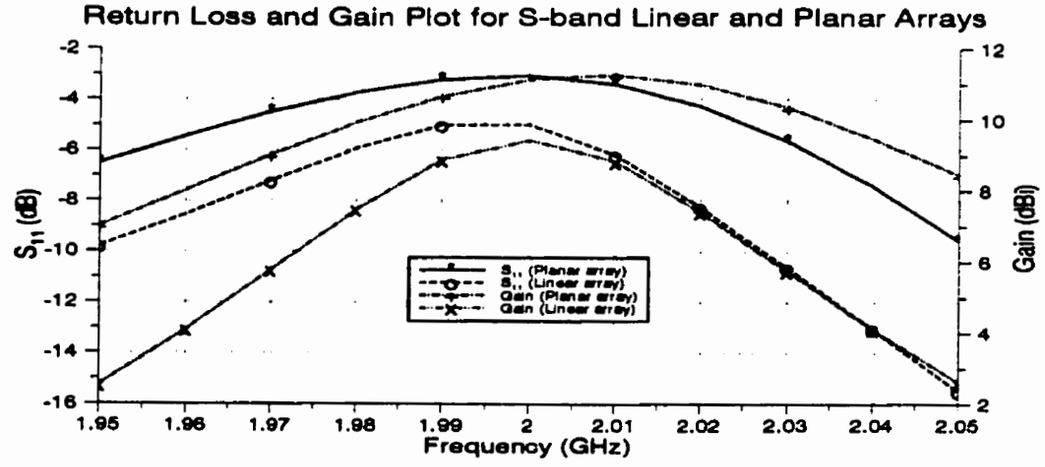

(a) S-Band Return Loss and Gain

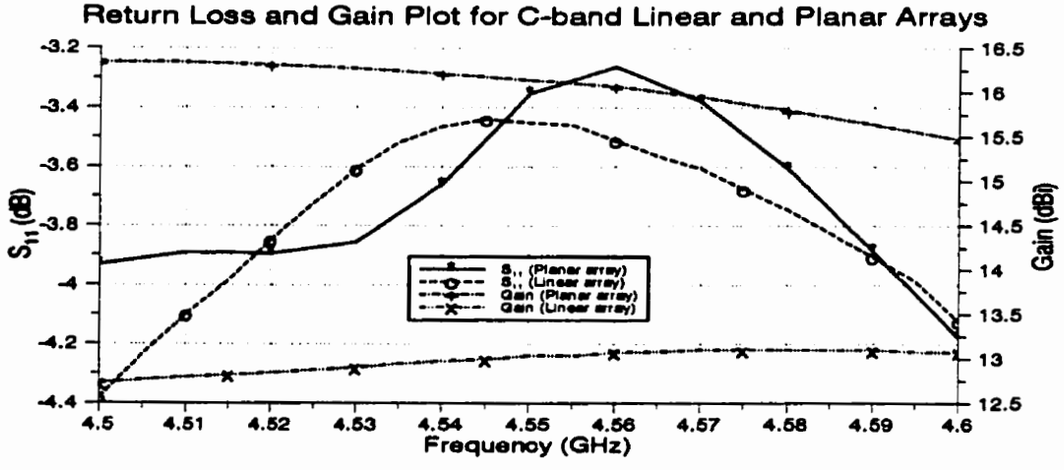

(b) C-Band Return Loss and Gain

Linear: $Z_o = 50\,\Omega$, $W = 3.6$, $L = 463.0$

S-Band: $W_{p2} = 25.0$, $L_{p2} = 41.8$, $d_2 = 0.3$, $D_2 = 93.9 \approx \lambda_{g2}$

C-Band: $W_{p5} = 10.0$, $L_{p5} = 18.6$, $d_5 = 1.0$, $D_5 = 41.3 \approx \lambda_{g5}$

Planar: $Z_o = 100\,\Omega$, $W = 0.95$, $L \approx 29.0 + 463.0 = 492$ (half the array)

S-Band: $W_{p2} = 25.0$, $L_{p2} = 41.8$, $d_2 = 0.3$, $D_2 = 98.0 \approx \lambda_{g2}$

C-Band: $W_{p5} = 10.0$, $L_{p5} = 18.6$, $d_5 = 1.0$, $D_5 = 43.0 \approx \lambda_{g5}$

All dimensions in mm

Figure 3.26: Comparison of Return Loss and Gain for Linear and Planar Dual Band Uniform Arrays

patch pattern in s-band due to separation of less than $0.5\lambda_o^s$. In the c-band the field patterns in yz-plane appear with considerably high side lobes which is the result of a separation greater than $0.8\lambda_o^c$. Although the significantly large side lobe levels in c-band planar array are not considered grating lobes, this feature marks a demerit in the design. Also the uneven side lobe levels reveals, once again, the non-uniform distribution of power among elements and the necessary gap modification required to obtain a better uniform distribution.

The problems encountered in the design of proximity coupled dual band planar arrays indicate the difficulty involved in the design process and that more careful considerations and some flexibility in design specifications are needed.

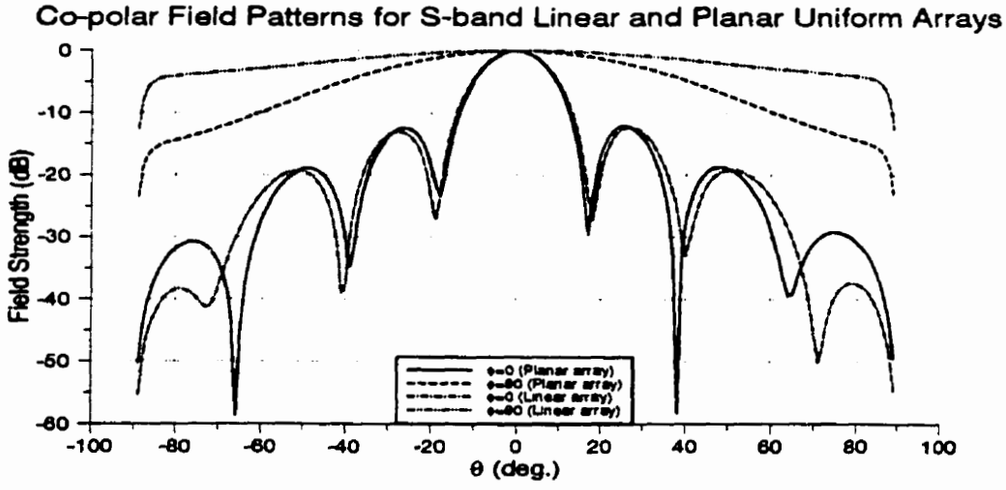

(a) Co-polar Field Patterns at 2.0 GHz

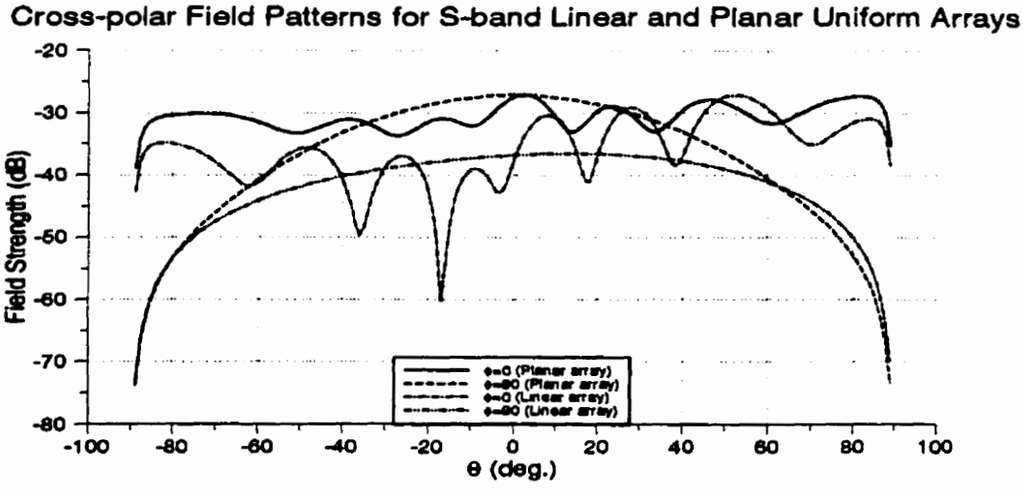

(b) Cross-polar Field Patterns at 2.0 GHz

Linear: $Z_o = 50\,\Omega$, $W = 3.6$, $L = 463.0$

S-Band: $W_{p2} = 25.0$, $L_{p2} = 41.8$, $d_2 = 0.3$, $D_2 = 93.9 \approx \lambda_{g2}$

C-Band: $W_{p5} = 10.0$, $L_{p5} = 18.6$, $d_5 = 1.0$, $D_5 = 41.3 \approx \lambda_{g5}$

Planar: $Z_o = 100\,\Omega$, $W = 0.95$, $L \approx 29.0 + 463.0 = 492$ (half the array)

S-Band: $W_{p2} = 25.0$, $L_{p2} = 41.8$, $d_2 = 0.3$, $D_2 = 98.0 \approx \lambda_{g2}$

C-Band: $W_{p5} = 10.0$, $L_{p5} = 18.6$, $d_5 = 1.0$, $D_5 = 43.0 \approx \lambda_{g5}$

All dimensions in mm

Figure 3.27: Field Patterns for Linear and Planar S-Band Uniform Arrays

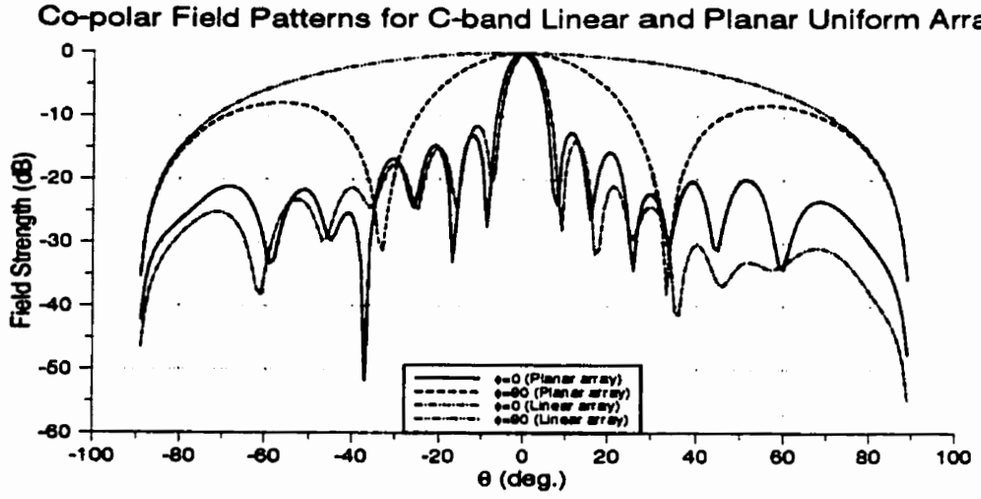

(a) Co-polar Field Patterns (Planar array at 4.56 GHz; linear array at 4.55 GHz)

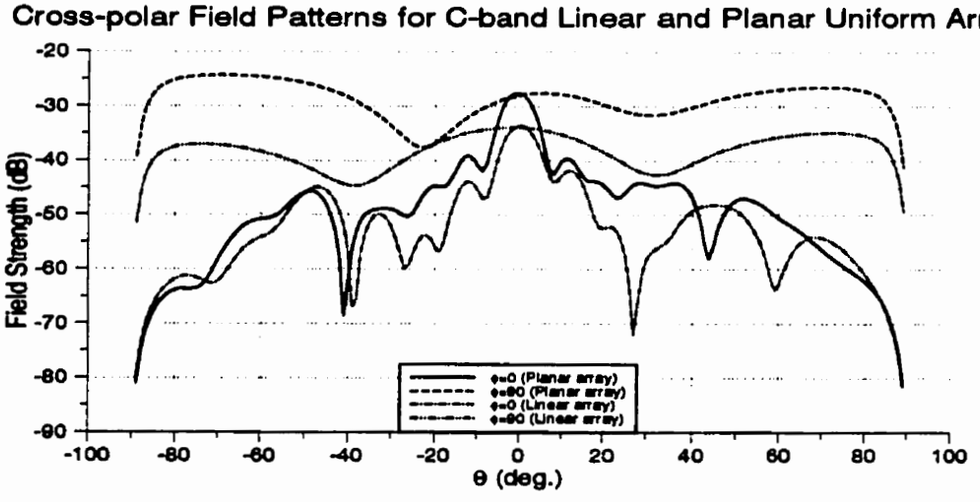

(b) Cross-polar Field Patterns (Planar array at 4.56 GHz; linear array at 4.55 GHz)

Linear: $Z_o = 50\,\Omega$, $W = 3.6$, $L = 463.0$

S-Band: $W_{p2} = 25.0$, $L_{p2} = 41.8$, $d_2 = 0.3$, $D_2 = 93.9 \approx \lambda_{g2}$

C-Band: $W_{p5} = 10.0$, $L_{p5} = 18.6$, $d_5 = 1.0$, $D_5 = 41.3 \approx \lambda_{g5}$

Planar: $Z_o = 100\,\Omega$, $W = 0.95$, $L \approx 29.0 + 463.0 = 492$ (half the array)

S-Band: $W_{p2} = 25.0$, $L_{p2} = 41.8$, $d_2 = 0.3$, $D_2 = 98.0 \approx \lambda_{g2}$

C-Band: $W_{p5} = 10.0$, $L_{p5} = 18.6$, $d_5 = 1.0$, $D_5 = 43.0 \approx \lambda_{g5}$

All dimensions in mm

Figure 3.28: Field Patterns for Linear and Planar C-Band Uniform Arrays

Chapter 4

Fabrication and Test

4.1 Introduction

This chapter deals with the comparison between the experimental and simulation results. It also includes evaluation of antenna performance for some cases. The single element structure and problems involved in fabrication are discussed first and then the three different array configurations are thoroughly examined.

4.2 Single Element Fabrication

The single element was built manually in order to obtain a preliminary comparison. The fabrication of single element revealed some of the considerations which have to be taken into account before construction of the array. One of the very important results from the single element configuration is the effect of connectors when added to the configuration. The typical connectors used in the sample antenna are for side feeding and have a total length of 10.47 mm. The outer length which extends from the board is about 9.6 mm. Considering the connection to the coaxial cable of almost 3 mm into the connector, there is a length of approximately 6.4 mm added to the feedline when connectors are mounted onto the structure, shown in Figure 4.1.

As a result of the added length, the actual length of feedline has to be 80.5 mm to achieve an open-circuited feedline at 2.0 GHz when two connectors are added to the structure. Including the extension of connector, the physical length of $80.5+2(6.4) = 93.3$ mm is measured, which is in agreement with the simulation length for a strip

Table 4.1: Summary of Experimental and Simulation Results for a y-polarized Single Patch

	Simulation	Experiment
S_{11}	-8.2 (dB)	-4.6 (dB)
Reasonant Frequency	1.99 (GHz)	2.00 (GHz)
Impedance	$110 + j14.5$ (Ω)	$186.6 - j37.2$ (Ω)

structures and the same configuration on **Ensemble** . The single patch radiator exhibits an impedance of $110.0 + j14.5$ Ω measured on network analyzer. A tuning stub of width 3.6 mm and length of 32.4 mm was estimated for the structure under test. The location of stub is estimated to be around 18.75 mm which was taken from the center of patch. In this design, an assumption that the impedance seen at the port is mostly due to the patch located at the center of λ_g length feedline including the connector extension length, is made. Therefore the stub should be positioned 18.75 mm away from the load or center of patch.

The same structure resulted in impedance of $186.67 - j37.15$ Ω at 2.0 GHz by **Ensemble** . The tuning stub corresponding to that impedance has the same width and length but the location was estimated to be about 15.6 mm from the patch center. From Figure 4.3 we notice that the experimental outcome appears to be more favorable.

The return loss of about -8.2 dB at 1.99 GHz was registered for a y-polarized single patch located about $\lambda_g/2$ from the source as compared to loss of -4.5 dB at 2.0 GHz simulation result. The same difference is observed where the tuning stub reduce the return loss of the prototype to -28.8 dB at 2.008 in comparison to -17.4 dB at 2.01 simulated structure.

4.3 Fabrication Limitation

Although arrays consisting of 10 elements are studied in hope of scaling the configuration to higher frequency, the cost and accuracy of fabrication led us to building the antenna at the first suggested frequency band and to a shorter length. After feasible

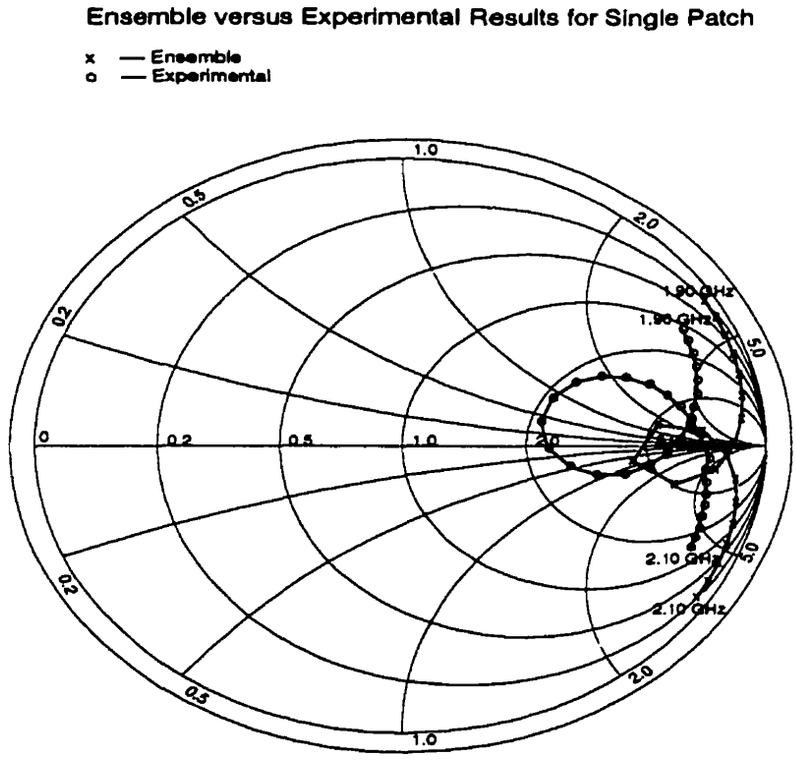

Dimensions (mm):
$W = 3.6$, $L = 93.3$, $W_p = 37.5$, $L_p = 41.3$, $h = 1.6$, $D_{offset} \approx 47.0$, $d \approx 0.5 - 0.6$; $\epsilon_r = 3.2$

Figure 4.2: Impedance Comparison between Simulation and Experiment for a Single Patch Configuration

sizes of material were considered, an array of $5\lambda g$ in length for manual fabrication on MC5 material was decided.

MC5 material is readily available and inexpensive with the disadvantage of above average lossy dielectric. Some of the properties of MC5 are $\epsilon_r = 3.2 \pm 0.5$ and dissipation factor of 0.0052 at 1 GHz($\tan\delta = 0.008$ at10 GHz). The loss tangent of $\tan\delta = 0.008$ was used in simulation despite the interpolated value of $\tan\delta = 0.0055$ at 2 GHz. The laminate with 10^9 MΩ-cm volume resistivity is clad by 1 oz copper layer.

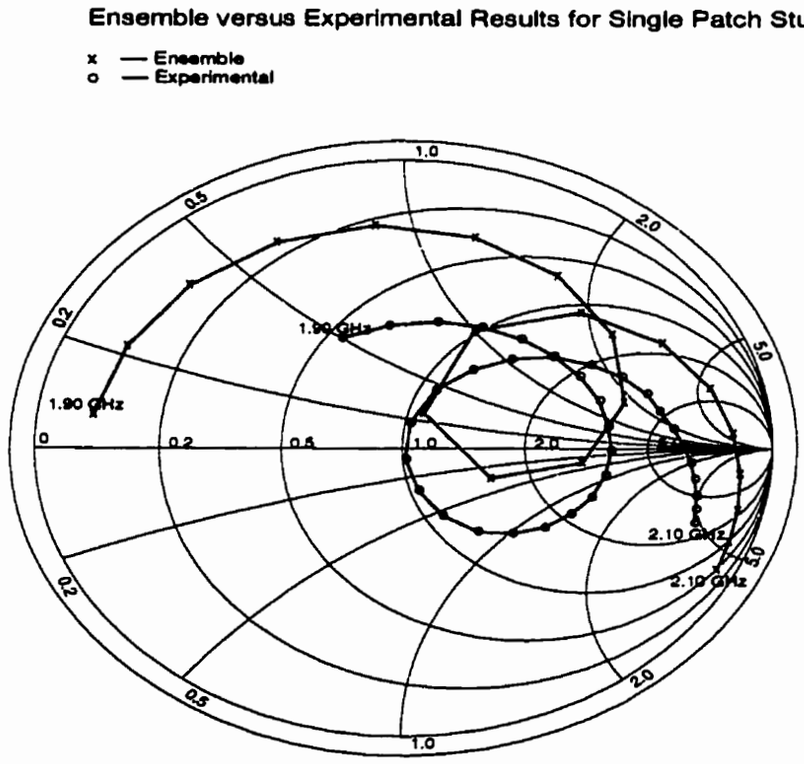

Stub length and location (**Ensemble**): $Length_{stub} = 32.49$ mm, $Loc._{stub} = 15.6$ mm
Stub length and location (Experimental): $Length_{stub} = 32.4$ mm, $Loc._{stub} = 18.7$ mm

Figure 4.3: Impedance Comparison between **Ensemble** and Experimental Single Patch Configuration with Tuning Stub

4.4 Experimental versus Simulation Results

Since manual fabrication is an elaborate process, only three configurations for conducting measurements were assembled. Two 5-element arrays with uniform and Taylor distributions at 2 GHz band and a dual band dual polarized set resonant at 2 and 5 GHz bands are the three cases considered for testing.

4.4.1 Uniform Array

A uniform array consisting of 5 patches placed λ_g apart from each other is built and tested under two feeding methods.

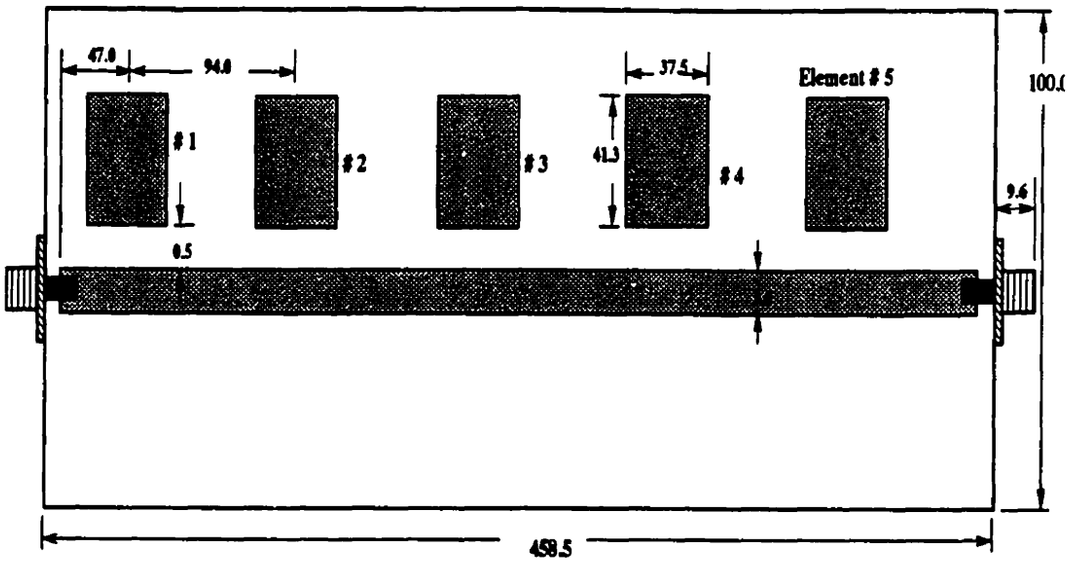

Figure 4.4: Top View of Array Configuration in Proximity of a Feedline

A feedline of width 3.6 mm on average is mounted on three laminate sheets of 45.8 × 10.0 cm. The open-circuited feedline exhibits high impedance at 1.996 GHz which is close to the desired 2.0 GHz. The total length becomes near 472 mm when 6.4 mm connector extension added to the feedline is included. This length corresponds to $5\lambda_g$ at 2 GHz.

The uniform array under test is terminated with an open-circuit and insertion parameters are obtained using a network analyzer. Similar condition is simulated on **Ensemble** and two outcomes are graphed together for comparison in Figure 4.5.(a).

Once the design is tested under the open-end termination, the traveling-wave feeding is an easy task by just terminating the feedline with 50Ω load. The deviation between the results is attributed mostly to a larger loss tangent. The slight shift in resonance is merely due to inaccurate fabrication and inexactness of dimensions, although **Ensemble** also exhibits some shift in resonance for different mesh sizes. In simulation 36% reduction in the cell size, as compared with the optimal size suggested by the software, is employed to obtain results in better agreement with the experimental ones.

The impedances are also compared as shown in Figure 4.5.(b) and obviously better impedance bandwidth is observed for the experimental data. This is due to the higher loss tangent of material and not a figure of merit in this case.

The far-field pattern which is measured in the anechoic chamber reveals a fair agreement between the desired pattern and the achieved one [see Figure 4.6.(a)]. The maximum gain of 11.4 dBi was measured at 2.00 GHz which is an excellent match with the simulated value at this center frequency. However uneven side lobe levels in the measured pattern indicates a non-uniform distribution of power.

The maximum cross-polar level is measured about -19 dBi below the main co-polar beam at the resonant frequency, where the simulated results indicate -21 dBi from the maximum gain. Both trends show similarity such as occurrence of maximum cross-polar component at the boresight.

Figure 4.6.(b) illustrates the integrity of pattern at two edges of the frequency band and the degree of agreement between the measured and simulated patterns.

4.4.2 Calculation of Efficiency

In order to evaluate the performance of the antenna, a comparison between the simulated and measured results as well as theoretical estimates is made.

As a measure of the correctness, an empirical formula based on the aperture theory gives the gain estimate.

$$D = \frac{4\pi A_e}{\lambda_o^2} \tag{4.1}$$

where A_e is the effective area of the aperture. At 2 GHz the length of about $3.14\lambda_o$ and width of near $0.5\lambda_o$ gives

$$D = \frac{4\pi\,(3.14\lambda_o)\,(0.5\lambda_o)}{\lambda_o^2} = 19.75 \quad (12.95\ dBi)$$

The above estimate gives us some measure to compare with the simulation results. From the Figure 4.6 a gain of 11 dBi at 1.98 GHz is read and compares well with the estimated gain.

A summary of comparison is included in the following table (Table 4.2). The case of the open-ended feedline is considered for this purpose. The feedline without any

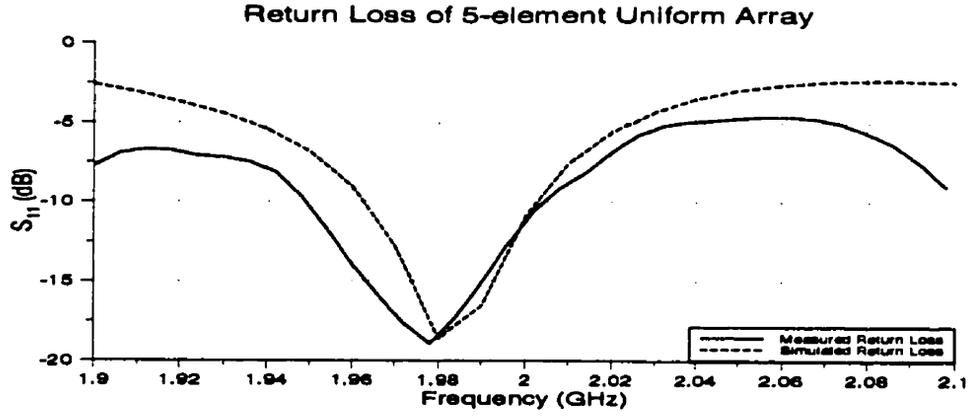

(a) Return Loss

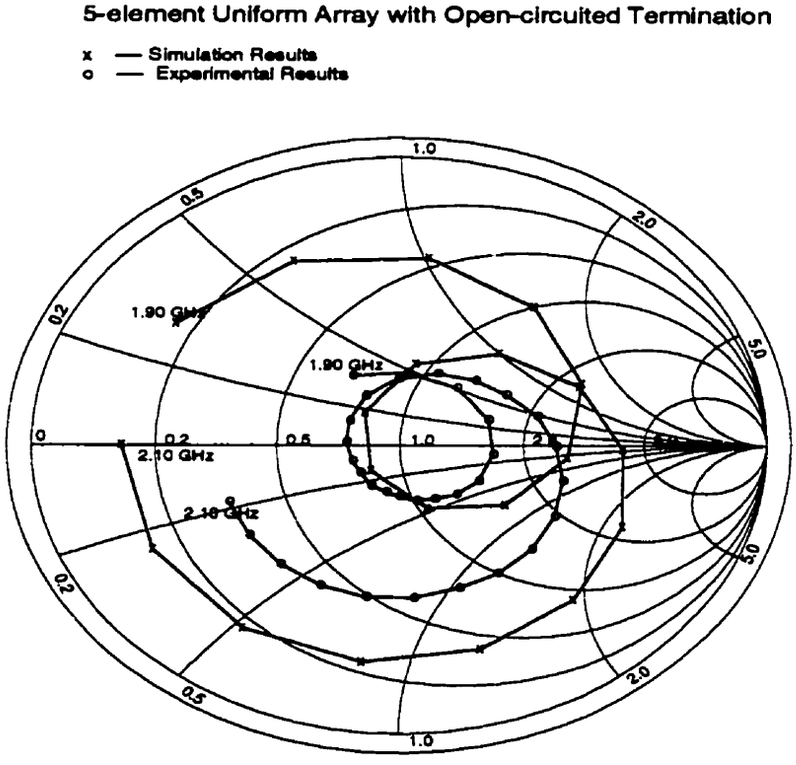

(b) Input Impedance

Dimensions (mm): $W = 3.6$, $L = 93.3$, $W_p = 37.5$, $L_p = 41.3$, $h = 1.6$, $d \approx 0.5 - 0.6$, $\epsilon_r = 3.2$

Figure 4.5: Return Loss and Impedance Comparison between Simulation and Experiment for a Single Patch Configuration (Figure 4.4)

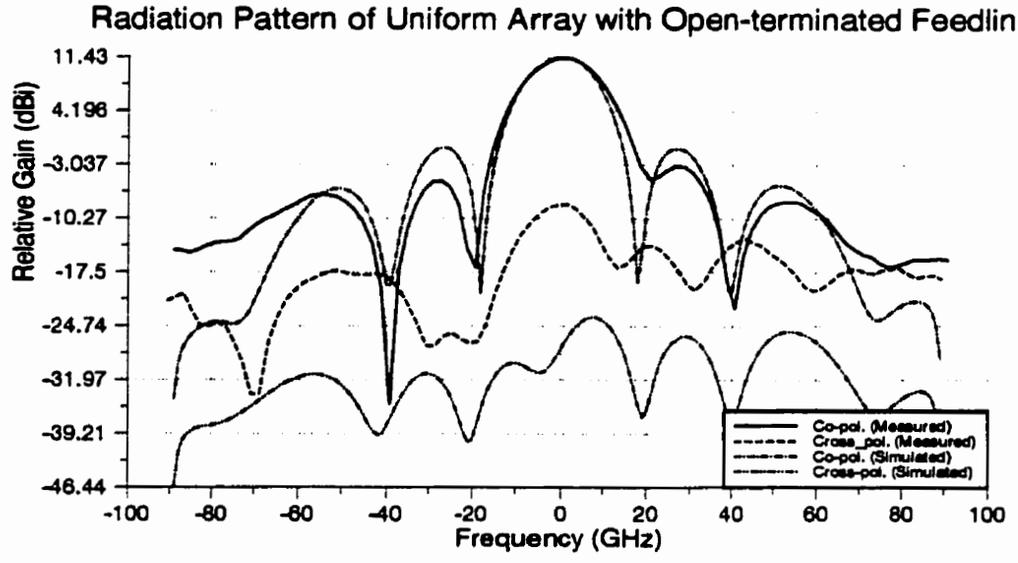

(a) Co-polar and cross-polar patterns at the center frequency

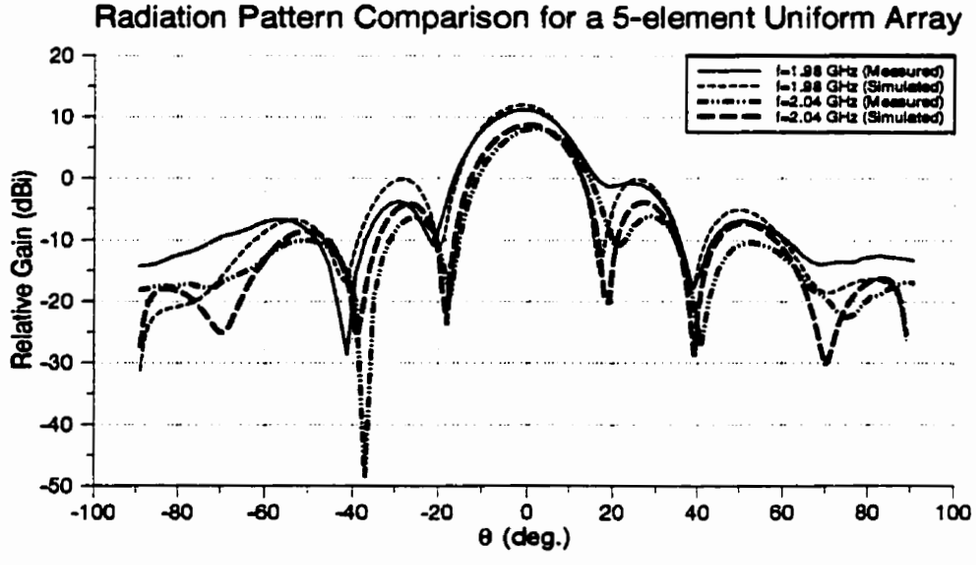

(b) Pattern comparison at the bandwidth frequencies

Dimensions (mm): $W = 3.6$, $L = 471.7$, $W_p = 37.5$, $L_p = 41.3$, $h = 1.6$, $d \approx 0.5 - 0.6$, $\epsilon_r = 3.2$

Figure 4.6: Simulation and Experimental Radiation Patterns for the 5-element Uniform Array with Open-circuited Termination (Figure 4.4)

Table 4.2: Efficiency Calculation Results

	Simulation	Experiment	Theory
S_{11} (dB)	-18.6 @ 1.98 GHz	-18.9 @ 1.978 GHz	-
Gain (dBi)	11.8	11.1	12.95
HPBW (dB)	$\approx 18.0^o$	$\approx 17.5^o$	$\approx 16.5^o$
SLL (dB)	12.0	14.9	12.8

patch placed exhibits an open termination with the impedance $288 + j9.1\ \Omega$ at 1.996 GHz.

The efficiency of antenna can be estimated through $e = \frac{P_{rad}}{P_{tot}}$, where $P_{rad} = P_{in} - P_{line} - P_r$. P_{line} is measured with no load condition ($P_{line} = 1 - |S_{11}|^2 = 1 - |0.92707|^2 = 0.1405$). The radiated power is approximately $P_{rad} = 1 - |0.11738|^2 - 0.1405 = 0.8457$. This figure indicates that for a unit input power there is about 80% power radiated. In practical application this figure reduces to 70% due to other loss factors.

4.4.3 Array with Taylor Distribution

Measurements is also conducted on an array of 5 elements with an approximate Taylor distribution across it. The same values (SLL=-20 dB SLL $\bar{n}$=3) are used in order to obtain the distribution for the desired pattern.

Table 4.3: Taylor Distribution

Element #	Taylor Distribution	Normalized Coupling	Gap d (mm)
3	≈ 1.0	0.65	0.5
2	0.75	0.49	0.9
1	0.52	0.34	1.4

Table 4.3 summerizes the values obtained in each stage in order to establish an approximate Taylor distribution by means of the gap adjustment. The comparison

of return loss for this configuration suggests the highly lossy material used for experimental purpose.

The return loss of the array along with the impedance on Smith chart are all illustrated in Figure 4.7. From the plot we observe that the bandwidth for the actual array is about 2.0% (1.97-2.01 GHz) where the simulation suggests a 1.0% (1.98-2.0 GHz).

Next comparison is for the far-field pattern of two results which are selected for the best comparable ones. There is a noticeable frequency shift in the corresponding patterns while the resonance frequency appears at 1.99 GHz. In practice this shift in frequency is predictable and usually higher gain is expected to occur at frequencies slightly away form the resonance frequency.

Another significant difference is the higher side lobe levels for the experimental pattern. The maximum side lobe level of -15 dB is compared to -20 dB, the desired level. This signifies that the Taylor distribution has not been established along the array and that many factors such as the inaccurate gap distance and unpredicted higher material loss could be the reason for the discrepancy between the results.

The simulation result of resonant current at the center of each patch in normalized form is compared with the exact one in Table 4.4.

Table 4.4: Current Amplitude and Phase in Taylor Distribution for a 5-elements Array

Element #	**Theoretical Taylor Distribution**	**Simulated Normalized Amplitude**	**Phase Difference (deg.)**
1	0.52	0.53	1.4
2	0.75	0.76	5.7
3	≈1.0	1.0	0.0
4	0.75	0.75	4.8
5	0.52	0.51	2.1

Despite the non-uniform gap size, the phase distribution follows similar to the amplitude and remains within 5° difference. The amplitude falls well with the desired distribution.

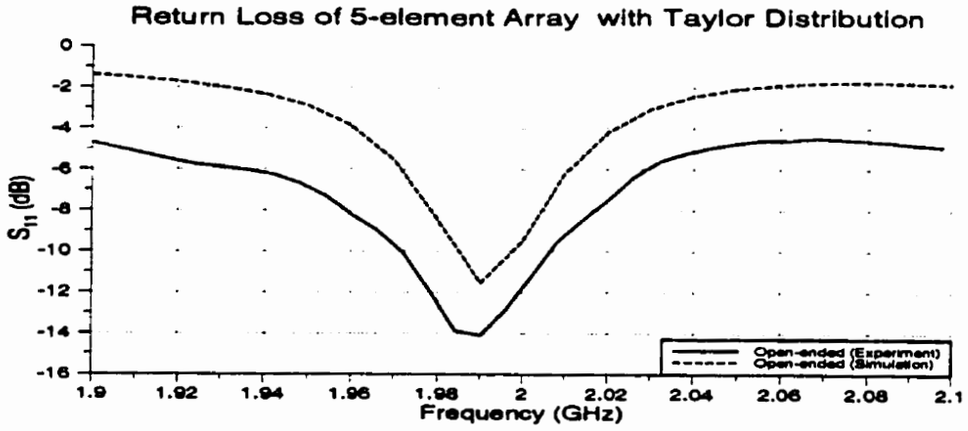

(a) Return Loss

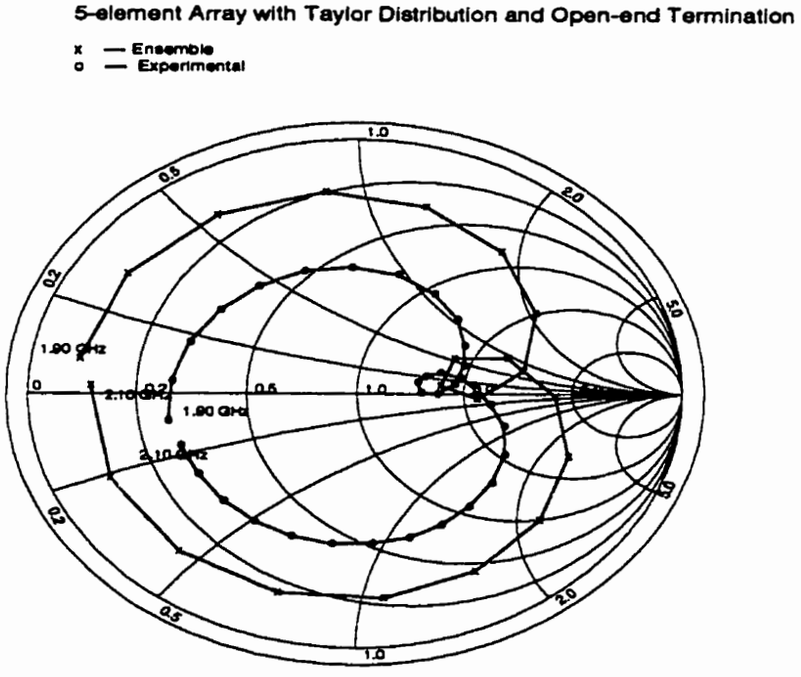

(b) Impedance

$W = 3.6$, $L = 471.7$, $W_p = 37.5$, $L_p = 41.3$, $h = 1.6$, $D = 94.0$

$d_3 = 0.5$, $d_{2,4} = 0.9$, $d_{1,5} = 1.4$, $\epsilon_r = 3.2$, $\tan\delta = 0.008$ (all dimensions in mm)

Figure 4.7: Comparison between Simulation and Experimental Return Loss and Impedance of 5-element Array with Taylor Distribution and Open Termination

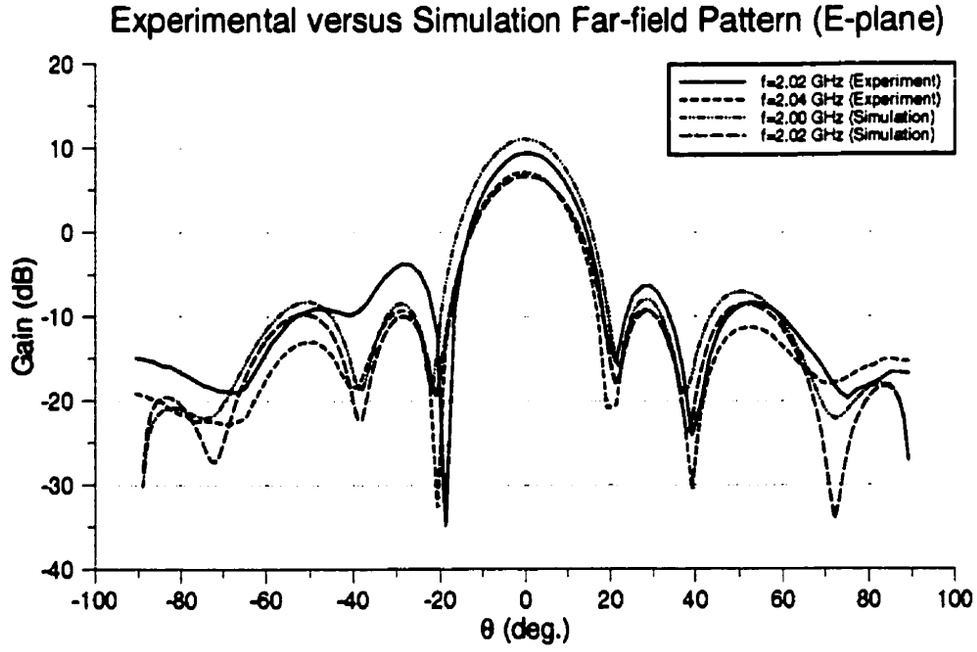

$W = 3.6$, $L = 471.7$, $W_p = 37.5$, $L_p = 41.3$, $h = 1.6$, $D = 94.0$;
$d_3 = 0.5$, $d_{2,4} = 0.9$, $d_{1,5} = 1.4$, $\epsilon_r = 3.2$, $\tan\delta = 0.008$ (all dimensions in mm)

Figure 4.8: Far-field Pattern of 5-element Array with Taylor Distribution ($\phi = 0$)

4.4.4 Dual Band and Dual Polarized Array

In this section the results obtained for the fabricated dual band dual polarized antenna and those for the simulated configuration are compared. The ratio of patch widths to guided wavelength are chosen to be the same to compare the cross-polar component level for both polarizations. The diagram of the fabricated dual band and dual polarized array is shown in Figure 4.9.

For the y-polarized array, an optimal patch size with $W_p = 25.0$ and $L_p = 42.0$ mm is chosen, which has the width to wavelength ratio of $\frac{W_p}{\lambda_o} = \frac{25.0}{150} = 0.17$ for the low band. The same ratio for the higher band is considered and $W_p = 0.17\lambda_o = (0.17)(60) \approx 10.0$ mm is computed. The resonant length of x-polarized patches at 5-GHz band is about 17.0 mm. Based on the geometry of Figure 4.9, the following results are obtained.

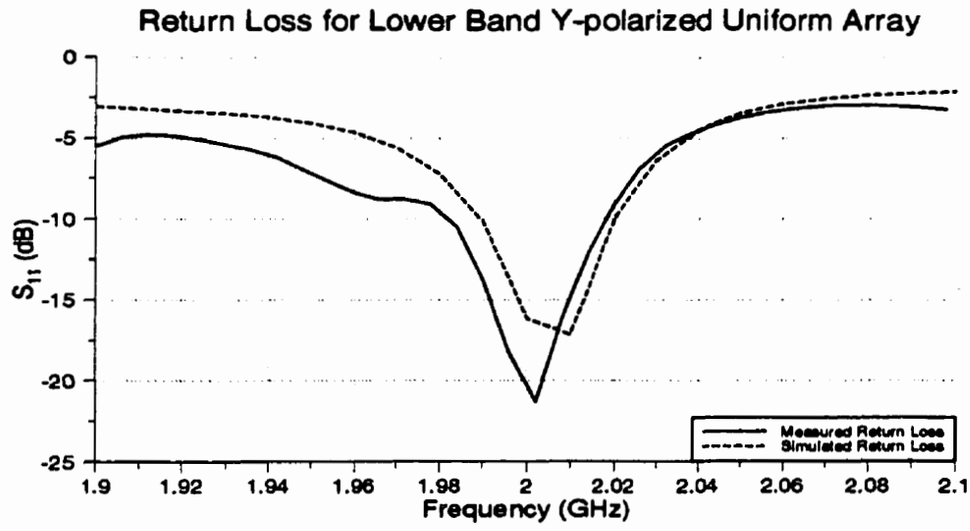

(a) Low Band: $W_p = 25.0$, $L_p = 42.0$, $d \approx 0.3$ $D \approx 94.0$; $N = 5$

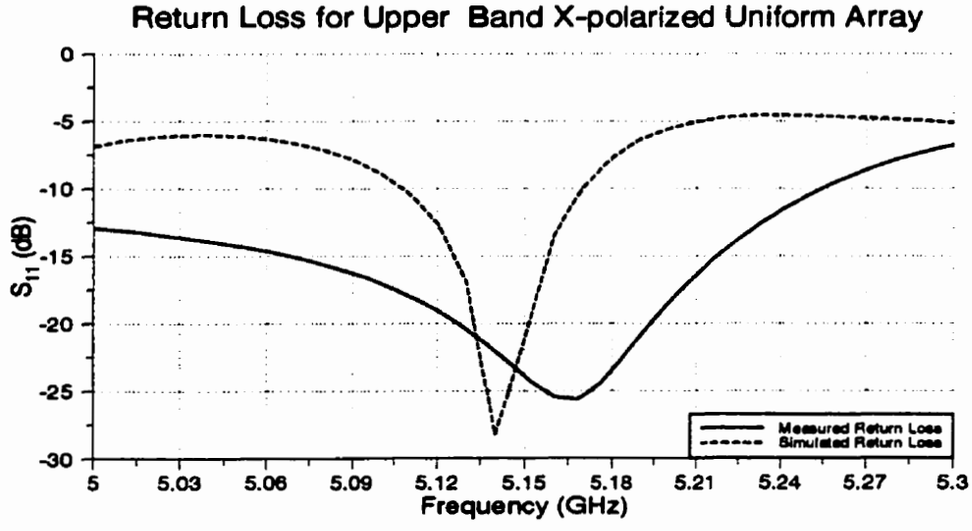

(b) High Band: $W_p = 10.0$, $L_p = 17.2$, $d \approx 0.3$ $D \approx 37.5$; $N = 11$
All dimensions (mm): $W = 3.6$, $L = 471.7$, $h = 1.6$, $\epsilon_r = 3.2$, $\tan\delta = 0.008$

Figure 4.10: Return Loss of Dual Band Array with Uniform Distribution and Open Termination

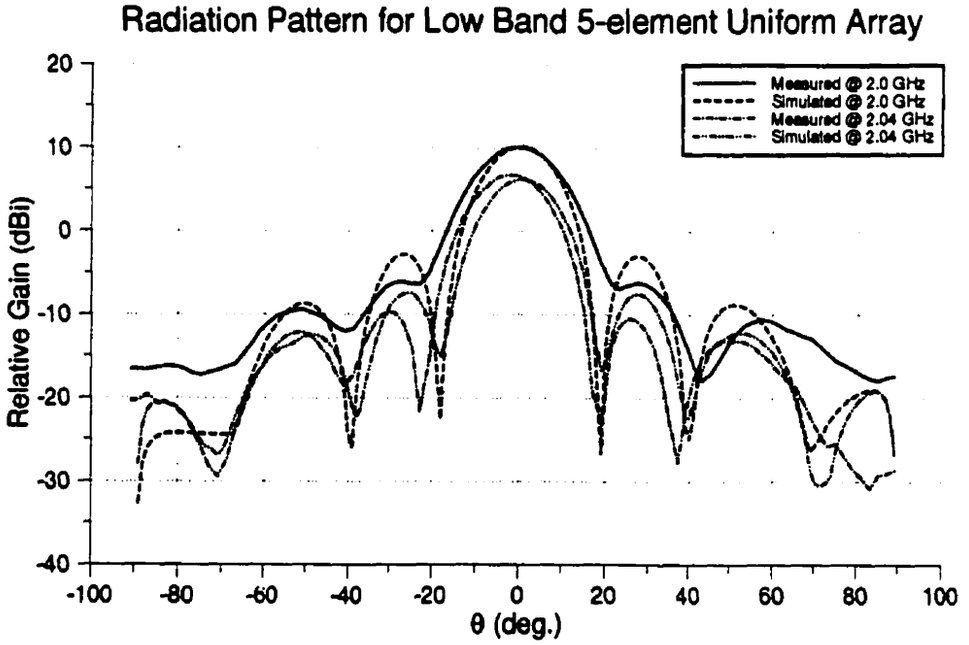

(a) Low Band: $W_p = 25.0$, $L_p = 42.0$, $d \approx 0.3\,D \approx 94.0$; $N = 5$ (dimensions in mm)

Figure 4.11: Radiation Pattern of Lower Band Array with Uniform Distribution and Open Termination ($\phi = 0$)

in comparison with the simulated values as well as the measured single band uniform array discussed earlier in Section 4.4.1.

Although the configurations are not exactly the same due to additional high band array, some of the features of narrow patch resonators in low band are distinguished. Referring to Table 4.5, we observe that despite slight decrease in gain a better cross-polarization level and side lobe level are achieved. The conclusion is that the use of narrow rectangular patch ($0.1 \leq \frac{W_p}{L_p} \leq 0.5$) has many advantages over patches with width to length ratios above 0.5.

4.5 Single Patch on Low Loss Material

The significant discrepancy between the measured and simulated results raised the concern to investigate the difference more in depth. The deviation is mostly attributed

Table 4.5: Comparison of Two Different Uniform Arrays

5-element Single Band with $\frac{W_p}{L_p} = 0.9$ as in Figure 4.4 versus
5-element Y-polarized Low Band with $\frac{W_p}{L_p} = 0.6$ as shown in Figure 4.9

Parameters	$W_p/L_p = 0.9$		$W_p/L_p = 0.6$	
	Measured	Simulated	Measured	Simulated
Gain (dBi) @2.0 GHz	11.4	11.4	10.1	11.3
S_{11} (dBi)	-18.5 @1.98 GHz	-18.0 @1.98 GHz	-21.0 @2.0 GHz	-10.8 @2.0 GHz
Maximum SLL	-13	-12	-15	-13
Cross-polar Level (dB) maximum	-19	-21	-30	-35

to the material loss and considered a disagreement between the manufacturer's specification and the actual material properties. In order to prove this claim, a single patch configuration is built on a different material and only simple measurements of the return loss and input impedance are conducted.

The material used for comparison is Norplex Oak 601 (NO601) with the dielectric constant, $\epsilon_r = 2.55$, thickness, $h = \frac{1}{16}" = 1.6$ mm and loss tangent about, $\tan\delta = 0.002$ at 10 GHz. For the selected material parameters, a feedline with width, $W = 4.5$ mm corresponds to a 50Ω line. In order to measure the material loss, the transmission lines are connected in two-port configuration and the forward transmission, S_{21}, and return loss, S_{11}, are measured at each port. The forward transmission, S_{21}, for a 50Ω line ($W = 102.6$ mm) on NO601 material at 1.726 GHz reads a value of -0.15 dB as compared to -0.24 dB at 2.026 GHz on MC5. The above values translate to 0.99 and 0.97 on magnitude scale, respectively. The reflected wave is measured $S_{11} = -15.4$ dB on NO601 and $S_{11} = -22.1$ dB on MC5 material.

The calculations of material loss for printed transmission lines whose widths correspond to 50Ω lines are given below. For NO601 material the loss calculation is

$$\text{Material Loss} = 1 - |S_{11}|^2 - |S_{21}|^2 = 1 - 0.029 - 0.966 = 0.005$$

and for the MC5 material, the material loss is calculated

$$\text{Material Loss} = 1 - |S_{11}|^2 - |S_{21}|^2 = 1 - 0.006 - 0.946 = 0.048.$$

The comparison between two values reveals a ratio of 10. This figure may not be the exact measure of material loss since some radiation could exist along the line, but difference of 5 or 6 times is expected in practice. The return loss for a single patch configuration with open-circuited termination (refer to Figure 2.4) on both materials are measured next. The feedline length is adjusted such to fall in open-circuited condition of input impedance at vicinity of 2.0 GHz. The measured results are also compared with the simulation ones for both materials.

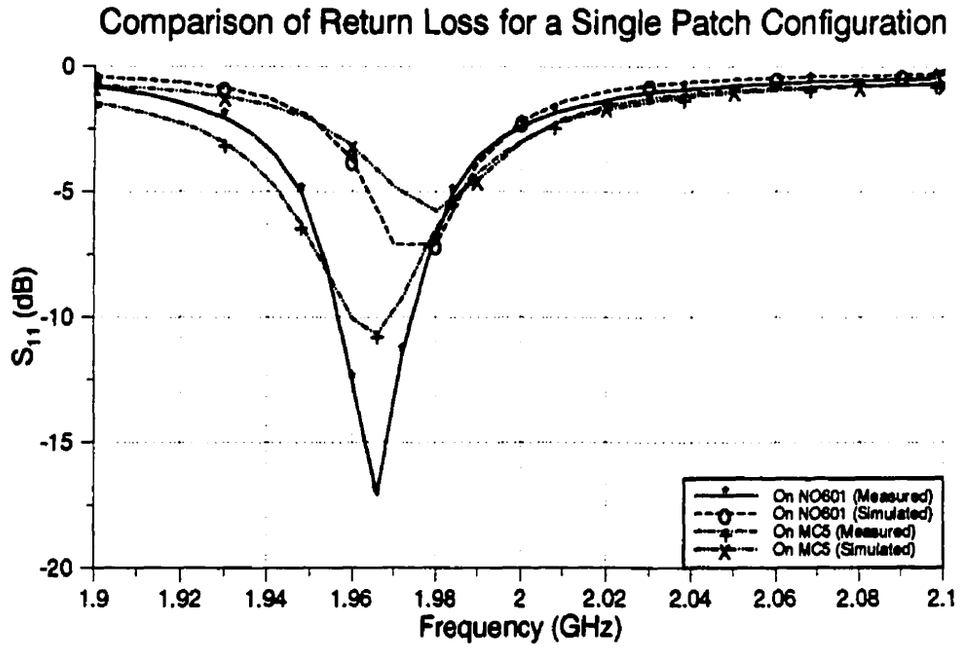

On NO601: $W = 4.5$, $L = 102.6$, $W_p = 37.5$, $L_p = 46.5$, $h = 1.7$, $d \approx 0.3$, $\tan\delta = 0.002$
On MC5: $W = 3.6$, $L = 93.2$, $W_p = 37.5$, $L_p = 42.0$, $h = 1.7$, $d \approx 0.3$, $\tan\delta = 0.008$
All dimensions in mm

Figure 4.12: Return Loss of Single Patch Configuration with Open Termination

The shifts in frequency (Figure 4.12) between the measured and simulated results is due to inexactness of physical dimensions of patches as well as the software inaccuracy. From Figure 4.12 it is concluded that beside the considerable difference in material properties, the disagreement between measured and simulated results attributes mainly to the software numerical results. Throughout the previous section

the discrepancies were related to material loss but it is conclusive that the basis functions used in numerical solution introduce some deviation from the actual results. However, some of the loss differences could also be attributed to the resonance of the patch and the effective coupling between the patch and the feedline at the resonant frequency.

Chapter 5

Conclusion

5.1 Concluding Remarks

The proximity coupled arrays were investigated in this study. They revealed many characteristics similar to the single patch configuration as well as other array arrangements, which can be used in the design applications. These are listed below as the conclusive outcome of the study:

1) The coupling to the patch placed in proximity of a feedline takes place electromagnetically. Either vertical or horizontal excitation with respect to the feedline current can be achieved. In a resonant configuration the voltage standing-wave is the source of capacitive coupling to the resonant element and the vertically resonant patches are best excited when centered at the maxima of the voltage standing-wave.

   The magnetic field about the feedline creates inductive coupling to the nearby patch and the effectiveness of coupling is optimal when the radiator resonates together with the feedline current at the current standing-wave maxima.

2) The most effective control parameter is the gap distance between the element and the feedline. By means of adjusting the gap, one can manage the amount of power coupled to each radiator and configure any desired power distribution across an array of radiators.

3) The patch resonant frequency is mainly determined by its length, but a proper progressive incremental change in the lengths of resonators in an array helps broadening the performance bandwidth while keeping the far-field pattern distortion to a minimal.

4) Although the patch width has some effect on the amout of coupling to the patch, it also characterizes the resonance of the patch to some extent and cannot be used as an effective control parameter.

5) One technique to reduce the cross-polarization is the use of narrow patch resonators. Patches with width to length ratios less than 0.5 and greater than 0.1 minimize the effect of cross-polar components with a trade-off in less coupling surface.

6) The cross-linear array is another technique to reduce the cross-polarization in a single band array. Two patches positioned within λ_g at anti-phase locations across from each other comprise a unit element of a cross-linear configuration. This technique is most desirable for vertical polarization where the resonant current on radiators with width to length ratio greater than 0.5 are desirable.

7) Dual band, dual polarized array configuration is possible with proximity fed arrangement. By proper design the advantage of dual band antenna with optional dual polarization on one configuration can be enjoyed.

8) The y-polarized resonators can be modeled as two radiating slots (with radiation resistance) separated by transmission line and connected via a capacitor to the feedline. The model is useful for circuit analysis and optimization. The coupling in x-polarized resonators, on the other hand, can be represented by a transformer or two inductors with mutual inductance as a function of distance between them. Determination of the relation between the mutual inductance and the gap requires a whole new investigation in the circuit theory.

9) **Ensemble** provides a fairly good approximation to the proximity coupled patch problem under a reasonable mesh resolution but some deviation of the

simulated results from the measured ones indicate some degree of inexactness in the simulated results. This deficiency, however, does not lessen the value of software and its many powerful features.

Hopefully, the above conclusion provides a summary of this study and sheds light on the important features of the subject matter.

Bibliography

[1] E. Cashen, R. Frost, and D. Young, "Improvements relating to aerial arrangements," *British Provisional Patent (EMI Ltd.)*, no. specifications 1294024, 1970.

[2] Emi-Varian, "Printed antennae and front ends," *Microwave Journal*, no. 18, pp. 20F–20G, 1973.

[3] J. R. James, P. S. Hall, and C. Wood, *Microstrip Antenna: Theory and Design.* Peter Peregrinus Ltd., 1981.

[4] T. Miyazaki and K. Itoh, "Analysis and design of a proximity fed microstrip antenna," *Proceedings of ISAP*, pp. 545–548, 1996.

[5] R. K. Hoffmann, *Handbook of Microwave Integrated Circuits.* Artech House Inc., 1987.

[6] P. A. Razzi, *Microwave Engineering, Passive Circuits.* Prentice Hall Inc., 1988.

[7] C. Balanis, *Antenna Theory: Analysis and Design.* John Wiley & Sons, Inc., 1982.

[8] K. Hirasawa and M. Haneishi, *Analysis, Design, and Measurement of Small and Low-profile Antennas.* Artech House Inc., 1992.

[9] M. Ma, *Theory and Application of Antenna Arrays.* John Wiley & Sons Inc., 1974.

[10] Boulder Microwave Technologies Inc., **Ensemble** *for Windows, version 4.1.* 2336 Canyon Blvd, Suit 102, Boulder, Colorado, 80302.

[11] J. R. Mosig and F. E. Gardiol, "Analytical and numerical techniques in the Green's function treatment of microstrip antennas and scatterers," *IEE Proceedings, Part H*, vol. 132, pp. 424–432, December 1985.

[12] P. Bhartia, K. Rao, and R. Tomar, *Millimeter-Wave Microstrip and Printed Circuit Antennas*. Artech House Inc., 1991.

[13] Hewlett-Packard (Canada) EESof, **Libra** *for Windows*. 2670 Queenview Drive, Ottawa, Ontario, K2B 8K1.